MULTIPACTOR IN THE PRESENCE OF HIGHER-ORDER MODES: A NUMERICAL STUDY

By

Scott Alan Rice

A DISSERTATION

Submitted to
Michigan State University
in partial fulfillment of the requirements
for the degree of

Electrical Engineering—Doctor of Philosophy
Physics—Dual Major

2017

ABSTRACT

MULTIPACTOR IN THE PRESENCE OF HIGHER-ORDER MODES:
A NUMERICAL STUDY

By

Scott Alan Rice

Resonant electromagnetic structures are vitally important in engineering and scientific applications, ranging from devices as ubiquitous as antennas and microwave ovens, to devices as demanding as high-power microwave sources and particle accelerator components. As we push the limits on the design and operation of such structures, one of the physical limitations that we must contend with is electrical breakdown, which becomes increasingly likely as we increase field strength and reduce structure sizes. Multipactor is a type of breakdown in which electromagnetic fields accelerate free electrons into a material, which then ejects secondary electrons which are re-accelerated back into the material, and which sustains or grows the breakdown current over time.

We are interested in understanding multipactor better because it is one of the common design constraints for high-power resonant structures around microwave frequencies, such as klystrons, couplers, waveguides, and accelerating cavities used in particle accelerators. Besides being a design constraint, we could also potentially employ the non-linear nature of multipactor to intentionally attenuate sporadic harmful power levels which may affect certain sensitive equipment, such as for the protection of front-end electronics on radio receivers in space-borne applications.

This dissertation details the results of numerical study of two-surface multipactor driven by time-harmonic fields, with a specific focus upon how secondary electron emission models can affect the resulting multipactor predictions, and how multipactor susceptibility and trajectories

can be affected by the presence of additional modes within a resonant structure. The primary focus is on multipactor occurring between the inner and outer conductors of coaxial geometries, but some parallel plate geometries are also considered.

The scope of investigation is limited to the multipactor regime in which space charge effects can be neglected. In practice this means the early-time evolution of multipactor, since it takes some time before space charge effects become significant. Despite this simplifying assumption not being applicable to the late-time behavior of multipactor, this approach still allows for much practical benefit in the understanding of multipactor genesis and controllability, which is frequently the most significant concern of engineering interest.

Dedicated to the memory of my father.

TABLE OF CONTENTS

LIST OF TABLES

LIST OF FIGURES

KEY TO ABBREVIATIONS

GDE	Growth-decay error
RMSE	Root-mean-square error
SEE	Secondary electron emission
SEY	Secondary electron yield
TEM	Transverse electromagnetic

CHAPTER 1: Introduction

1.1 Motivation

Over the past approximately 70 years, resonant electromagnetic structures have become increasingly important in engineering and scientific applications, ranging from devices as ubiquitous as antennas and microwave ovens, to devices as demanding as high-power microwave sources and particle accelerator components. As we push the limits on the design and operation of such structures, one of the physical limitations that we must contend with is electrical breakdown, which becomes increasingly likely as we increase field strength and reduce structure sizes.

Depending on the physical situation, different types of breakdown are possible. Transient direct-current breakdown can occur in circumstances where the potential difference between surfaces due to static charges becomes sufficiently strong, resulting in a momentary arc as the surfaces equilibrate. Sustained direct-current or alternating-current breakdown is possible in circumstances when there is a power source to drive the sustained arcing. Depending on the circumstances in which breakdown occurs, it can either be desired, benign, problematic, or even catastrophic.

Multipactor [1][2][36] can be considered as a type of breakdown in which a sustained current of electrons can impact surfaces and cause the release of secondary electrons, which are then free to be accelerated by the fields and again impact a surface, carrying on the multipactor. A pictorial representation is shown in Figure 1 below. Multipactor can in theory occur between an arbitrary number of surfaces, but historical interest has tended to focus on circumstances where multipactor is most typically seen in practice, which is either two-point multipactor which occurs between two conducting surfaces, or single-point multipactor on a single dielectric surface. Within this dissertation, we exclusively focus on the case of two-surface multipactor between conducting surfaces. For this case, multipactor can only occur when oscillatory fields of certain field strengths and frequencies interact with materials capable of emitting secondary electrons with sufficient ease; the resonant constraints upon two-surface multipactor will be explained with mathematical precision in the body of this dissertation.

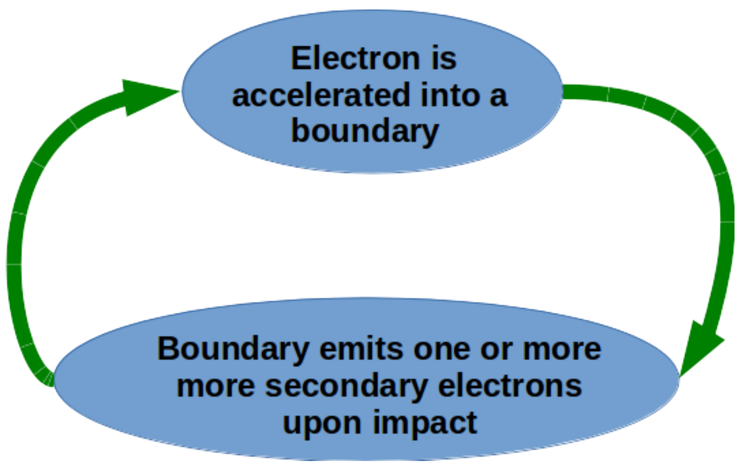

Figure 1: Conceptual diagram of multipactor breakdown.

We are interested in understanding multipactor better because it is one of the common design constraints for high-power resonant structures around microwave frequencies, such as klystrons, couplers, waveguides, and accelerating cavities used in particle accelerators. Within the context of microwave sources and particle accelerators, multipactor is generally a nuisance at best, drawing energy out of structures that would ideally be used to produce high fields. It is also capable of detuning structures and causing changes in device impedance [12], which may degrade device performance within a given application. However, multipactor can also be catastrophic in other circumstances, for example the heat deposition from an unwanted multipactor current can push a superconducting cavity out of the superconducting regime [36], potentially resulting in quenching of the superconductivity and possible damage to the cavity or surrounding structures.

In some potential applications, the non-linear response of multipactor as a function of field strength could also be intentionally employed. An example would be the protection of sensitive circuitry on radio receivers which may be subjected to sporadic high-intensity fields, such as on a satellite outside Earth's protective ionosphere and thus subject to the direct effects of solar storms. In such a situation, the multipactor could be intentionally used to attenuate excess field strength before a received signal is introduced to the receiver's front-end electronics.

1.2 Background

An examination of the technical literature shows multipactor investigations going back to the 1920's, before multipactor as it is understood today was identified and named as a specific mechanism within the larger class of radiofrequency breakdown phenomena. In this section we provide a historical overview of multipactor research, focusing primarily on developments in multipactor which occurred over the last 30 years, and to a lesser extent over the past 90 years. In addition to the historical background provided in this section, interested readers are also referred to review papers by Vaughan [1] and Kishek [2] which provide thorough historical accounts of multipactor research over the decades, up through the time of their respective publications years of 1988 and 1998.

A paper in 1954 by Hatch [3] references early experimental studies of what would later be called multipactor which occurred in the 1920's, and appeared in French- and Germanlanguage publications, as well as some later Swedish-language publications from the early 1940's. The first conceptual description of multipactor phenomenon in American technical literature was in 1934 by Farnsworth [4], who employed multipactor to design an electron multiplier tube capable of producing enough current (in the form of multipacting electrons) to drive a fluorescent screen and produce a television image. A paper in 1948 by Gill [5] provided a theoretical relation between the amplitude, phase, and frequency of the driving field, and the multipactor trajectory length, with Hatch [3] expressing the theory within a more concise mathematical framework and providing comparisons to experimental data. These early theoretical treatments of multipactor assumed very simple secondary electron energy spectra and negligible space charge effects in order for the mathematical relationships of multipactor resonance to be derived; the theory provided by both [3] and [5] assumes a secondary electron energy spectrum which is defined via a proportionality to an incident electron's impact energy. Both [3] and [5] also assume that the driving electric fields only vary in time, and are invariant with respect to the location between the bounding surfaces, as would be the case for an infinite parallel plate geometry.

The theoretical understanding of multipactor advanced in the late 1980's and 1990's with a series of publications by a number of people. Vaughan [1] and Riyopolous [6][7] addressed the theory of multipactor from a phase stability viewpoint, which mathematically showed the conditions under which stable multipactor resonances can occur even in the presence of random fluctuations due to stochastic secondary emission velocities and velocity perturbations due to space charge effects. Riyapolous' second publication [7] also allowed for delay times between an electron impacting a boundary and a secondary electron being emitted.

Kishek [8] and Valfells [9] examined multipactor using a circuit model in which a multipacting device is represented as a parallel plate capacitor, and from this they derived a number of useful theoretical results regarding the total current involved in multipacting electrons, frequency response of multipactor, and the resulting quality factor of a resonator experiencing multipactor. Using this circuit model in addition to the behavior of typical secondary electron yield curves, Kishek [10] also explained a previously unrecognized phase-focusing mechanism influencing multipactor stability, in which multipacting electrons have a tendency to be pushed towards impact energies which maximize the secondary electron yield curve, while at the same time space charge effects tend to defocus the multipacting electrons; space charge saturation occurs when these two competing factors balance and the multipacting electrons have impact energies near the first unity-crossing location on the secondary electron yield curve. Riyopolous [11] provided further analytical and simulation work on the phase focusing and space charge particle debunching phenomenon and how they influence multipactor saturation.

Gopinath [12] utilized the particle-in-cell method to simulate parallel plate multipactor for fully stochastic emission velocities of the secondary electrons, allowing for a study of multipactor evolution from early time, when space charge effects are negligible, up through the late-time steady-state when space charge saturation occurs, for a circuit model allowing for varying Q values. These numerical results agreed quite well with the earlier theoretical results which assumed mono-energetic secondary electrons, thus validating for many circumstances the simplifying assumptions of the prior theoretical analyses.

Besides parallel plate geometries, a second canonical multipactor scenario of interest occurs in coaxial geometries. A pair of companion papers by Udiljak [13] and Semenov [14] respectively provided analytical and particle-in-cell treatments of multipactor in coaxial geometries driven by electric fields, and neglecting magnetic fields. Because the field strength in a coaxial geometries is spatially inhomogenous, no closed-form solution to an electron's trajectory is known, and Udiljak makes some simplifying assumptions to arrive at approximate analytical solutions which are qualitatively useful if not always quantitatively accurate. One interesting phenomenon considered by Udiljak is the existence of single-surface multipactor supported by the outer radius of a coaxial geometry, which is possible due to the ponderomotive force arising from the field inhomogeneity inside a coaxial geometry. Subsequent work by Pérez [15] examined multipactor involving standing, travelling, and mixed transverse electromagnetic modes within coaxial geometries.

Work by Sorolla [16] and Semenov [17] examined the frequency spectrum of fields caused by multipactor current within a parallel plate geometry. Their results were obtained by assuming that multipacting electrons can be treated as a filament of charged particles moving with a periodic velocity; this assumption is not strictly correct because resonance conditions tend to cause multipacting electrons to travel in discontinuous sheets or packets, and not in a continuous filament. Nonetheless, this assumption, along with image theory applied to both conducting parallel plates, allows for results which agree quite well with particle-in-cell simulations applied to the same geometry.

The effect upon multipactor of a perturbative field in addition to the a primary field driving parallel plate multipactor was examined by Semenov [18]. His findings showed that for a perturbative field which is relatively close in frequency to the primary field, multipactor growth can be reduced or eliminated. However, these results are not a definitive conclusion on the matter, due to two main deficiencies which will become more clear in Chapters 3 and 4 of this dissertation. Specifically, Semenov used Vaughan's SEY model, which does not adequately represent incident electrons impacting the surfaces with low energies. Semenov also only examined electron trajectory starting phases which were near the stable starting phase for unperturbed multipactor trajectories; he did not examine the entire range of possible starting phases, some of which could yield stable multipactor trajectories in the presence of a perturbing mode.

Phase-shift keying of the driving field was simulated by Semenov [19] for a parallel plate geometry and by Gonzáles-Iglesias [20] for a coaxial geometry. While some changes were observed in the field strengths at which multipactor resonance occurs, the overall susceptibility to multipactor was not significantly affected. Gonzáles-Iglesias [20] includes comparisons to measured data, which is in good agreement with the simulated results.

Papers by Vdovicheva [21] and Anza [22] examined parallel plate multipactor from a perspective of statistical distributions of electron velocities, which are then modified under the influence of the driving fields and boundary impacts. From this, they determine how multipactor current evolves over time in a statistical sense, as opposed to treating the phenomenon from the perspective as a resonant phenomenon. Anza uses this statistical approach in [23] to provide a theoretical analysis of multipactor susceptibility in the presence of multicarrier signals, such as a multi-channel satellite antenna. A subsequent paper by Anza [24] compared his statistical analysis to measured data of multipactor onset within actual microwave components, and he showed respectable agreement as to the field strengths which give rise to multipactor.

In addition to simple canonical geometries, work has been published which extends the traditional two-point multipactor analyses to more complicated multipactor scenarios. Kryazhev [25] and Riyopoulos [26] analyzed multipactor in parallel plate geometries and demonstrated that under certain conditions it is possible to have stable asymmetric back-and-forth orbits, in which the time duration of one leg of the trajectory takes a different amount of time than another leg of the trajectory. Shemelin [27] generalized the phase stability criterion from two-point multipactor occurring over one radiofrequency period to an arbitrary N-point multipactor occurring over an arbitrary number of radiofrequency periods. Kishek [28] used analytical theory and the particle-in-cell method to study the stability of N-point multipactor in field conditions where the traditional two-point multipactor theory fails to predict sustainable multipactor. Semenov [29] generalized the traditional parallel plate analysis by providing a theoretical analysis of multipactor within a rectangular waveguide geometry, and showed that the higher-order multipactor trajectories can be significantly affected by the oscillating magnetic field; this magnetic field usually has a negligible impact on low-order multipactor trajectories because the multipacting electrons are not moving at relativistic speeds, and the magnetic force is proportional to v/c, where v is magnitude of the particle velocity and c is the speed of light.

Two papers by Rasch [30][31] examined two-point multipactor between the convex surfaces of two conducting cylinders, and how the surface curvature affects the multipactor susceptibility. Semenov [32] extended this analysis to any two conducting surfaces with geometries that are defined by curves in a two-dimensional plane, and which are invariant in the direction normal to the plane. These analyses generalize the traditional parallel plate multipactor analysis found in [1], [3], and [5]. Surface curvature was included in these analyses by the introduction of a focusing or defocusing factor for the multipactor trajectories, similar to how ray optics treats the convergence or divergence of rays reflected from a curved surface, with the important distinction that ray optics is characterized by specular reflections, whereas the multipactor trajectories in these analyses are assumed to emerge normal to the conducting surface. Such an assumption for the emission trajectories can be justified if the secondary electron emission velocities are small, but this assumption can still introduce non-trivial errors in certain cases, which the authors demonstrate by a comparison with Monte Carlo multipactor simulations using stochastic emission velocities. Despite an inability to provide quantitative multipactor susceptibility predictions in all circumstances, this geometrical analysis can provide qualitative insight into why certain geometrical structures are more or less prone to two-surface multipactor than are infinite parallel plates.

1.3 Description of this dissertation

This dissertation details the results of numerical study of multipactor, with a specific focus upon how secondary electron emission models can affect the resulting multipactor predictions, and how multipactor susceptibility and trajectories can be affected by the presence of additional modes within a resonant structure. The primary focus is 2-point multipactor occurring between the inner and outer conductors of coaxial geometries, but some parallel plate geometries are also considered. However, there is nothing in the underling physics which is specific to 2-point multipactor, and the results are thus expected to be generalizable to many n-point multipactor scenarios.

The scope of investigation is limited to the multipactor regime in which space charge effects can be neglected. In practice this means the early-time evolution of multipactor, since it takes some time before space charge effects become significant. Despite this simplifying assumption not being applicable to the late-time behavior of multipactor, this approach still allows for much practical benefit in the understanding of multipactor genesis and controllability, which is frequently the most significant concern of engineering interest.

1.4 Organization of this dissertation

This dissertation is organized into seven chapters, with this introduction being Chapter 1. Chapter 2 provides an overview of the theoretical and computational methodology that multipactor initiation can be studied in the absence of space charge effects. The resonance conditions which give rise to multipactor are discussed, as well as the relationship between multipactor and the secondary electron yield (SEY) of surfaces sustaining multipactor. Analytical and numerical approaches to analyzing multipactor are then discussed.

Chapter 3 presents various secondary electron emission (SEE) models which are fundamental to any further study of multipactor initiation or sustainability. The models we consider are not intended to be an exhaustive list of all possible SEE models, but were chosen either because of their popularity within various technical communities, or other attractive qualities such as conceptual or computational simplicity. These models are loosely presented in order of least complex to most complex, in terms of both the SEY curves and the secondary electron emission energy spectra. The exception to this order of presentation is that the final SEE model, termed the medianized Furman SEE model, is a simplified variant of the most complex SEE model, the Furman SEE model. This medianized variant is defined in a deterministic way so as to capture much of the behavior of the more complicated stochastic model without needing to resort to Monte Carlo simulations.

Chapter 4 examines to what extent multipactor resonance is affected by the presence of an additional mode alongside the fundamental mode which is primarily driving the multipactor, for circumstances in which the space charge effects are negligible. Metrics are introduced to quantify the multipactor susceptibility over a distributed volume such as a cavity or a length of waveguide, in order to avoid erroneously concluding that we are able to improve multipactor performance based on an examination of only one location within a resonant structure; if we look at only one location, then we are neglecting how an additional mode may be negatively affecting multipactor performance at other locations in the structure.

In Chapter 5 we generalize the medianized Furman SEE model by using cumulative statistics other than the 50^{th} percentile of the underlying emission distribution, and examine how well multipactor predictions using this generalized medianized Furman SEE model agree with the fully stochastic Furman model. These results suggest that different design or analysis goals for a resonant structure may be best attained by using different cumulative statistics from the underlying Furman SEE model when reducing the model from a stochastic to a deterministic model.

Chapter 6 addresses the question of whether or not the impact points on a surface of multipacting particles can be controlled via the presence of a higher-order mode. It is shown that under circumstances in which a higher-order mode has a much stronger magnetic field than the fundamental mode, then the multipactor impact points can be controlled under many circumstances. Such an ability to steer the location of multipactor points would have a practical applications, for example deflecting multipactor current away from a sensitive area in a device and towards areas able to tolerate or even suppress the multipactor because of geometrical factors or surface treatments.

Chapter 7 concludes this dissertation with a summary of the results obtained, and possible directions for future research in this area.

CHAPTER 2: Approaches Towards Analyzing Multipactor Initiation

2.1 Multipactor review

Multipactor is a resonant phenomenon in which an electromagnetic field causes a free electron to impact a surface, resulting in the surface emitting secondary electrons. If the surface geometry and electromagnetic fields are appropriately arranged, the secondary electrons can then be accelerated and again impact a surface in the bounding geometry. If the net number of secondary electrons participating in multipactor is non-decreasing, then the process can repeat indefinitely. Expressed concisely, in order to initiate and sustain multipactor, we must satisfy the following two conditions: (1) The secondary electron yield must be greater than or equal to unity when averaged over the entire ensemble of multipacting electrons, and (2) the system geometry and field excitation must result in electrons impacting boundaries at the proper RF phase, such that secondary electrons emerge to find a field phase which will again accelerate them into a boundary to create more secondary electrons. These two conditions have naturally resulted in approaches to multipactor control which have respectively focused on (1) surface treatments to modify the secondary electron yield, and (2) geometry and field modifications to affect the multipactor resonance [36].

When plotted as a function of the kinetic energy of the incident electrons, secondary electron yield (SEY) curves typically have shape with a maximal SEY value at an intermediate incident kinetic energy, and low SEY values for low and high incident kinetic energies, as shown in Figure 2. For most metals of engineering interest, the first unity-valued point on the SEY curve (denoted as E_{min} in Figure 1) is on the order of 100 eV, and the second unity-valued point on the SEY curve (denoted as E_{max} in Figure 1) is on the order of 1000 eV [33]. These unity-valued points frequently are respectively called the first and second crossover points in the literature, and the SEY is also frequently referred to as δ in the literature. Parametric models to fit this curve have been presented by Vaughan [34] and Furman and Pivi [35]. It is also important to note that secondary electrons can also be induced not only by incident electrons, but also by other incident particles such as ions [49]; we limit our consideration only to incident electrons in this dissertation, which is typical of most analyses of multipactor in the literature.

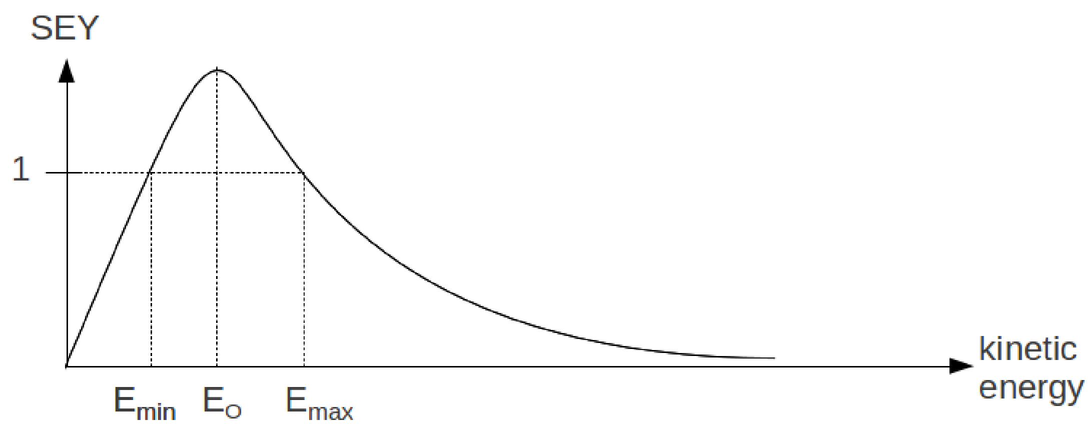

Figure 2: SEY Curve. A Secondary Electron Yield (SEY) curve as a function of incident electron kinetic energy. E_{min} and E_{max} are commonly called the first and second crossover points, and the SEY is sometimes represented by the Greek letter δ in the literature.

Besides having an SEY that meets or exceeds unity, the system geometry and field excitation must be conducive to sustaining the multipactor. This can perhaps be most easily conceptualized by considering two parallel conductor plates separated by a distance *d*, and driven by an alternating voltage of $V(t) = V_o \sin(\omega \cdot t+\theta)$ as shown in Figure 3, where V_o denotes the voltage scaling, ω denotes the angular frequency, t denotes time, and θ denotes initial phase. An electron of charge q and mass m_e would undergo an acceleration described by:

$$\ddot{x}=\frac{q \cdot V_o}{m_e \cdot d} \sin(\omega \cdot t+\theta) . \tag{2.1}$$

For an electron starting at $x=0$ with no initial velocity, by solving Equation (2.1) subject to the constraint that the electron arrives at the far plate at $x=d$ at N half periods later for N odd, we arrive at the gap-frequency constraint for two-point multipacting [1][36]:

$$d^2 \cdot \omega^2=\frac{q \cdot V_o}{m_e} \cdot (2 \sin(\theta) + N \pi \cdot \cos(\theta)) . \tag{2.2}$$

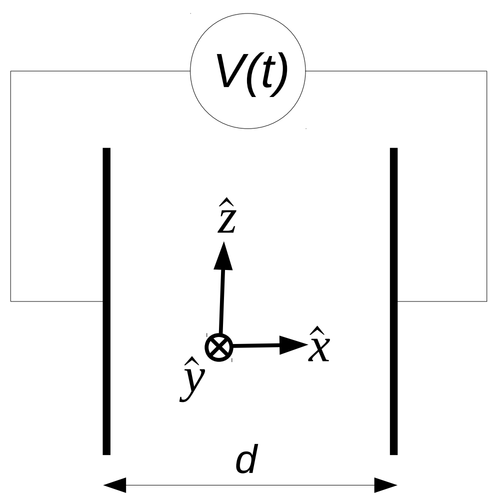

Figure 3: Basic parallel plate geometry

Equation (2.2) was derived under the assumptions that the field is spatially uniform, the particle can only move in one dimension, the initial velocity of secondary electrons is zero, and the particle traverses the gap in a half RF period. These assumptions can be violated to varying degrees in real-world multipacting. See Vaughan [1] for a more general analysis of the geometry and phase conditions necessary to sustain parallel plate 2-point multipactor. However, Equation (2) does allow us to concisely express how frequency, phase, field strength, and geometry are related to sustain two-point multipacting under the limiting assumptions.

2.2 Analytical treatment of parallel plate geometries

This section builds upon the work presented by the author in [37].

In this section we consider an analytical treatment of multipactor trajectories with some approximations to make the problem analytically feasible. Multipactor in general is a very complicated process, with space charge effects resulting in a nonlinear time-varying system, and the secondary electron emission process ultimately being stochastic due to the effects of quantum mechanics as asserted in [35], and more frequently due to uncharacterized surface imperfections and contamination in practice [36]. Nonetheless, with some modest approximations and assumptions, a mathematical model of multipactor trajectories can be developed for the case of negligible space charge effects. Such a model can provide good insight into multipactor initiation, which frequently occurs when space charge density is small or non-existent.

Consider the parallel plate geometry as shown above in Figure 3, where the plates are assumed infinite in the y- and z-directions. Assume that the electric field between the plates is time-varying, but not dependent upon position. To allow for additional generality beyond a simple parallel plate capacitor analysis, we allow for a nonzero magnetic field that is transverse and proportional to the electric field. We can also consider externally-imposed electric and magnetic fields to be present, respectively denoted as $\mathbf{E_{ext}}$ and $\mathbf{B_{ext}}$. Without loss of generality, the total electric field $\boldsymbol{E}$ and magnetic field $\boldsymbol{B}$ can then be expressed as:

$$\boldsymbol{E} = \hat{x}\, E_0 \cos(\omega t + \theta) + \boldsymbol{E_{ext}} \tag{2.3}$$

$$\boldsymbol{B} = \hat{y}\, \frac{\alpha}{c} E_0 \sin(\omega t + \theta) + \boldsymbol{B_{ext}} \tag{2.4}$$

where t denotes the time, θ is an arbitrary phase, α is a unitless scaling factor to allow for arbitrary magnetic field strength and sign relative to the electric field, c is the speed of light in free space. In practice constant (DC) $\mathbf{E_{ext}}$ and $\mathbf{B_{ext}}$ have been used to modify multipactor [36], but this is not always possible for a given design constraint; throughout this dissertation we will assume that $\mathbf{E_{ext}}$ and $\mathbf{B_{ext}}$ are zero. The above choice of magnetic field will allow our parallel plate fields to be considered as the limiting case of the TEM mode standing waves within a coaxial cavity, and will therefore provide some insight into not only rectangular geometries, but to coaxial geometries as well.

To understand how the field expressions in equations (2.3) and (2.4) are related to coaxial cavity fields, consider the conducting coaxial geometry as shown in Figure 4, with ends that are shorted from the inner and outer conductors. For this coaxial geometry, the TEM mode standing waves in phasor form are:

$$\boldsymbol{E_{coax}} = \hat{r} \frac{V_o}{r \log(b/a)} \sin(\beta_z\, z) \cos(\omega\, t + \theta) \tag{2.5}$$

$$\boldsymbol{B_{coax}} = -\hat{\phi} \frac{V_o}{c\, r \log(b/a)} \cos(\beta_z\, z) \sin(\omega\, t + \theta) \tag{2.6}$$

where V_o is field scaling factor in units of volts, r is the radial position as measured from the central axis, z is the position along the axis, b is the outer conductor radius, a is the inner conductor radius, β_z is the wavenumber of the TEM mode, ω is the angular frequency of the temporal mode, θ is the temporal phase, c is the speed of light in free space, and log() denotes the natural logarithm. The unit vectors $\hat{r}$ and $\hat{\phi}$ respectively denote the radial and circumferential directions in the coaxial geometry.

To see how Equations (2.3) and (2.4) are the limiting cases of Equations (2.5) and (2.6), let the radial distance between the inner and outer conductor in the coaxial geometry be equal to a fixed d, such that $b = a + d$. Then for $a \to \infty$, we we have $d << a$, and letting $r = a + \Delta r$ where $\Delta r \leq d$, we have that $r \cdot \log(b/a) = (a+\Delta r) \cdot \log(1+d/a) \to (a+\Delta r) \cdot (d/a) \to d$. We then have:

$$\lim_{r\to\infty} \boldsymbol{E}_{coax} = \hat{r} \frac{V_o}{d} \sin(\beta_z z) \cos(\omega t + \theta) \tag{2.7}$$

$$\lim_{r\to\infty} \boldsymbol{B}_{coax} = -\hat{\phi} \frac{V_o}{c\,d} \cos(\beta_z z) \sin(\omega t + \theta) \tag{2.8}$$

Finally by noting that we can consider $\hat{r} \to \hat{x}$ and $\hat{\phi} \to \hat{y}$ as $a \to \infty$, and with appropriate choices of α and E_0, we can express Equations (2.7) and (2.8) in the form of Equations (2.3) and (2.4). We have thus established that the form of the rectangular-coordinate fields given by Equations (2.3) and (2.4) are in general the large-radius limiting case for coaxial TEM fields at a fixed longitudinal (z) position along the coaxial cavity.

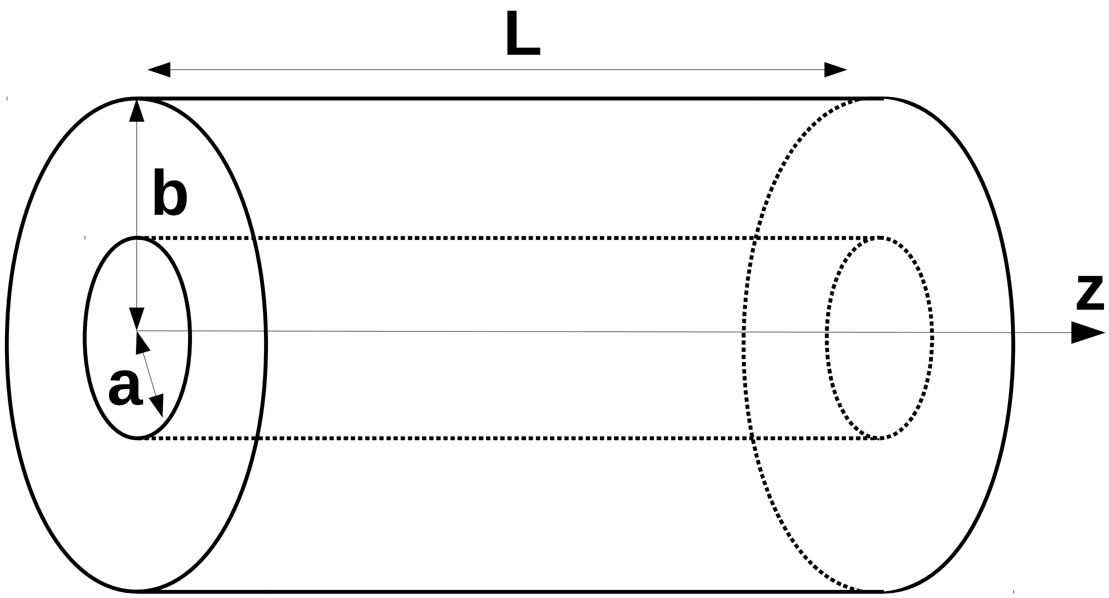

Figure 4: Coaxial cavity geometry. Dimensions are length L, inner radius a, and outer radius b.

Returning back to the parallel plate geometry, let us now consider the forces that the electric and magnetic fields will impart to a particle of charge q. The forces $\boldsymbol{F_E}$ and $\boldsymbol{F_B}$ respectively due to the electric and magnetic fields are given by:

$$\boldsymbol{F_E} = q\boldsymbol{E}(t) = \hat{x} q E(t) \quad (2.9)$$

$$\boldsymbol{F_B} = q\boldsymbol{v} \times \boldsymbol{B}(t) = q(\hat{x}\dot{x} + \hat{z}\dot{z}) \times \hat{y} B(t) = qB(t)(\hat{z}\dot{x} - \hat{x}\dot{z}) \quad (2.10)$$

where $\boldsymbol{v}$ denotes the velocity, $\dot{x}$ and $\dot{z}$ respectively denote the time derivatives of the x and z positions of the particle, and the operation $\times$ denotes the vector cross product. These forces will result in accelerations $\ddot{x}$ and $\ddot{z}$ respectively along the x and z directions as follows:

$$\ddot{x} = qE(t) - \dot{z}\frac{q}{m}B(t) \tag{2.11}$$

$$\ddot{z} = \dot{x}\frac{q}{m}B(t) \tag{2.12}$$

These equations can be expressed more concisely in matrix notation as the following:

$$\begin{bmatrix} \ddot{x} \\ \ddot{z} \end{bmatrix} = \begin{bmatrix} 0 & \frac{-q}{m}B(t) \\ \frac{q}{m}B(t) & 0 \end{bmatrix} \begin{bmatrix} \dot{x} \\ \dot{z} \end{bmatrix} + \begin{bmatrix} \frac{q}{m}E(t) \\ 0 \end{bmatrix} = A(t) \begin{bmatrix} \dot{x} \\ \dot{z} \end{bmatrix} + \begin{bmatrix} \frac{q}{m}E(t) \\ 0 \end{bmatrix} \tag{2.13}$$

From linear systems theory [38][39], we know that the homogenous solution for $[\dot{x} \;\; \dot{z}]^T$ in the above system can be expressed via an (as yet unknown) state transfer function $\Phi(t, t_o)$ via:

$$\begin{bmatrix} \dot{x}(t) \\ \dot{z}(t) \end{bmatrix} = \Phi(t,0) \begin{bmatrix} \dot{x}(t=0) \\ \dot{z}(t=0) \end{bmatrix} \tag{2.14}$$

Since $A(t_1)A(t_2) = A(t_2)A(t_1)$, we have [38]:

$$\Phi(t, t_0) = \exp\left(\int_{t_0}^{t} A(\tau) d\tau\right)$$

$$= \exp\left(\begin{bmatrix} 0 & -\int_{t_0}^{t} \frac{q}{m} B(\tau)\, d\tau \\ \int_{t_0}^{t} \frac{q}{m} B(\tau)\, d\tau & 0 \end{bmatrix}\right) \tag{2.15}$$

We can simplify equation (2.15) by applying the relation

$$\exp\left(\begin{bmatrix} 0 & -\gamma \\ \gamma & 0 \end{bmatrix}\right) = \begin{bmatrix} \cos(\gamma) & -\sin(\gamma) \\ \sin(\gamma) & \cos(\gamma) \end{bmatrix} \tag{2.16}$$

which results in:

$$\Phi(t, t_0) = \begin{bmatrix} \cos\left(\int_{t_0}^{t} \frac{q}{m} B(\tau)\, d\tau\right) & -\sin\left(\int_{t_0}^{t} \frac{q}{m} B(\tau)\, d\tau\right) \\ \sin\left(\int_{t_0}^{t} \frac{q}{m} B(\tau)\, d\tau\right) & \cos\left(\int_{t_0}^{t} \frac{q}{m} B(\tau)\, d\tau\right) \end{bmatrix}. \tag{2.17}$$

The complete non-homogenous solution for $[\dot{x} \quad \dot{z}]^T$ is then given by:

$$\begin{bmatrix} \dot{x}(t) \\ \dot{z}(t) \end{bmatrix} = \Phi(t, 0) \begin{bmatrix} \dot{x}(t=0) \\ \dot{z}(t=0) \end{bmatrix} + \int_{0}^{t} \Phi(t, \tau) \begin{bmatrix} \frac{q}{m} E(\tau) \\ 0 \end{bmatrix} d\tau$$

$$= \Phi(t,0)\begin{bmatrix}\dot{x}(t=0)\\ \dot{z}(t=0)\end{bmatrix} + \int_0^t \begin{bmatrix}\frac{q}{m}E(\tau)\cos\left(\int_\tau^t \frac{q}{m}B(\sigma)d\sigma\right)\\ \frac{q}{m}E(\tau)\sin\left(\int_\tau^t \frac{q}{m}B(\sigma)d\sigma\right)\end{bmatrix} d\tau \qquad (2.18)$$

The nested integrals in equation (2.18) are not evaluable in closed form for time-harmonic fields, but this analytic expression does provide a solution to check numerical methods against in special circumstances.

2.3 Numerical treatment of multipactor initiation

In practice, analytical treatments of multipactor are rarely used for real-world multipactor analysis once the geometries and field conditions become more complex. To handle this, we resort to numerical methods.

In general, for a charged particle interacting with a specified electromagnetic field, the particle state at any given instant in time can be represented as a six-dimensional vector which contains the particle's three space coordinates and three velocity components. This can be expressed mathematically as:

$$\begin{bmatrix}\dot{x}(t)\\ \dot{y}(t)\\ \dot{z}(t)\\ \ddot{x}(t)\\ \ddot{y}(t)\\ \ddot{z}(t)\end{bmatrix} = \frac{q}{m}\begin{bmatrix}0&0&0&1&0&0\\ 0&0&0&0&1&0\\ 0&0&0&0&0&1\\ 0&0&0&0&B_z(\boldsymbol{r},t)&-B_y(\boldsymbol{r},t)\\ 0&0&0&-B_z(\boldsymbol{r},t)&0&B_x(\boldsymbol{r},t)\\ 0&0&0&B_y(\boldsymbol{r},t)&-B_x(\boldsymbol{r},t)&0\end{bmatrix}\begin{bmatrix}x(t)\\ y(t)\\ z(t)\\ \dot{x}(t)\\ \dot{y}(t)\\ \dot{z}(t)\end{bmatrix} + \frac{q}{m}\begin{bmatrix}0\\ 0\\ 0\\ E_x(\boldsymbol{r},t)\\ E_y(\boldsymbol{r},t)\\ E_z(\boldsymbol{r},t)\end{bmatrix} \qquad (2.19)$$

where q is the particle charge, m is the particle mass, $\boldsymbol{r}$ denotes the particle's position (x, y, z), $B_{x,y,z}$ denotes the magnetic field components, and $E_{x,y,z}$ denotes the electric field components. The system defined in (2.19) can be solved via a standard differential equation system solver. For the results presented in this dissertation, Matlab's built-in ode45() function [40][41] was employed to solve for the particle trajectories as a function of time. The ode45() function is an adaptive-step-size solver which uses the Dormand-Prince method to compute fourth- and fifth-order accurate solutions to the underlying differential equation system, and compares the difference to estimate the solution error. The Matlab ode45() function also has built-in capability for defining conditions at which to terminate the system solver; this capability was used to end a particular ode45() instance when a particle's distance to a boundary surface goes to zero, signifying that a boundary strike occurred.

CHAPTER 3: Secondary Electron Yield Models

3.1 Introduction

The formation of multipactor is strongly dependent upon the secondary electron yield (SEY) of a surface contributing to multipactor, and the emission velocities of the emitted electrons. In this chapter, we examine different possible approaches to modeling the SEY and emission velocities. In order of increasing complexity, we examine the effects of the following secondary electron emission (SEE) models upon multipactor susceptibility: boxcar (passband) SEY model with zero emission energy, Vaughan's SEY curve [34] with zero emission energy, Vaughan's SEY curve with nonzero emission energy, and Furman's SEE model [35]. We also propose a simplified version of Furman's model in which the stochastic emission process is replaced by a deterministic emission process which achieves respectable agreement with Furman's fully stochastic model; this is of considerable computational interest because it allows us to avoid the more costly Monte Carlo simulations required to generate results from a stochastic model.

3.2 Coaxial cavity geometries used in this dissertation

For all of the results presented in this chapter, and in much of the results in this dissertation, we utilize coaxial cavity geometries which are shorted at both ends, as shown in Figure 5. For such geometries, the TEM mode electric field ***E***(r,z,t) and magnetic field ***B***(r,z,t) can be expressed as:

$$\boldsymbol{E}=\hat{r}\frac{V_0}{r\cdot\log(b/a)}\cdot\cos(\omega t+\theta)\cdot\sin\left(\frac{n\pi z}{L}\right), \tag{3.1}$$

$$\boldsymbol{B} = -\hat{\phi}\frac{1}{c}\frac{V_0}{r \cdot \log(b/a)} \cdot \sin(\omega t + \theta) \cdot \cos\left(\frac{n\pi z}{L}\right), \qquad (3.2)$$

where a cylindrical coordinate system (r, ϕ, z) is assumed for radial position r (meters), azimuthal position ϕ (radians), and axial position z (meters), V_0 denotes a field scaling parameter (Volts), t denotes time (seconds), ω represents the angular frequency (radians/second), θ represents the field temporal phase (radians), n represents the harmonic number (integer), L represents the cavity length along the axial direction (meters) such that $0 \leq z \leq L$, a and b respectively denote the inner and outer conductor radii (meters), c is the speed of light in free space (meters/second), carats (^) over a coordinate denote unit vectors in this cylindrical basis, and boldface quantities denote vectors.

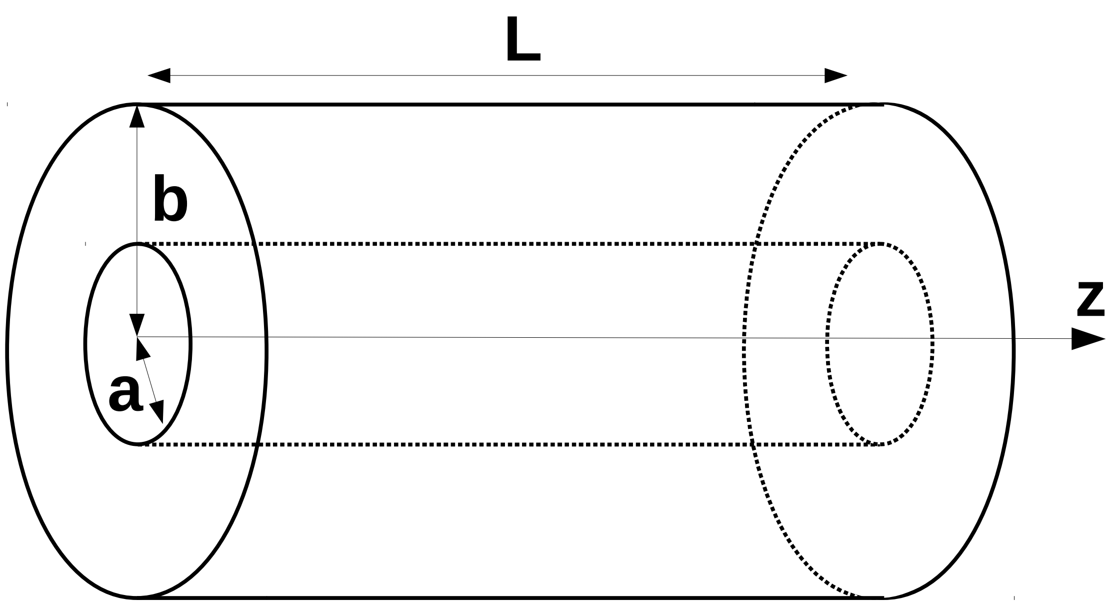

Figure 5: Coaxial cavity geometry. Dimensions are length *L*, inner radius *a*, and outer radius *b*.

We employ two coaxial geometries for most of the results generated throughout this dissertation. Both geometries have a length L=1.86 meters, which corresponds to a fundamental (n=1) TEM mode resonance at 80.5 MHz; this specific resonant frequency was chosen to match the design frequency of quarter-wave resonators used in the beamline of the Facility for Rare Isotope Beams particle accelerator facility [42]. Coaxial geometry #1 has an inner radius a=0.01 meters, and an outer radius b=0.056472 meters; these radii were chosen to yield two-boundary multipactor between the inner and outer conductors for V_0 on the order of 1000 V. Coaxial geometry #2 has radii that are 3x greater than the first coaxial geometry, specifically an inner radius a=0.03 meters, and an outer radius b=0.169416 meters. This second geometry was chosen to provide some diversity of geometry in order to assess how the simulated results change when the geometry is changed.

When simulating multipactor trajectories within coaxial cavities, throughout the entire dissertation, we simulate particles which start at t=0 with zero velocity from r=b-ε (recall that r=b is the outer wall), where ε=1 nm is a small radial starting offset so that the code can identify a boundary crossing if the fields immediately push the particle across the boundary. This same radial offset ε is used whenever a particle strikes a boundary and results in a secondary electron being emitted from the boundary; however, in the case of secondary emission, the particle may have a non-zero starting velocity depending on the secondary emission model used, as discussed in later sections. Unless specified otherwise, all trajectories in this dissertation start from z=L/2 (halfway between cavity end caps); the exception to starting at z=L/2 is when we examine multipactor breakdown over distributed volumes within coaxial cavities and waveguides respectively in sections 4.3 and 4.4. Throughout this dissertation, we frequently use the generic term “particle” interchangeably with electron, since in this dissertation we exclusively simulate particles with the same charge-to-mass ratio as an electron, with one minor difference: Even though electrons have a negative charge, without loss of generality, we consider particles which are positively-charged and have the same ratio of mass to absolute charge as an electron. This results in the particle acceleration being in the same direction as the electric fields and not opposite the field direction as would occur for a negatively-charged electron; the resulting effect in the simulations is that for a negatively-charged electron, we would just need to include a phase shift of 180º in our field definitions to yield identical results. Also because we only consider TEM modes, the coaxial fields are rotationally-invariant and do not change with ϕ position. Finally, even though we typically examine coaxial cavities, the conclusions are expected to be generalizable for any two-boundary multipactor.

The specific parameters being varied and their sampling discretizations will be specified in each chapter, and will vary depending on the purpose of the simulations in that chapter. For both of the cavity results in this chapter, we allow θ to range from $-\pi/2$ to $\pi/2$ over 181 points. Also in this chapter, with cavity #1 we allow V_0 to vary from 10 V to 3000 V in steps of 10 V; with cavity #2 we allow V_0 to vary from 50 V to 30000 V in steps of 50 V.

As a point of comparison, equation (2.2) gave a relationship for two-surface multipactor resonance in parallel plate geometries. If we let $d=b-a$ and assume that equation (2.2) approximately holds for the coaxial geometries under consideration, then for a starting phase of $\theta=0$, equation (2.2) yields the following approximate predicted multipactor resonant voltages:

$$V_o = \frac{d^2 \cdot \omega^2 m_e}{q N \pi} \,. \tag{3.1}$$

Based on this relation, and recalling that N must be an odd integer corresponding to the number of half-periods the particle is in transit between the conductors, the approximate voltages V_o for the first few two-point multipactor resonances in both cavities are as shown below in Table 1.

N =	1	3	5
cavity #1 V_o:	1477 V	492 V	295 V
cavity #2 V_o:	13.29 kV	4.43 kV	2.66 kV

Table 1: Approximate peak voltages V_O to achieve multipactor resonances. Shown are the first three volage resonance conditions for half periods N={1,3,5}, for cavity #1 and cavity #2, based upon the parallel plate resonance condition.

3.3 Net SEY

For each simulated multipactor trajectory, we are only tracking a single particle, which is understood to have the same absolute charge-to-mass ratio as an electron, but which can represent any fractional number of electrons. The number of electrons that the particle represents is equal to the product of all the SEY values for each boundary impact that the trajectory experiences, and we call this product the net SEY. If the net SEY is greater than unity, or equivalently if the log(net SEY) is greater than zero, then this represents a net growth of secondary electrons over the simulated multipactor trajectory. This net SEY is used throughout this dissertation, and frequently is the starting point to understanding multipactor susceptibility.

Throughout this dissertation, we compute the net SEY as show in Figure 6 below, and explained as follows: we simulate particle trajectories for 10 cycles, where a cycle is defined to be one period of the fundamental mode, or one boundary impact, whichever occurs first. The net SEY is defined as the product of each single-impact SEY, and is understood to be zero if at least two boundary impacts do not occur over the simulation period. Note that the net SEY is different from the multipactor growth rate, because the net SEY does not take into account how long a trajectory is tracked in order for 10 cycles to complete. The growth rate of multipactor can be determined by taking the natural logarithm of the net SEY and dividing this value by the time of final boundary impact, as will be explained in Section 3.9 of this dissertation.

Note that some SEE models are stochastic, such that after an incident electron strikes a material, the SEE model may yield a random number of secondary electrons, each with their own initial velocity. When simulating a multipactor trajectory with such stochastic SEE models, one of the secondary electrons is chosen at random to continue the multipactor trajectory. With such stochastic SEE models, a series of Monte Carlo simulations are used to generate a large number of possible multipactor trajectories and associated net SEY values, which are then considered using statistical metrics such as the mean or median net SEY.

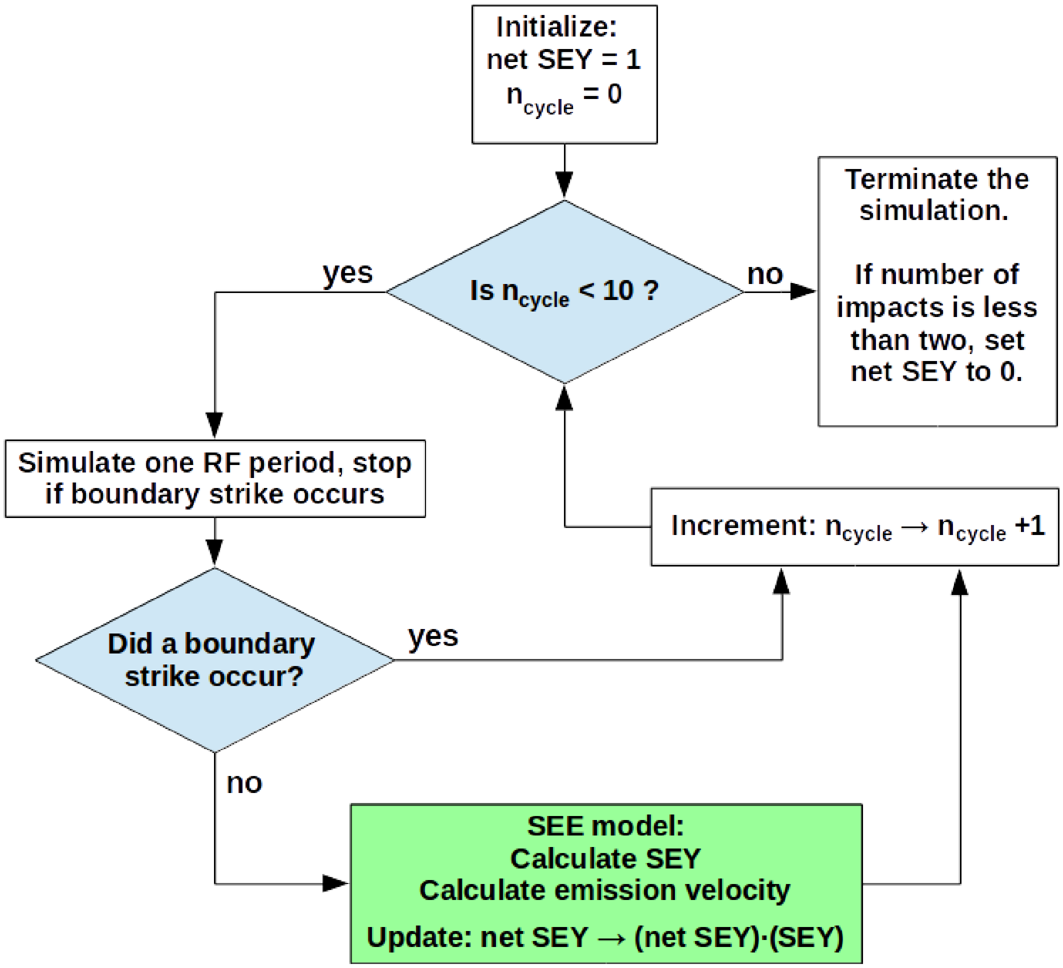

Figure 6: Process for calculating the net SEY. This process must be undertaken for each unique field condition. The effect of changing the SEE model (green block) is the focus of the succeeding sections in this chapter.

3.4 Boxcar SEE model with zero emission energy

The first SEE model to be considered is termed the boxcar (passband) SEY, which is simply unity for electrons with impact energies between 27.32 eV and 3018.5 eV, and is zero otherwise, as shown in Figure 7 below. These specific thresholds were chosen to match the unity-crossing points of the SEY curve in Furman's SEE model [35] for copper. The emitted secondary electrons are defined to have zero emission velocity. This SEE model is based upon a crude approximation to the SEY curve of most metals of engineering interest, which have an SEY greater than unity (and thus supporting multipactor) for incidence energies within a passband similar to this notional boxcar model, and with an emission energy spectrum dominated by emitted electrons which are much less energetic than the incident electrons.

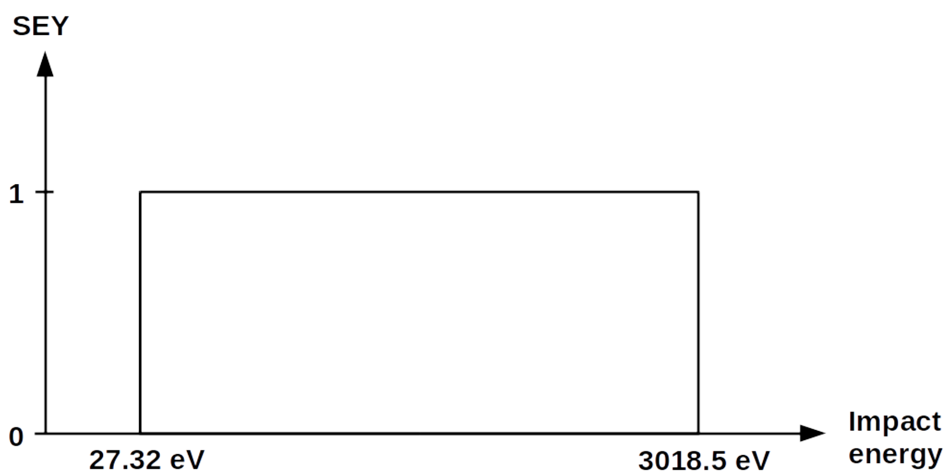

Figure 7: Boxcar SEY curve.

The results for the multipactor simulations of coaxial geometries #1 and #2 are shown respectively in Figures 8 and 9 below. For consistency of presentation, these results are plotted on the same logarithmic scale as future results with more sophisticated SEE models, despite the boxcar SEE model only yielding net SEY values of 0 or 1. Both of these results predict regions of multipactor stability, which is consistent with the idea of multipactor being a resonant phenomenon which occurs only over certain field strength ranges for a given geometry and excitation frequency. Each surface shows bands of multipactor stability, where the rightmost band corresponds to one-way transit times of a single half-period, the next rightmost band corresponds to one-way transit times of three half-periods, and so on. Coaxial geometry #2 shows a more complex resonance structure; this is due to the wider inner-to-outer conductor gap which allows more opportunities for the particle transit times to be an odd integer multiple of the electric field period, as well as the ability for a particle starting at a given phase to eventually phase-lock with the driving fields and impact the boundaries at energies corresponding to a nonzero SEY for each impact. The sharp transitions in these figures between multipactor resonance and non-resonance conditions are due to the discontinuous SEY curve which discards any trajectories with an incident electron yielding a zero SEY value. When more physically accurate SEE models are examined in future sections, we will see that these sharp transitions are smoothed out.

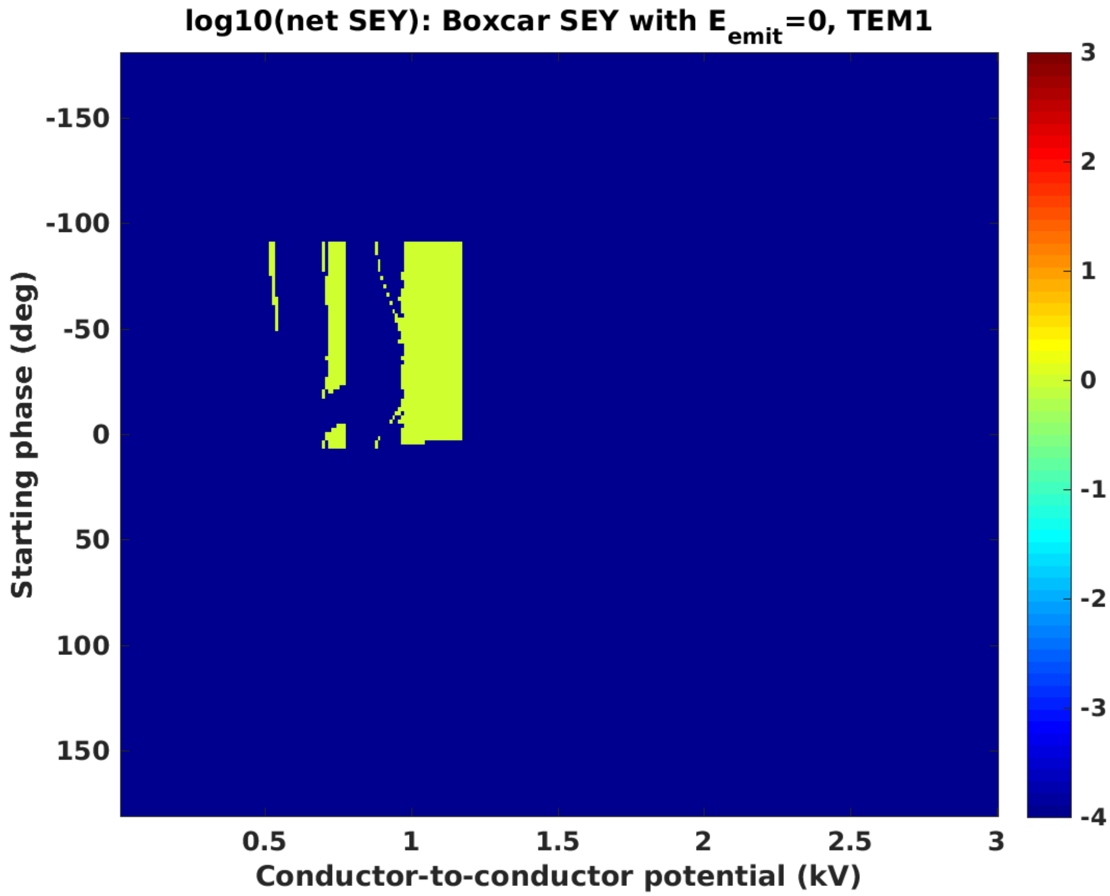

Figure 8: Net SEY surface for boxcar SEY model and coaxial geometry #1.

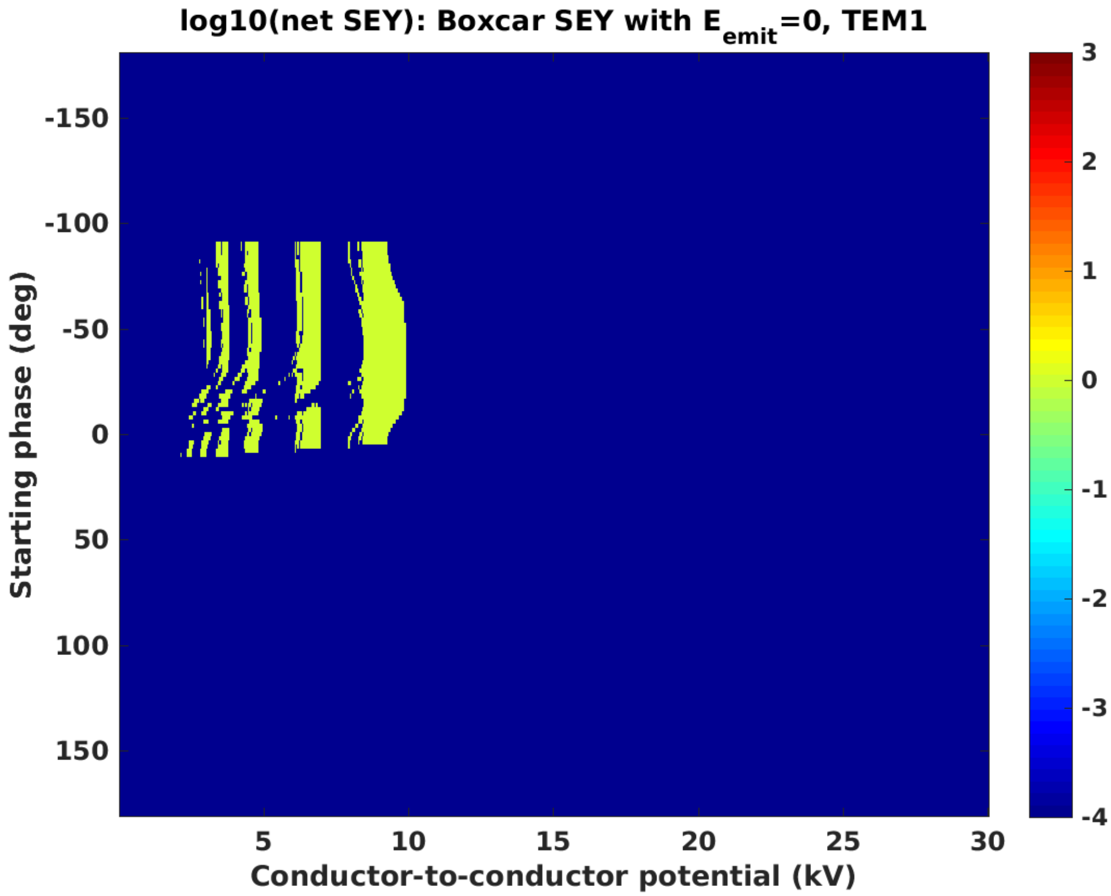

Figure 9: Net SEY surface for boxcar SEY model and coaxial geometry #2.

3.5 Vaughan model with zero emission energy

We next examine Vaughan's SEY model [34] , which is a popular SEY model within the microwave device community. Vaughan's model is relatively simple, being parameterized by only about 10 parameters, and if we use Vaughan's suggested values for some of the less critical parameters, we are then left with only 4 parameters to characterize any given material. One important feature of Vaughan's model is that the SEY is set to zero below a certain threshold impact energy. Vaughan proposes a 12.5 eV threshold, which was used in this present research.

In order to simulate the copper material used throughout this dissertation with Vaughan's model, and using the same variable names as provided by Vaughan, we use a first crossover incident energy V_1=27.32 eV, a second crossover incident energy V_2=3018.5 eV, a peak incident energy V_{max}=277.5 eV, and a peak SEY δ_{max}=2.0887; all of these values are understood to be for normal-incidence, and Vaughan's model adjusts them as a function of incidence angle. These values were chosen so that at zero incidence, the location and peak of the SEY curve matched the SEY curve for copper as generated for Furman's SEY model, which will be discussed in Section 3.7; plots showing Vaughan's SEY curve and Furman's SEY curve are shown in Figure 14, in which the thresholding effect of Vaughan's SEY curve is clearly seen in the right plot. Note that the crossover energies provided by Vaughan are presented in his paper to be the same as the crossover energies as shown in Figure 2, but an examination of Vaughan's parametric fitting shows that his SEY curve does not pass through unity at the first crossover point, but rather balances an approximation to a real SEY curve over an extended interval.

Vaughan's model only provides a SEY curve, it does not provide the energy and angular distribution for the emitted electrons. In this section, we examine results using Vaughan's model with emitted secondary electrons defined to have zero velocity. Since the majority of secondary electrons are emitted with a few eV of initial energy, this zero-energy approximation will typically have marginal impact.

Figures 10 and 11 below respectively show the results for the multipactor simulations of coaxial geometries #1 and #2. In comparison with the simple boxcar SEY model of the previous section, we note more complex multipactor susceptibility surfaces characterized by a continuum of net SEY values, which the simple boxcar SEY curve could not provide because it can only yield a binary 0 or 1 value. As with the boxcar SEY results, coaxial geometry #2 shows a more complex resonance structure, again due to the wider inner-to-outer conductor gap which allows more opportunities for the particle transit times to be an odd integer multiple of the electric field period, as well as the ability for a particle starting at a given phase to eventually phase-lock with the driving fields and impact the boundaries at energies corresponding to a nonzero SEY for each impact. The present SEY model again shows sharp transitions between multipactor resonance and non-resonance conditions, which are due to (i) the SEY curve going to zero for impact energies less than the 12.5 eV threshold, and (ii) the emission energy being zero when a secondary electron is emitted. As noted previously for the boxcar SEE model, when more physically accurate SEE models are examined in future sections, we will see that these sharp transitions are smoothed out.

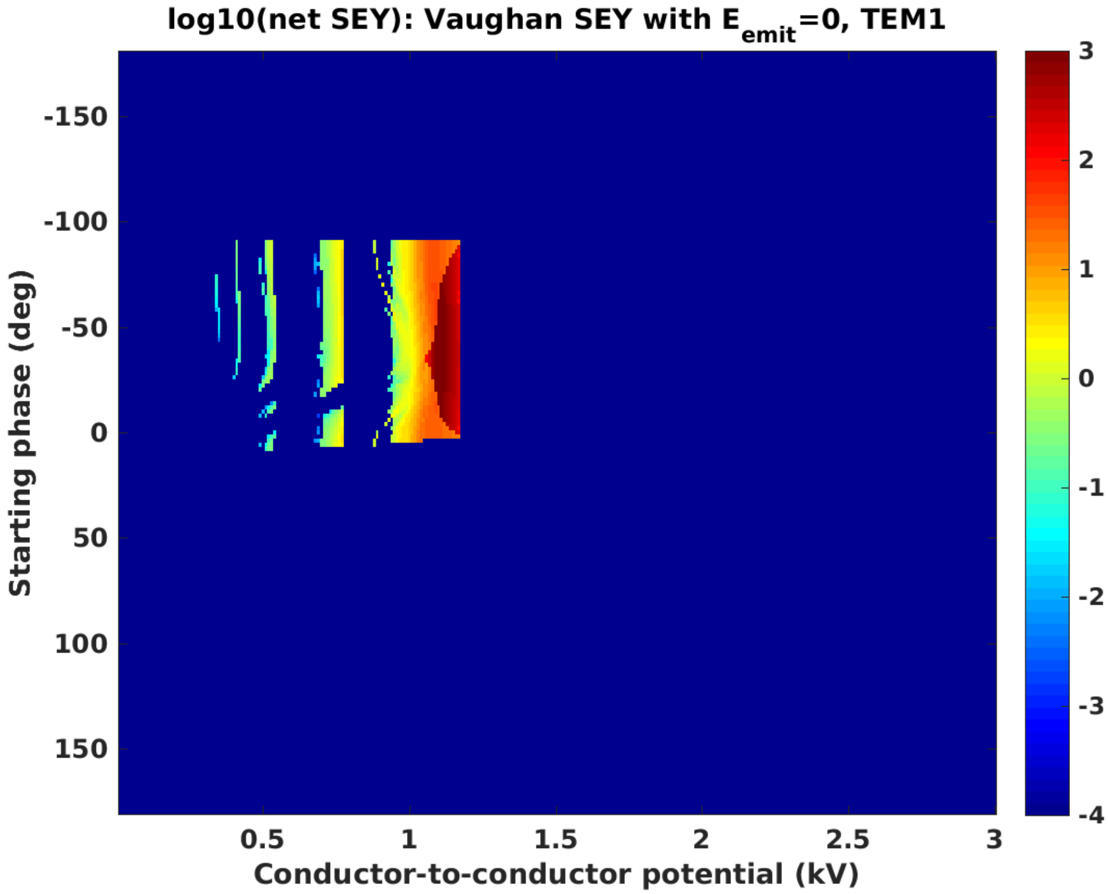

Figure 10: Net SEY surface for Vaughan SEY curve with zero emission energy, in coaxial geometry #1.

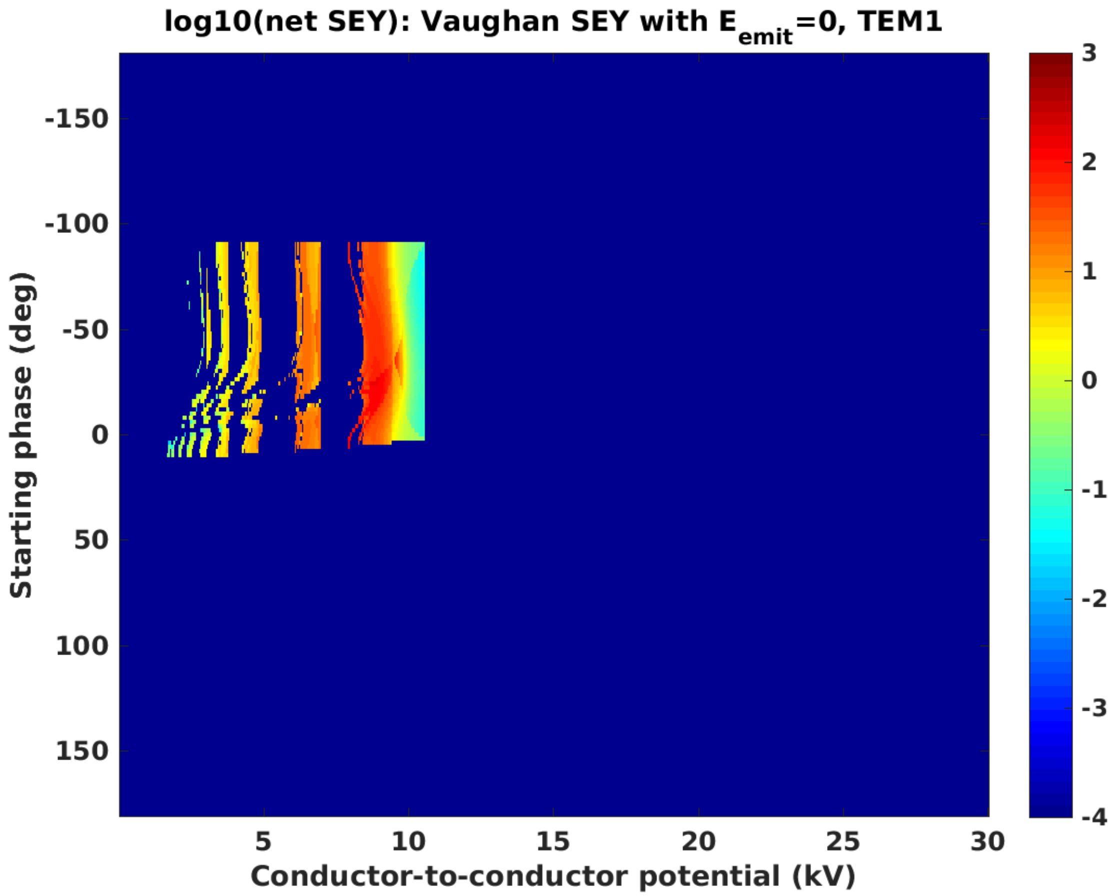

Figure 11: Net SEY surface for Vaughan SEY curve with zero emission energy, in coaxial geometry #2.

3.6 Vaughan model with non-zero emission energy

We next consider Vaughan's SEY curve, but instead of defining the emission energy to be zero as was done in the previous section, we allow the emitted electrons to have a spectrum of energies which follow a random process related to the underlying stochastic quantum mechanics. In this second approach to handling the emission energy spectrum, we considered secondary electrons to be selected randomly from a weighted collection of three underlying distributions: (1) True secondary electrons, which follow a Maxwell-Boltzmann energy distribution with an electron temperature of 5 eV, (2) rediffused electrons, also sometimes called scattered electrons, which follow a uniform energy distribution between the 0 eV and the incidence energy, and (3) reflected electrons, also sometimes called elastically scattered or backscattered electrons, which rebound elastically from the surface with the same energy as the incident energy. The choice of a 5 eV electron temperature for the true secondary electrons is somewhat arbitrary, but was chosen to yield reasonable approximate secondary electron energies for a wide range of incident electron energies ranging from a few eV up to thousands of eV. All of these emission mechanisms were assumed to have an isotropic distribution of emission angles within the half-space of the boundary containing the incident electron. This classification of three scattering mechanisms and the angular distribution was chosen to be analogous to how Furman's model [35] categorizes secondary emission mechanisms as will be described in Section 3.7.

The specific secondary electron distribution used was chosen randomly, with the probability of each scattering mechanism chosen to match the (incident energy dependent) probabilities given by Furman's model, in order to best compare the models. For the copper data used in this present research, at incidence energies near that which maximizes the SEY curve, true secondary electrons contribute about 90% to the SEY, the rediffused electrons contribute about 9% to the SEY, and the reflected electrons contribute about 1% to the SEY.

Since this SEY model incorporates a stochastic emission model, Monte Carlo simulations involving 100 independent trials were undertaken to characterize the resulting multipactor susceptibility. Figures 12 and 13 below respectively show the median results for the multipactor simulations of coaxial geometries #1 and #2, where each pixel represents the median value of 100 trials at a particular choice of (magnitude, phase). In comparison with the previous SEY models which used zero emission energies, we note much larger areas within the electric field's (magnitude, phase) space where multipactor can occur, and we see that the transitions are smoothed out along the field magnitude axis and show more structure overall. This is due to averaging over the stochastic emission energy trials, where non-zero emission energies permit some multipactor trajectories to be possible even if they do not strictly satisfy the resonance conditions that would be required for zero emission energy.

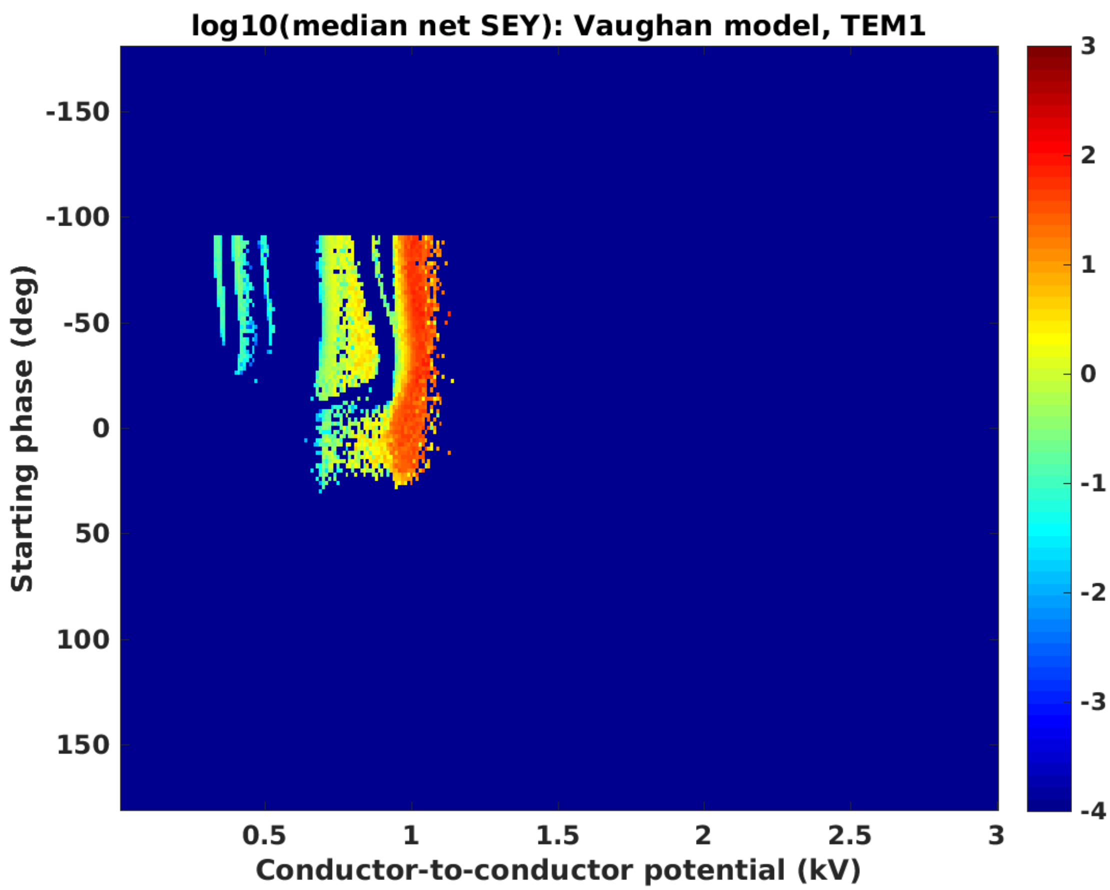

Figure 12: Median net SEY surface for Vaughan SEY curve with nonzero emission energy, in coaxial geometry #1. The median is calculated over 100 Monte Carlo trials.

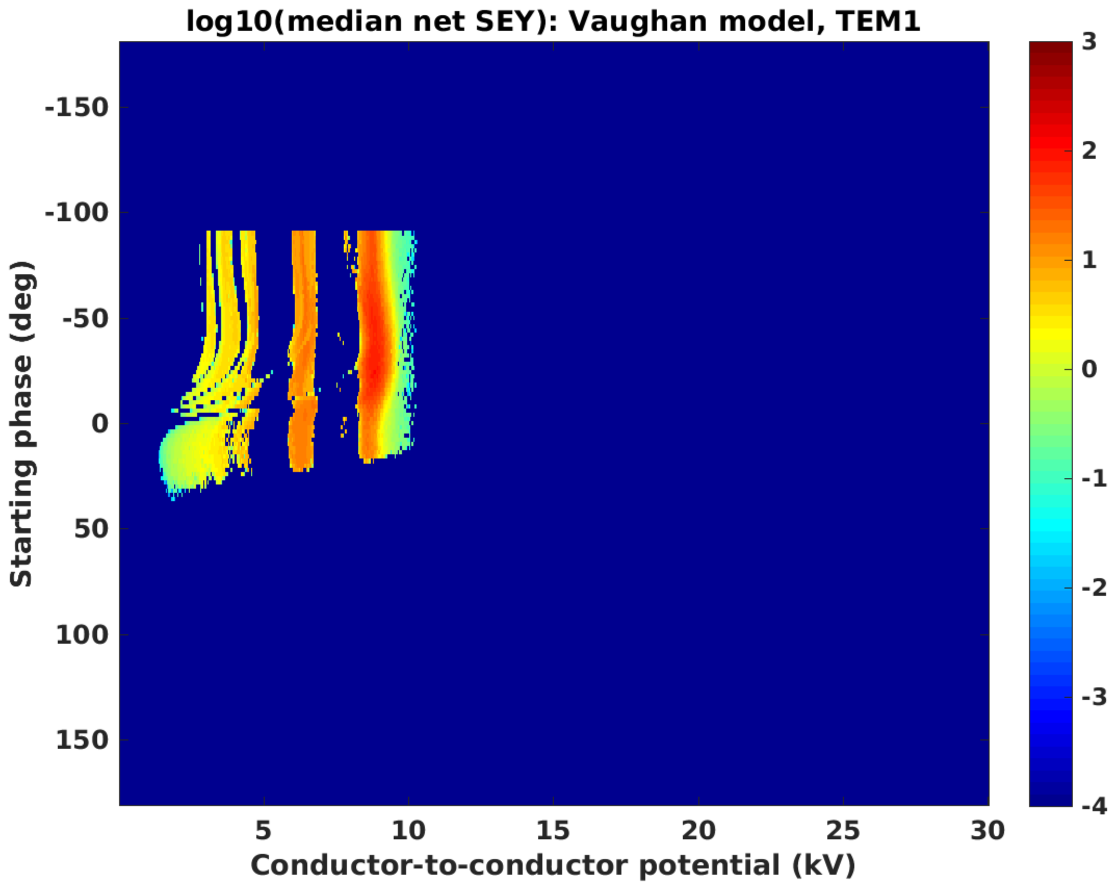

Figure 13: Median net SEY surface for Vaughan SEY curve with nonzero emission energy, in coaxial geometry #2. The median is calculated over 100 Monte Carlo trials.

3.7 Furman model

Furman's SEE model [35] is an even more complex model which has enjoyed popularity within the particle accelerator community. Furman's model contains around 45 parameters, and unlike Vaughan's model, Furman's model also provides the energy and angular distributions for the emitted electrons. Furman's model is based around the three secondary electron distributions that were introduced in the previous section to make Vaughan's model more comparable to Furman's model, namely true secondary, scattered, and reflected electrons, the sum of which provide the total SEY. An important feature of Furman's model is that the SEY does not go to zero as the impact energy goes to zero. Figure 14 shows Vaughan's and Furman's SEY models, as applied to the copper data from Furman's paper.

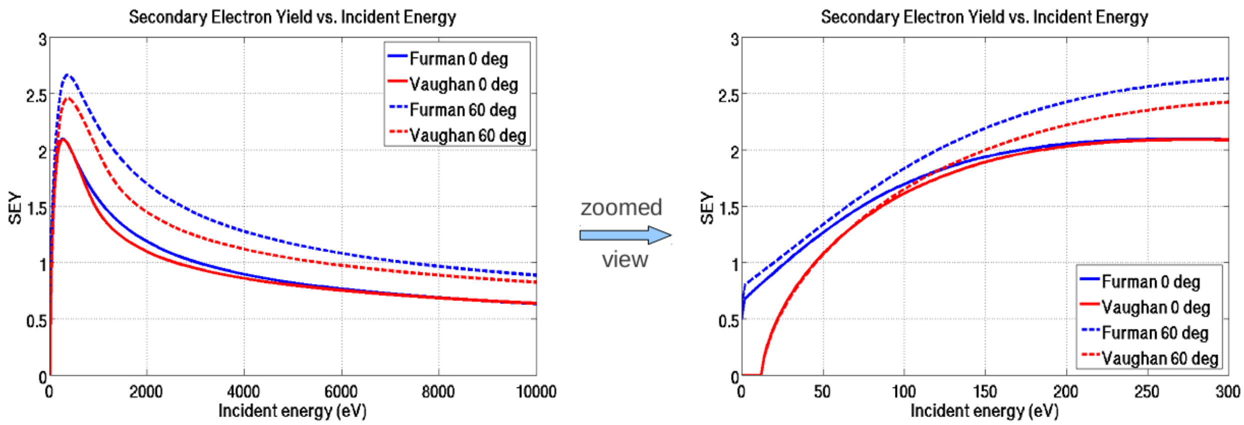

Figure 14: SEY vs. incidence energy curves from the Furman and Vaughan models. Results shown for normal incidence and 60º from normal. The left plot shows the SEY curve over a wide range of incident energies (0 eV to 10 keV), and the right plot shows the curve magnified to show low-energy features (0 eV to 300 eV).

Figures 15 and 16 respectively show the median net SEY when using Furman's model with coaxial geometries #1 and #2, where as before we compute the median of 100 Monte Carlo trials. We immediately note some key differences in the resulting multipactor susceptibility surfaces as compared to Vaughan's model. The first key difference is that Furman's model predicts much larger regions of non-trivial multipactor susceptibility than does Vaughan's model, which is due to Vaughan's model defining the SEY to be zero for incident electrons below a 12.5

eV threshold, effectively discarding multipactor trajectories with any single impact energy below this threshold. The second major difference is that even in regions of field phase that are not conducive to multipactor resonance, such as for starting phases outside of the range of approximately -90º to +90º, we see a non-zero net SEY. This is due to Furman's model having an (incident angle dependent) SEY in the vicinity of 0.6, such that even non-resonant trajectories can still have a non-zero net SEY after a finite simulation time. The zero net SEY at low field strengths for starting phases in the range of approximately -90º to +40º is due to trajectories which drift into the space between the conductors, but do not obtain at least two boundary impacts within the simulation time, resulting in the net SEY being set to zero as explained in Section 3.3. In the next section which introduces the medianized Furman SEE model, some particle trajectory plots are shown in Figures 19 and 20 which demonstrate these features of the net SEY surface as seen with the Furman model.

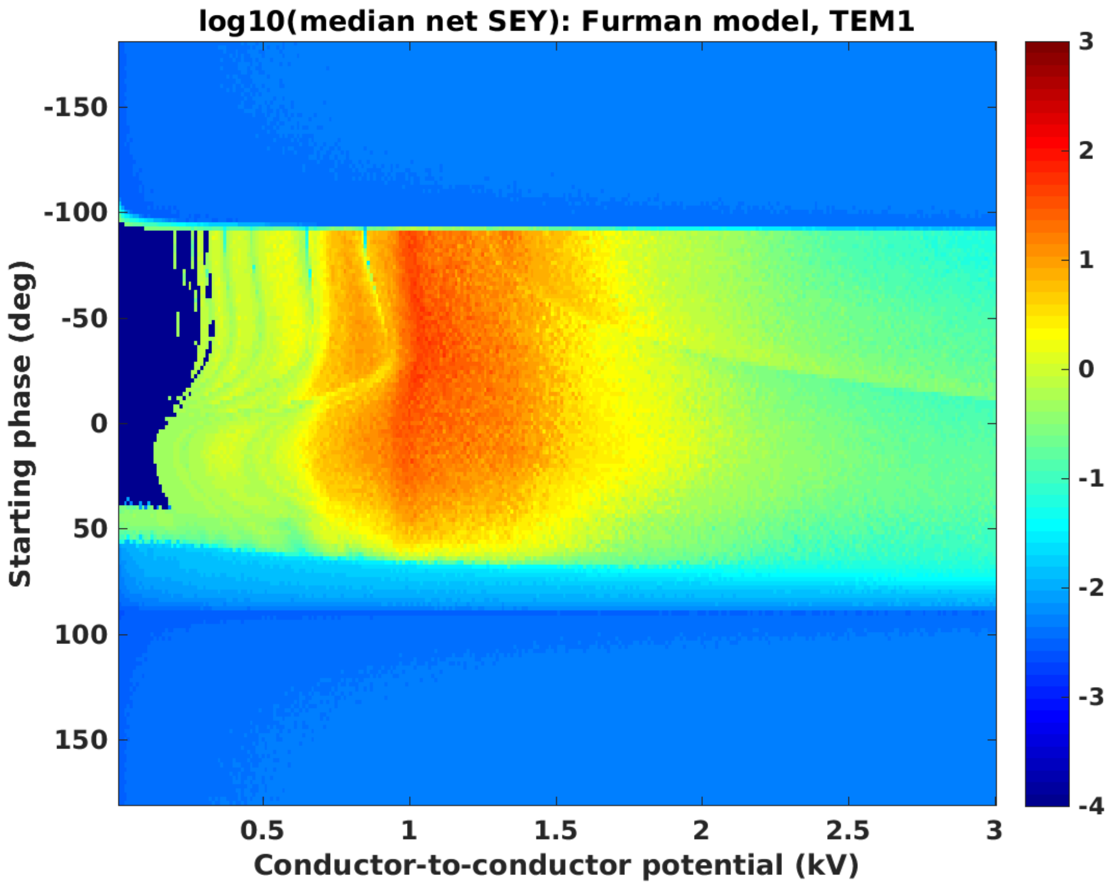

Figure 15: Median net SEY surface for Furman SEE model, in coaxial geometry #1. The median is calculated over 100 Monte Carlo trials.

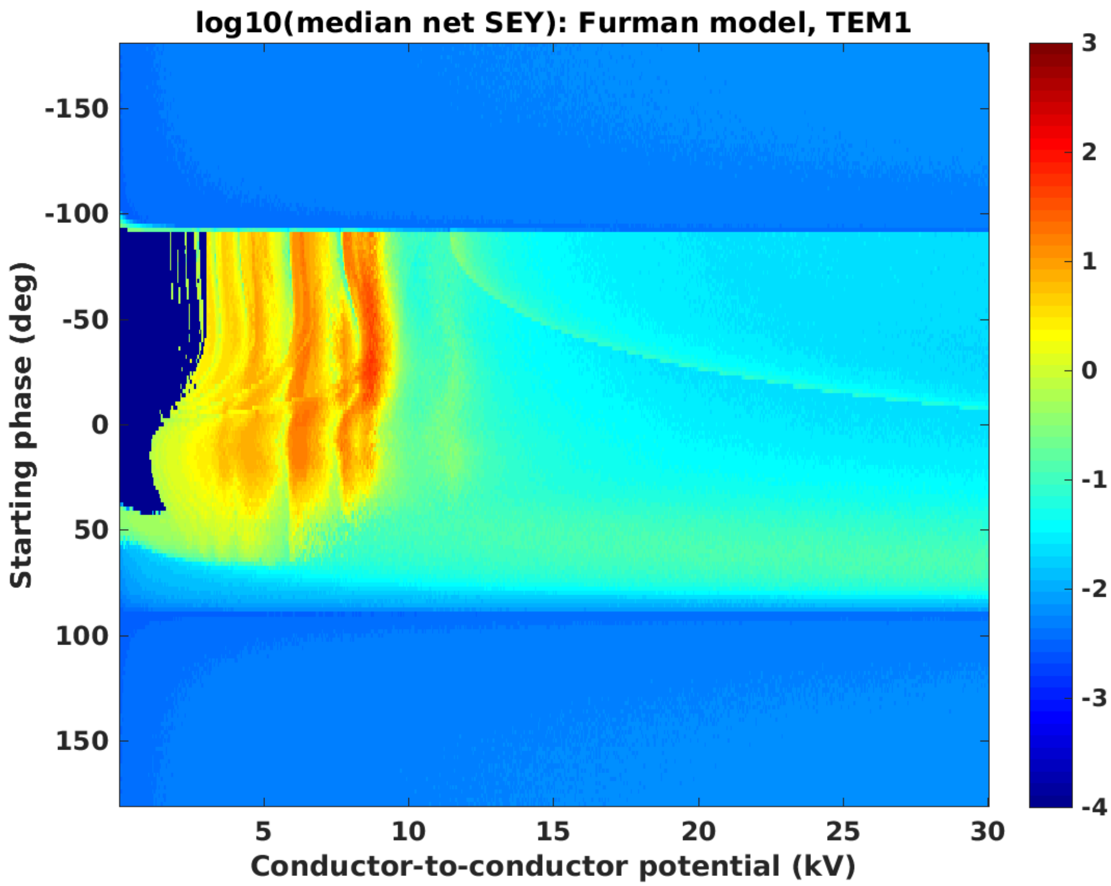

Figure 16: Median net SEY surface for Furman SEE model, in coaxial geometry #2. The median is calculated over 100 Monte Carlo trials.

3.8 Furman model with medianized emission energy

The previous results in this chapter suggest that multipactor formation can be very sensitive to low impact energy electrons, which makes Furman's model particularly appealing. However, Furman's model is a stochastic model which in practice requires Monte Carlo simulations to determine multipactor susceptibility for given geometry and field conditions. Instead of using Furman's complete SEY model, we propose a variant in which the emitted electron energies are defined to be the median of the (incident energy and angle dependent) emission distribution, and the emission direction is defined to be normal to the boundary. By using this approach, we retain the multipactor formation sensitivity to low impact energy electrons, and we are also able to obtain net SEY results, which appear to be qualitatively accurate without resorting to costly Monte Carlo simulations.

Figures 17 and 18 respectively show the net SEY when using Furman's medianized model with coaxial geometries #1 and #2. As compared to the results in the previous section generated using Furman's full model, these results show less smooth transitions in net SEY along the field magnitude axis; this is due to the lack of the stochastic emission energies which previously caused a smoothing effect at multipactor resonance boundaries. However, we observe that the results retain much of the overall structure and predictive value for multipactor, as compared to the full Furman model results of the previous section. The errors between the medianized Furman model and the full Furman model will be further studied and quantified in Chapter 5.

In timing tests done to compare the Furman model and the medianized Furman model, using both interpreted Matlab code and compiled Matlab code, a single execution of Furman's fully stochastic model took approximately twice as long as a single execution of the medianized Furman model. However, the computational savings with the medianized model comes not from the faster execution of the secondary electron scattering code, but rather from only needing to track one particle throughout the entire simulation, instead of tracking numerous particles (possibly growing exponentially in time) using Furman's fully stochastic model. Of course the price to pay for this computational savings is a less faithful simulation of the underlying physics, and therefore increased errors between simulation and reality.

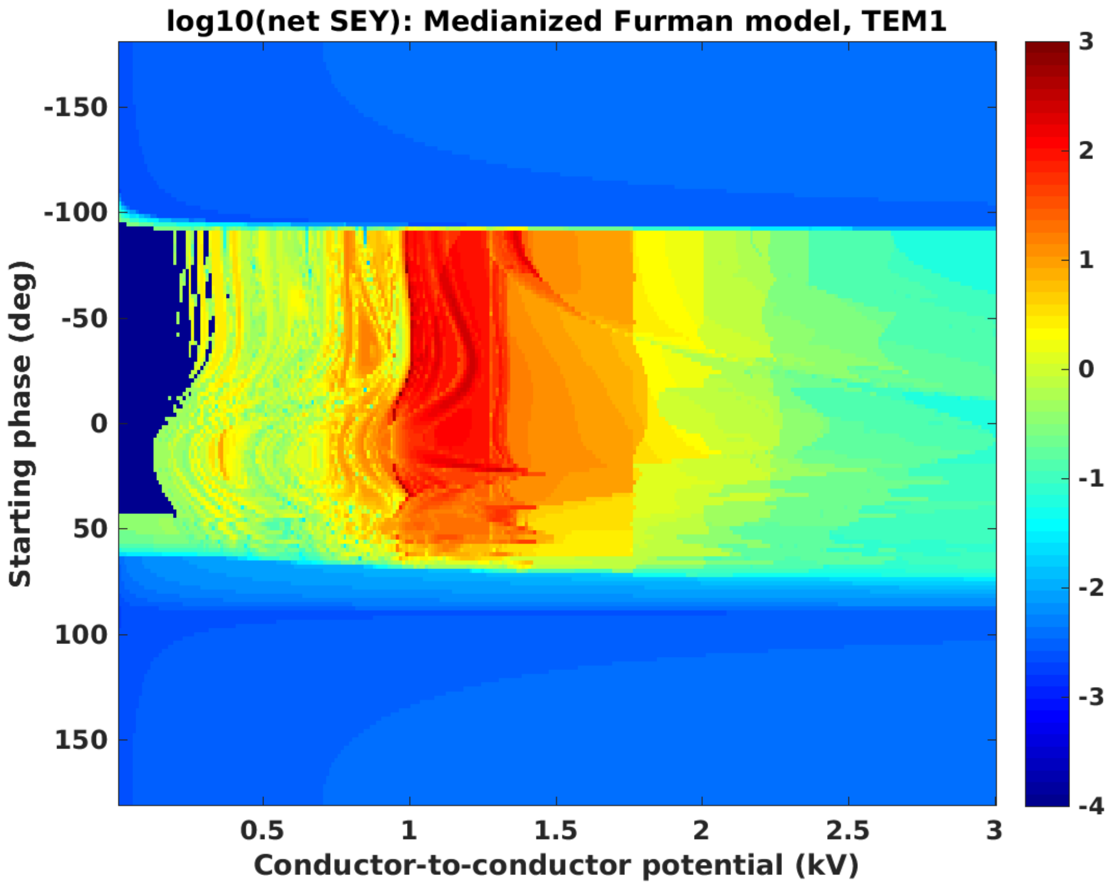

Figure 17: Net SEY surface for medianized Furman SEE model, in coaxial geometry #1.

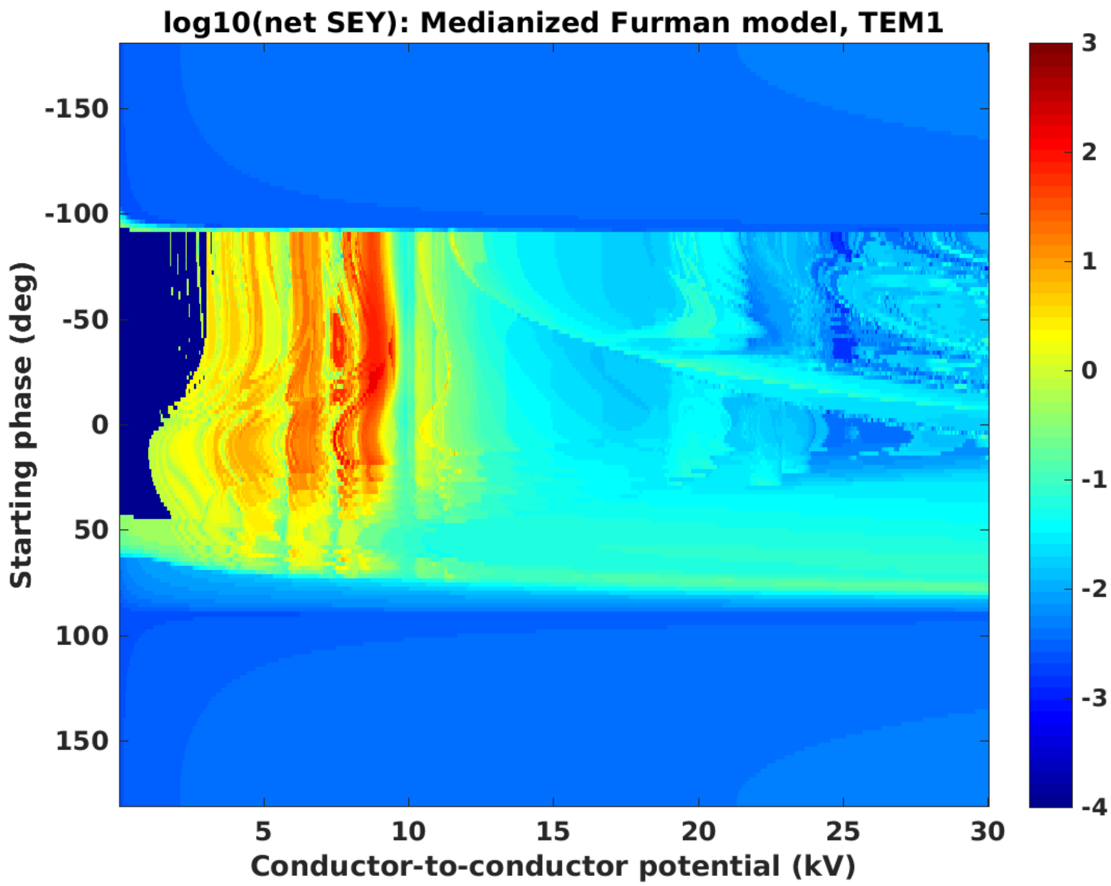

Figure 18: Net SEY surface for medianized Furman SEE model, in coaxial geometry #2.

In the previous section, we noted that with Furman's SEE model we see a region of zero net SEY at low field strength and starting phases in the range of approximately -90º to +40º, and small but nonzero net SEY for starting phases outside of the range of approximately -90º to +90º. The zero net SEY at low field strengths for starting phases in the range of approximately -90º to +40º is due to trajectories which drift into space between the conductors, but do not obtain at least two boundary impacts within the simulation time, as shown by some example particle trajectories in Figure 19. The small but nonzero net SEY for starting phases outside of the range of approximately -90º to +90º is due to Furman's model having an (incident angle dependent) SEY in the vicinity of 0.6, such that even non-resonant trajectories which impact a boundary can still have a vanishing but non-zero net SEY after a finite simulation time. Figure 20 shows examples of such particle trajectories, in which secondary electrons are continually emitted and then quickly return to the surface which emitted them.

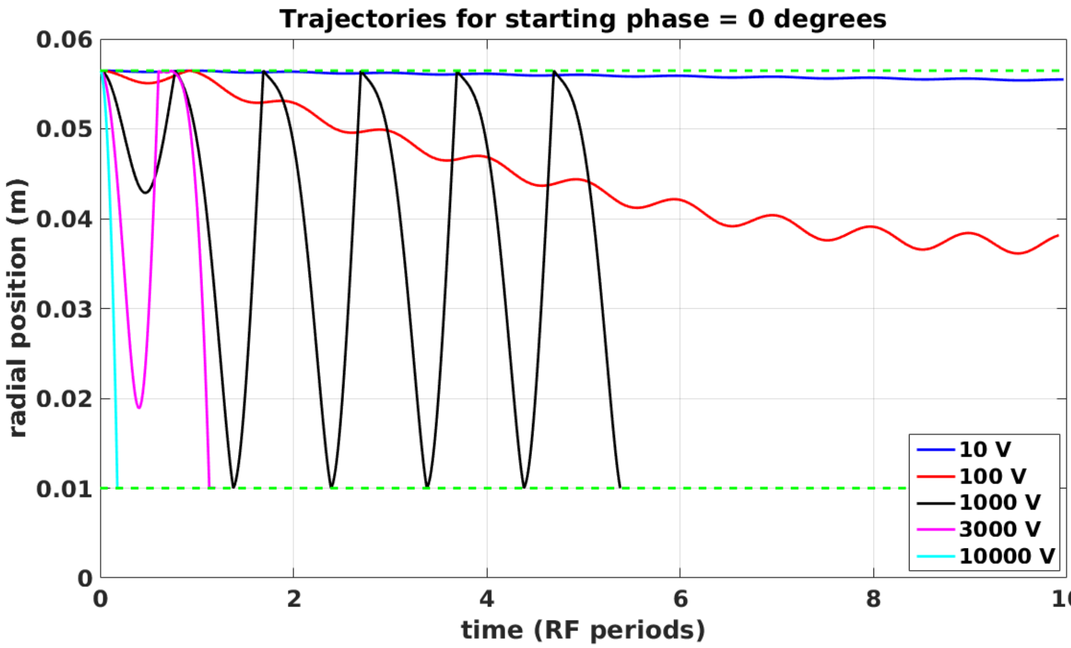

Figure 19: Radial position of particle trajectories in cavity #1, plot #1. Radial position of particle trajectories in cavity #1 for the medianized Furman SEE model, for varying peak gap voltages, and a starting field phase of 0º. Radial boundaries of the gap are shown as the dashed green line. At voltages of 10 V and 100 V, the trajectories are seen to drift into the gap without obtaining at least two boundary impacts, so their net SEY is defined to be zero. At a voltage of 100 V, we see a clear phase-locking of the particle trajectory to the driving field. At voltages of 3,000 V and 10,000 V, we see the particle driven to the opposing boundary, where it repeatedly is driven into that boundary until the simulation terminates after (# strikes)+(# RF periods)=10.

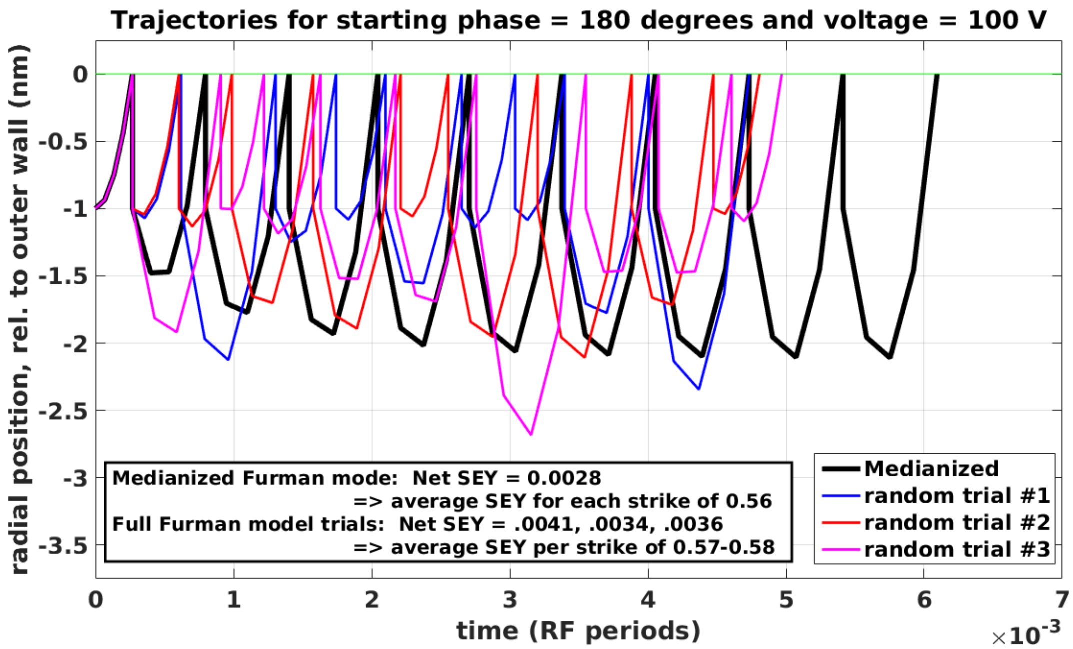

Figure 20: Radial position of particle trajectories in cavity #1, plot #2. Radial position of particle trajectories in cavity #1 for the medianized Furman SEE model, and three trials of the stochastic Furman SEE model, for a peak gap voltage of 100 V, and a starting field phase of 180º. The outer radial boundary of the gap is shown as the dashed green line. For each simulation, the particle is repeatedly driven into the outer radial boundary until the simulation terminates after 10 boundary impacts. The net SEY for the medianized Furman model is 0.0028 (geometric average SEY of 0.56 per impact), and the net SEY for the three stochastic Furman model trials is 0.0041, 0.0034, and 0.0036 (geometric average SEY of 0.57 or 0.58 per impact); these nonzero net SEY values appear as small values on the net SEY surface plots which are plotted on a logarithmic scale.

3.9 Multipactor growth rates

Throughout this dissertation, we typically focus on the net SEY when comparing different approaches to simulating the initiation of multipactor. In Section 3.3, it was noted that the net SEY is different from the growth rate of the multipactor current, because the net SEY does not take into account the length of time over which a multipactor trajectory is simulated before termination. In this section we relate the growth rate of multipactor current and the net SEY.

In the early-time evolution of multipactor when space charge effects are negligible, we can approximate the multipactor current as growing exponentially: $I(t) = I_0 e^{kt}$, where $I(t)$ is the total multipactor current, I_0 is the initial current, e is the base of the natural logarithm, k is the growth rate, and t is time. k is understood to be negative for an exponential decay of multipactor current. Within this framework, the net SEY at any instant in time is given by $I(t)/I_0$, and thus by taking the natural logarithm of the net SEY, we can calculate the product kt of the growth rate and time. In order to then determine k, we use the time $t = t_{final\ strike}$ of the final impact within a simulated trajectory. We thus have:

$$k = \log(\text{net SEY}) \,/\, t_{\text{final strike}}\ . \tag{3.2}$$

The growth rates for coaxial cavity #1 are shown in Figures 21 through 23, and in Figures 24 through 26 for coaxial cavity #2. Within each series of plots we respectively show the median growth rates as computed from 100 Monte Carlo trials of Vaughan's model with stochastic emission, the median growth as computed from 100 Monte Carlo trials of Furman's model, and the median growth as computed from the medianized Furman model.

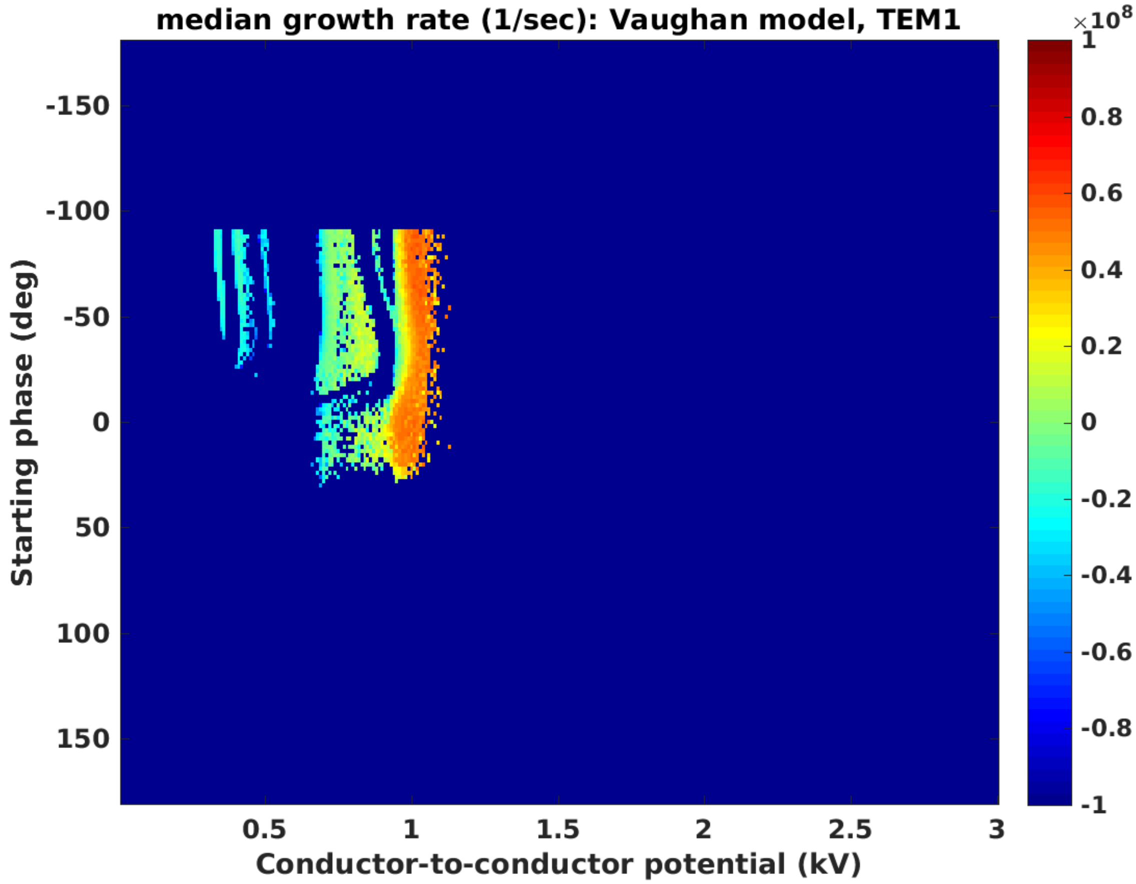

Figure 21: Median growth rate for Vaughan SEE model with stochastic emission energy, in coaxial geometry #1. The median is calculated over 100 Monte Carlo trials.

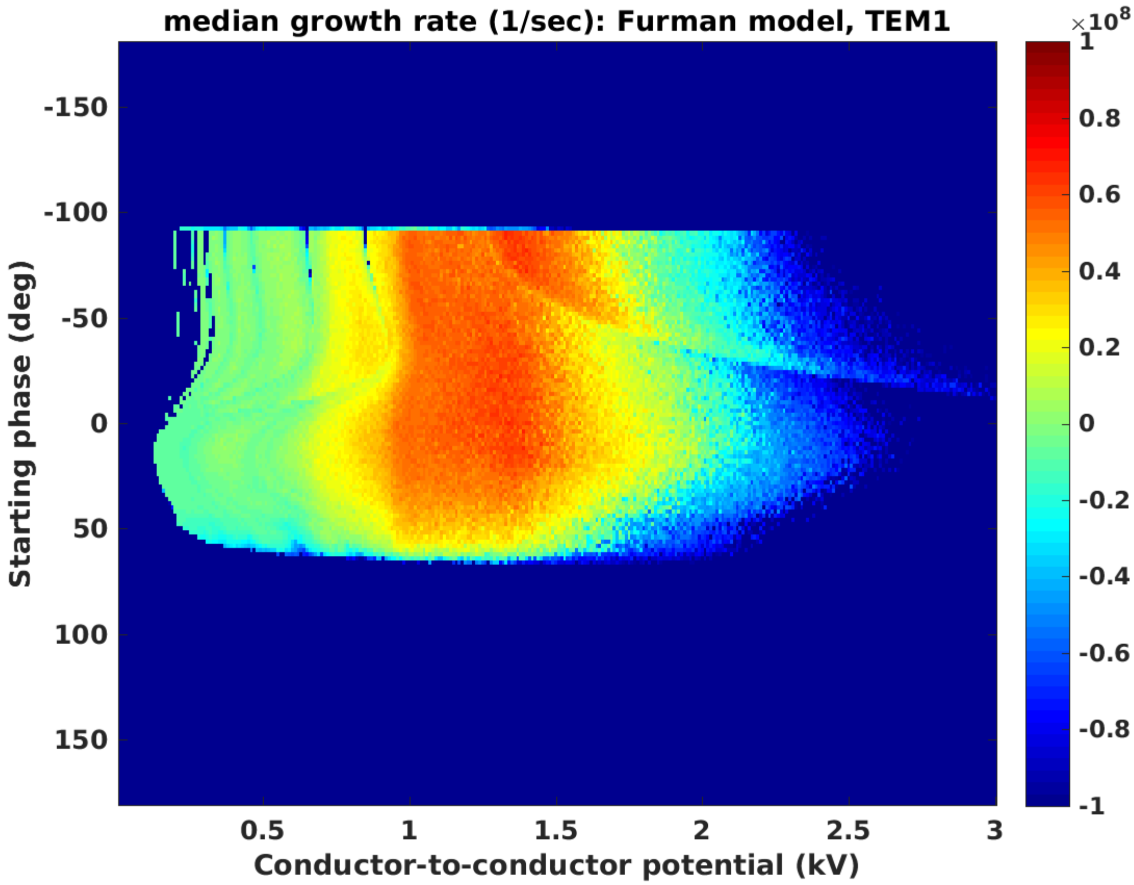

Figure 22: Median growth rate for Furman SEE model, in coaxial geometry #1. The median is calculated over 100 Monte Carlo trials.

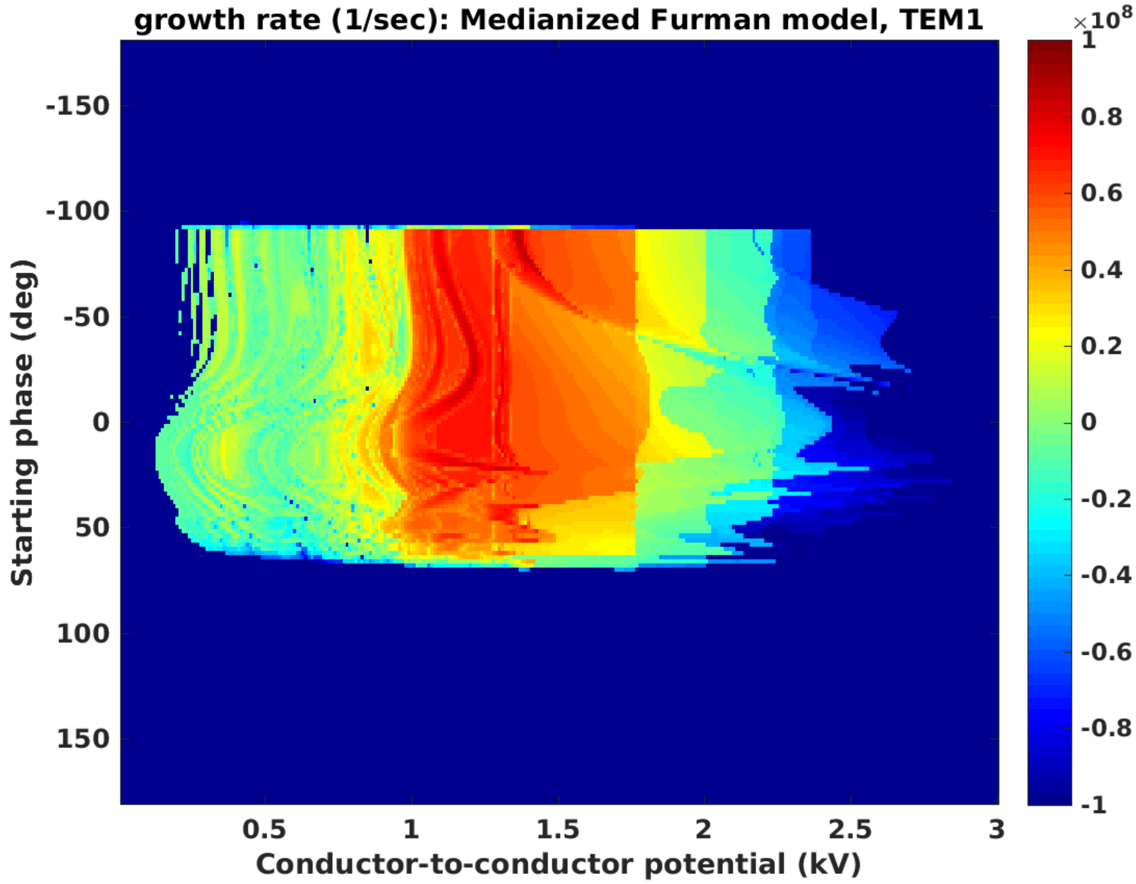

Figure 23: Growth rate for Medianized Furman SEE model, in coaxial geometry #1.

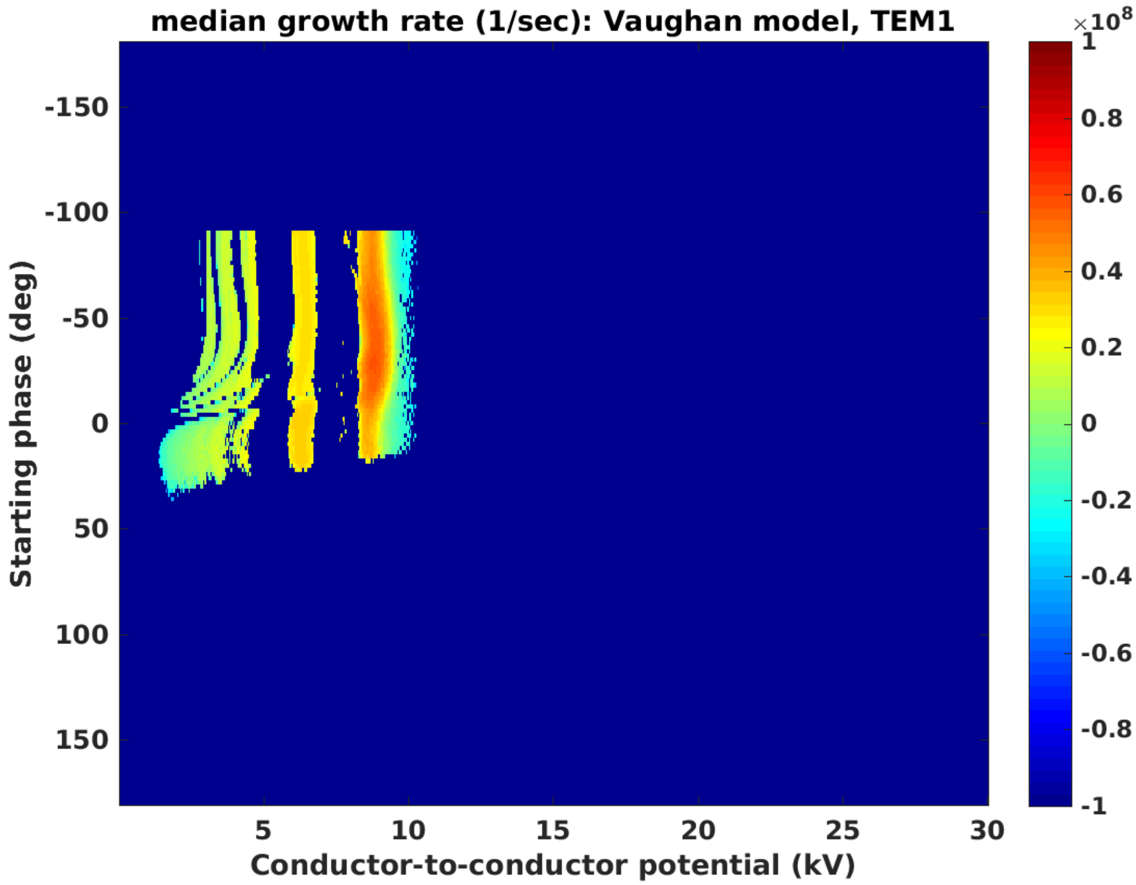

Figure 24: Median growth rate for Vaughan SEE model with stochastic emission energy, in coaxial geometry #2. The median is calculated over 100 Monte Carlo trials.

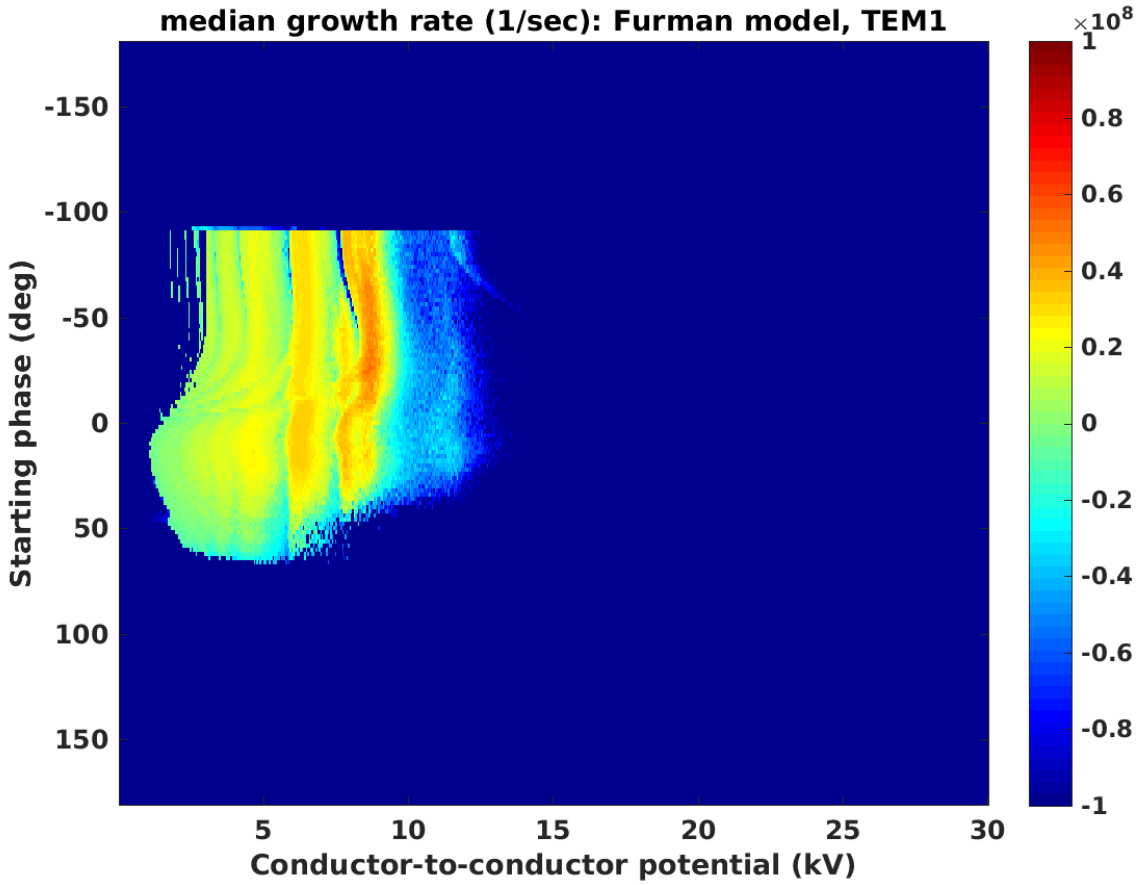

Figure 25: Median growth rate for Furman SEE model, in coaxial geometry #2. The median is calculated over 100 Monte Carlo trials.

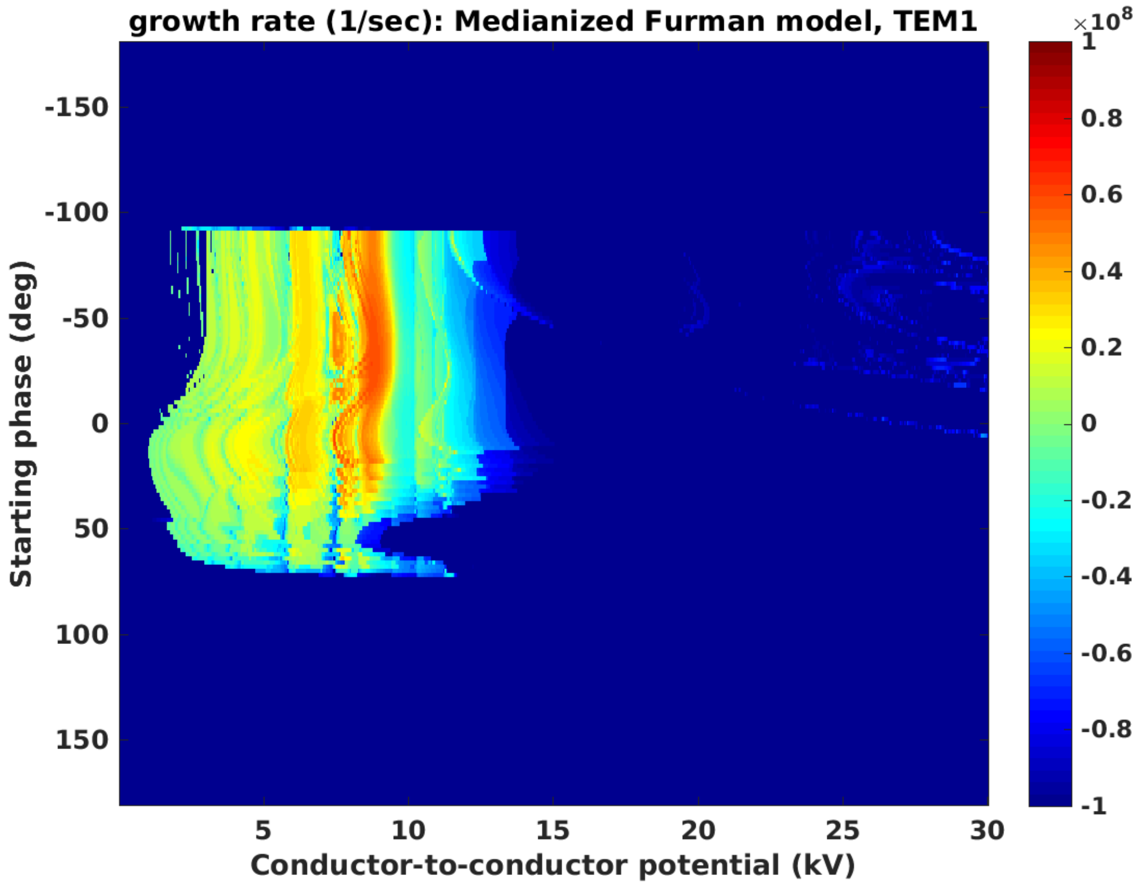

Figure 26: Growth rate for Medianized Furman SEE model, in coaxial geometry #2.

When we compare the Vaughan, Furman, and medianized Furman SEE models, we see similar behavior with the growth rate surfaces as we did with the the previous net SEY surfaces. Specifically, the Vaughan model significantly under-estimates the growth rate as compared to the Furman model, due to the fact that the Vaughan model will discard trajectories will a low impact energy for one or more boundary strikes, even if successive boundary strikes are capable of contributing significant growth. Also as before, the medianized Furman model can yield a respectable estimate of the stochastic Furman model; some errors are evident, but the computational costs is much less because Monte Carlo trials are avoided.

3.10 Conclusions

For all of the multipactor results of this chapter, regardless of the SEE model used, regions of multipactor resonances are apparent in the surface plots over the (voltage, starting phase) spaces examined. No known analytical expression for a multipactor resonance condition is available for a coaxial geometry, but the observed behavior of multipactor resonances is qualitatively similar to the discrete multipactor resonance conditions in a parallel plate geometry, as expressed in equation (2.2) in Chapter 2.

These results demonstrate the extreme sensitivity of simulated multipactor upon the low-impact energy SEY and the secondary emission energies. In Chapter 4 we will investigate multipactor suppression via secondary cavity modes [43]. The results of this chapter show that it is essential to take into account non-zero secondary emission energy distributions, and also be mindful of the extreme sensitivity of multipactor on the low-incident energy SEY. It is worthwhile to note that others working to simulate electron cloud effects have also reported on the importance of SEY at low incidence energies [44].

The results of this chapter also show that reasonable multipactor predictions can be accomplished through the use of a medianized version of the fully stochastic Furman SEE model, which saves computational cost relative to Monte Carlo simulations. This approach will be further examined in Chapter 4 by examining different excitation fields, and in Chapter 5 by examining different cumulative statistics besides the median statistic.

CHAPTER 4: Multipactor in the presence of perturbing modes

4.1 Introduction

Because the SEY is dependent upon the impact energy and angle of electrons striking a barrier, it seems reasonable to expect that multipactor will be affected by the introduction of perturbing modes into a resonant structure, in which these additional modes cause the electron impact energies and angles to either increase or decrease away from the peak in the SEY curve. One question of practical interest is whether or not additional modes could be used to suppress multipactor, which is often (but not always) an undesired effect in a resonant system. If the SEY is less than unity when averaged over the entire ensemble of multipacting electrons, then the multipactor will decay with time and not be sustainable.

It is worthwhile to note that resonant modes can be excited independently in most typical resonant structures, and therefore a distinct multipactor-suppressing mode could be introduced and removed as needed without affecting the primary mode excitation. Since multipactor can only occur at certain field strengths because of resonance and SEY considerations, it is also conceivable that multipactor-suppressing modes would only need to be present while a system's primary mode excitation passes through multipactor-susceptible field strength regions.

As in the previous chapter, we use the notional coaxial geometries #1 and #2 as canonical geometries to study multipactor.

4.2 Multipactor suppression with a 3rd harmonic mode

In order to most significantly affect multipactor, we need perturbing modes with periods that are relatively close to the fundamental mode's frequency, otherwise the perturbing mode will simply introduce oscillations around the unperturbed multipactor trajectories, but the overall trajectories of the particles will still be qualitatively similar to those that occur with only the fundamental mode. At the center of the coaxial cavity halfway between the end caps, the fundamental mode electric field is maximized, and even-order TEM harmonic modes have a null at this location, resulting in little to no impact on multipactor trajectories. Let us thus consider the lowest odd-order TEM harmonic, which is the 3rd harmonic.

By an examination of relative phases of the 3rd harmonic to the fundamental mode, it was empirically noted that significant multipactor perturbations were achieved when the modes were exactly out-of-phase, and the 3rd harmonic had an amplitude 3x as great as the fundamental mode. Expressed mathematically, we have the following electric field $\boldsymbol{E}(r,z,t)$ and magnetic field $\boldsymbol{B}(r,z,t)$:

$$\boldsymbol{E}=\hat{r}\frac{V_0}{r\cdot\log(b/a)}\cdot\left(\cos(\omega t+\theta)\cdot\sin\left(\frac{\pi z}{L}\right)-3\cos(3\omega t+3\theta)\cdot\sin\left(\frac{3\pi z}{L}\right)\right), \tag{4.1}$$

$$\boldsymbol{B}=-\hat{\phi}\frac{1}{c}\frac{V_0}{r\cdot\log(b/a)}\cdot\left(\sin(\omega t+\theta)\cdot\cos\left(\frac{\pi z}{L}\right)-3\sin(3\omega t+3\theta)\cdot\cos\left(\frac{3\pi z}{L}\right)\right), \tag{4.2}$$

where all the parameters are as defined in Chapter 3; specifically a cylindrical coordinate system (r,ϕ,z) is assumed for radial position r (meters), azimuthal position ϕ (radians), and axial position z (meters), V_0 denotes a field scaling parameter (Volts), t denotes time (seconds), ω represents the radian frequency (radians/second), θ represents the field temporal phase (radians), L represents the cavity length along the axial direction (meters) such that $0 \leq z \leq L$, a and b respectively denote the inner and outer conductor radii (meters), c is the speed of light in free space (meters/second), carats (^) over a coordinate denote unit vectors in this cylindrical basis, and boldface quantities denote vectors.

We examine the results for each of the five different SEE models that were introduced in the previous chapter: boxcar model with zero emission energy, Vaughan's SEY curve with zero emission energy, Vaughan's SEY curve with stochastic emission energy, Furman's SEE model, and the medianized Furman SEE model. For the results in this section, we use the same parameter sampling as was done in the previous chapter: with cavity #1 we allow V_0 to vary from 10 V to 3000 V in steps of 10 V; with cavity #2 we allow V_0 to vary from 50 V to 30000 V in steps of 50 V. For both of the cavity results in this chapter, we allow θ to range from -π/2 to π/2 in 181 steps.

Figures 27 and 28 respectively show the multipactor susceptibility results for coaxial geometry #1 and coaxial geometry #2, when the boxcar SEY model is employed; since the boxcar SEY can only have values of 0 or 1, the net SEY can only yield values of 0 or 1. These results show that the phase space area where multipactor resonances can occur is much less than for the baseline case examined in the previous chapter. Figures 29 and Figure 30 show the same respective net SEY results for Vaughan's SEY curve with zero emission energy, and we again see the phase space area where multipactor resonances can occur is much less than for the baseline case examined in the previous chapter.

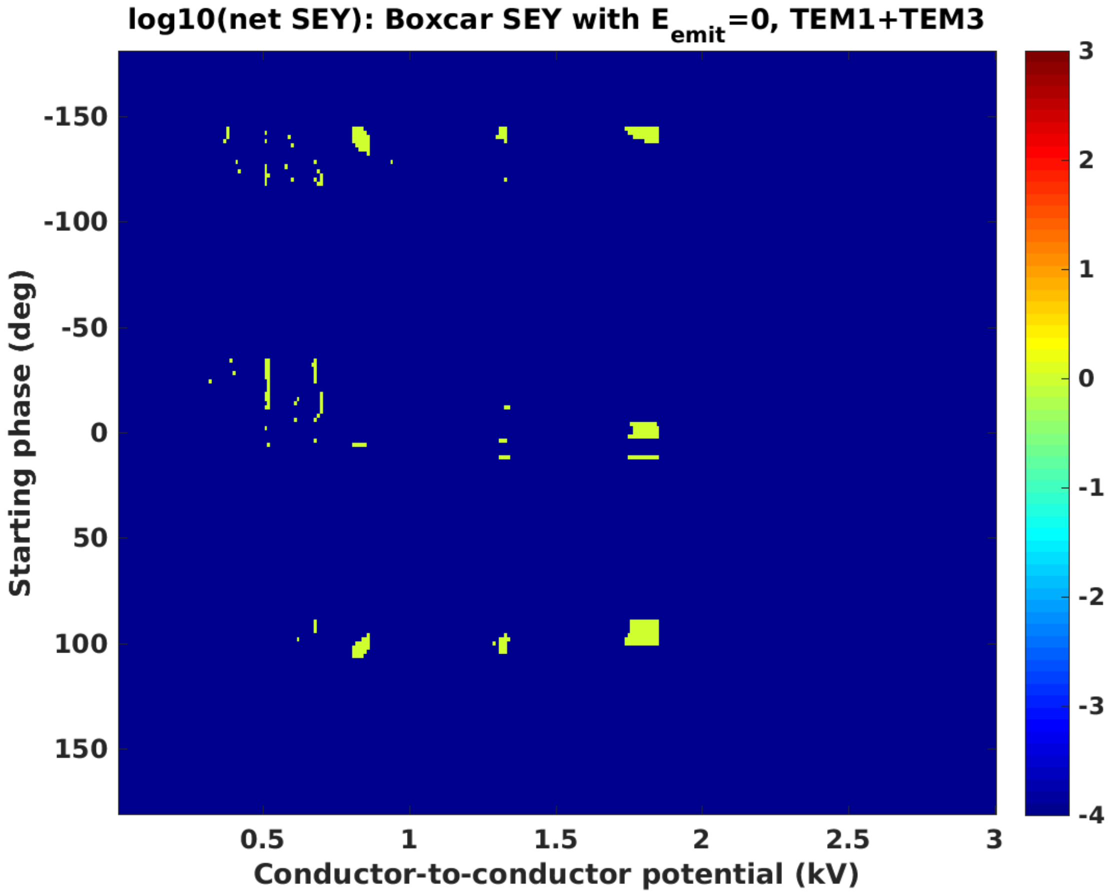

Figure 27: Net SEY in coaxial geometry #1 using the boxcar SEE model, with both the fundamental and 3rd harmonic TEM modes present. Conductor-to-conductor potential corresponds to field strength of the fundamental mode.

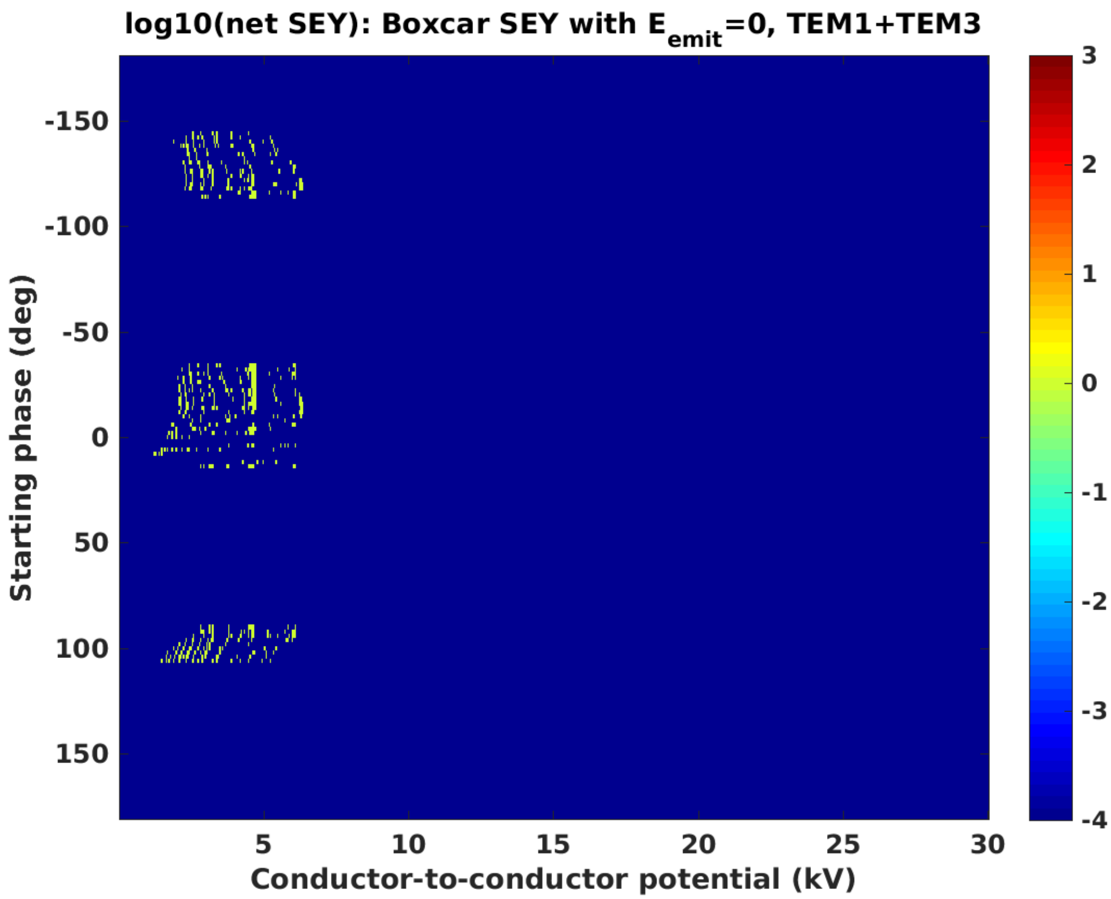

Figure 28: Net SEY in coaxial geometry #2 using the boxcar SEE model, with both the fundamental and 3rd harmonic TEM modes present. Conductor-to-conductor potential corresponds to field strength of the fundamental mode.

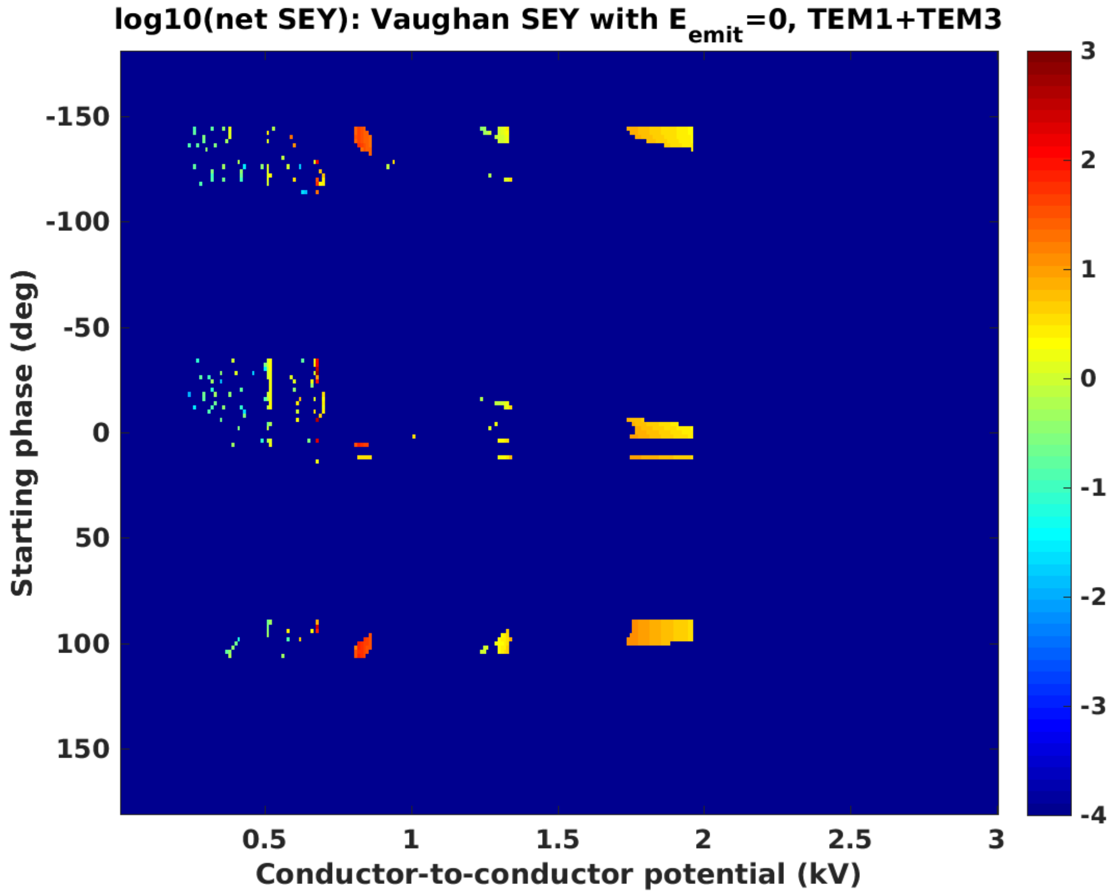

Figure 29: Net SEY in coaxial geometry #1 using Vaughan's SEY curve with zero emission energy, with both the fundamental and 3rd harmonic TEM modes present.

Conductor-to-conductor potential corresponds to field strength of the fundamental mode.

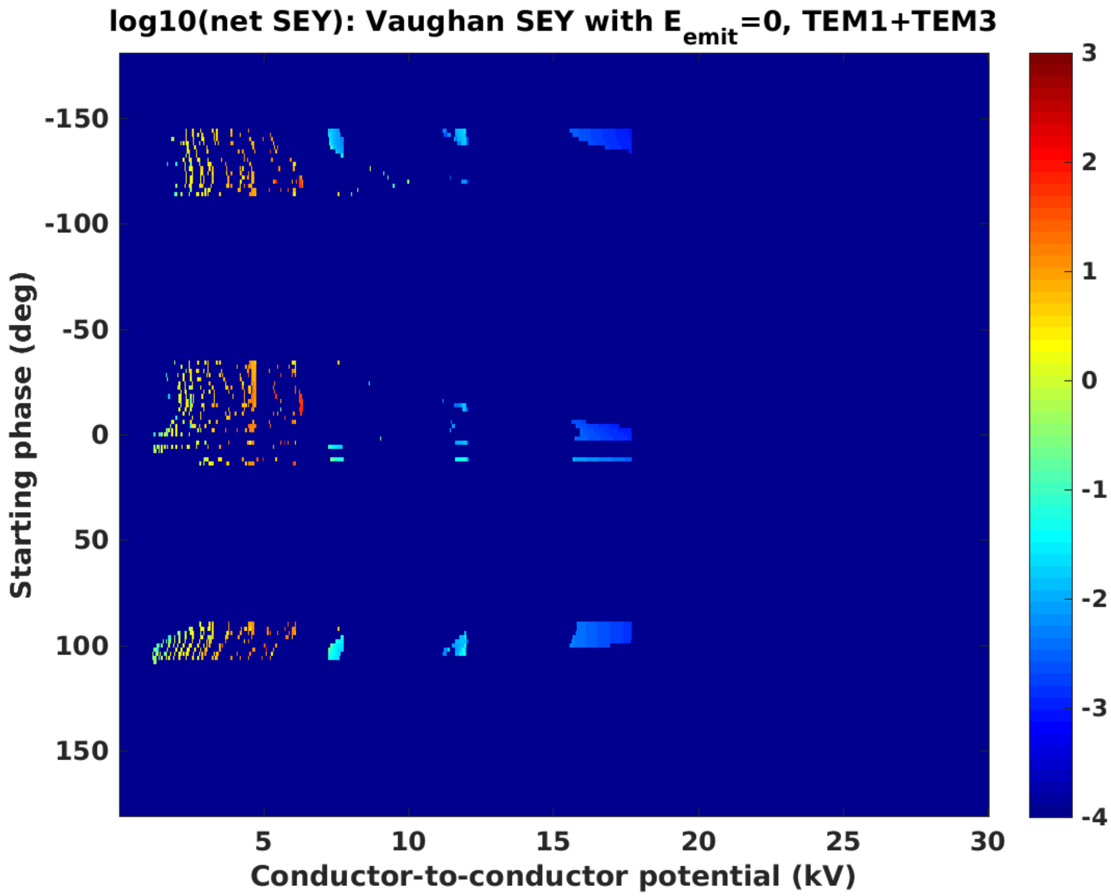

Figure 30: Net SEY in coaxial geometry #2 using Vaughan's SEY curve with zero emission energy, with both the fundamental and 3rd harmonic TEM modes present.

Conductor-to-conductor potential corresponds to field strength of the fundamental mode.

Despite the results for simple SEE models appearing promising in terms of the possibility to suppress multipactor with the 3rd harmonic mode, the more complex SEE models present more humble results. Figures 31 and 32 respectively show the net SEY results for coaxial geometry #1 and coaxial geometry #2, when Vaughan's SEY curve with nonzero emission energy is used. Despite the locations of multipactor susceptibility being displaced in the field (magnitude, phase) space as compared to the baseline case, the total area of multipactor susceptibility is approximately the same as for the baseline case.

Figures 33 and 34 respectively show the net SEY results for coaxial geometry #1 and coaxial geometry #2, when Furman's SEE model is used. As with the Vaughan SEY curve with nonzero emission energy, these results show the locations of multipactor susceptibility being displaced, but no significant reduction in multipactor susceptibility as judged by the total area where multipactor resonances can occur. The medianized Furman model results for coaxial geometries #1 and #2 are respectively shown in figure 35 and 36, and agree fairly well with the full Furman model, demonstrating the utility of the medianized Furman model for obtaining rapid results in lieu of numerous Monte Carlo trials as was done with the full Furman model.

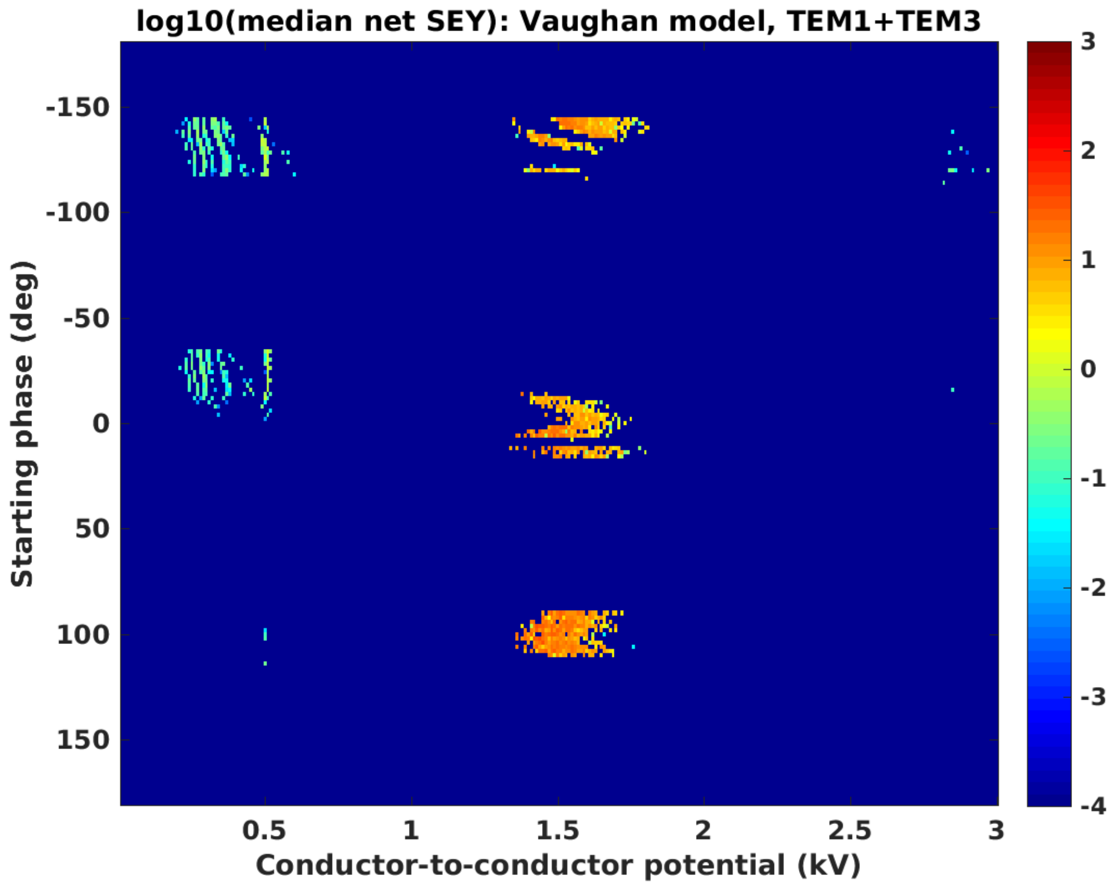

Figure 31: Median net SEY in coaxial geometry #1 using Vaughan's SEY curve with nonzero emission energy, with both the fundamental and 3rd harmonic TEM mode present. Conductor-to-conductor potential corresponds to field strength of the fundamental mode. The median is calculated over 100 Monte Carlo trials.

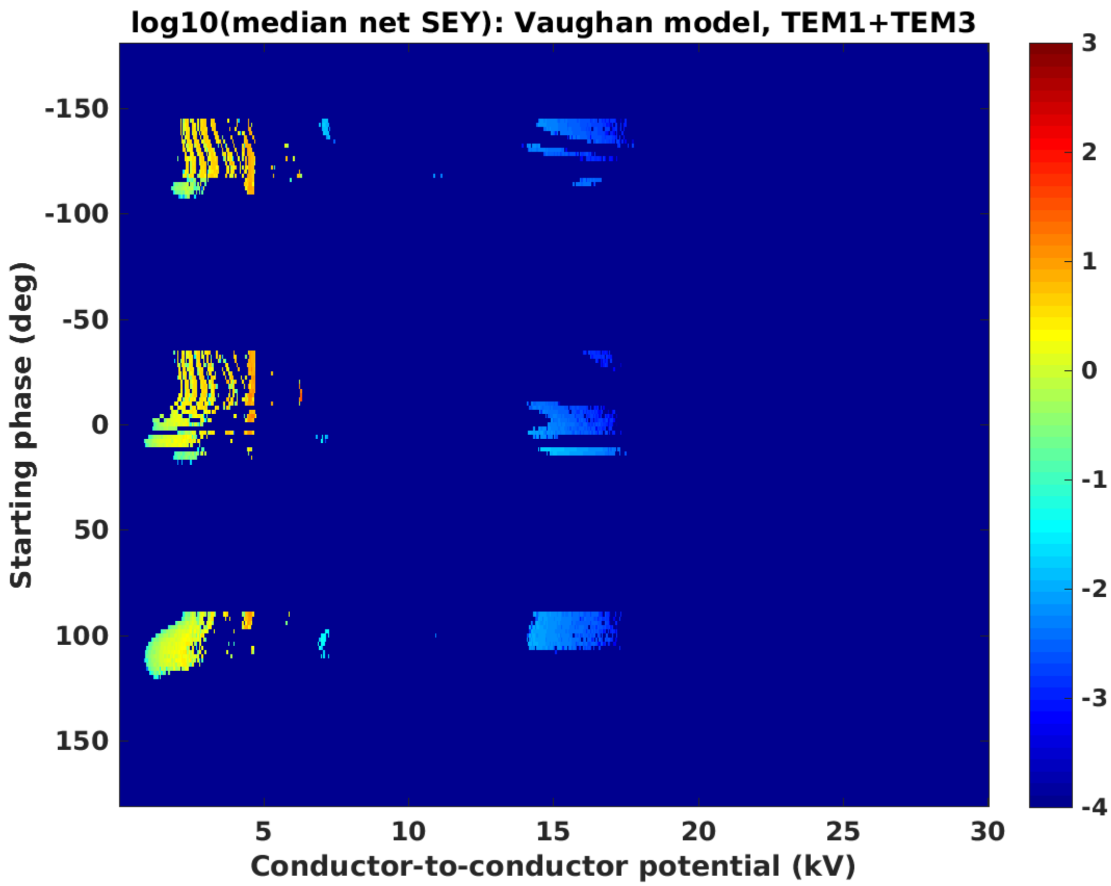

Figure 32: Median net SEY in coaxial geometry #2 using Vaughan's SEY curve with nonzero emission energy, with both the fundamental and 3rd harmonic TEM modes present. Conductor-to-conductor potential corresponds to field strength of the fundamental mode. The median is calculated over 100 Monte Carlo trials.

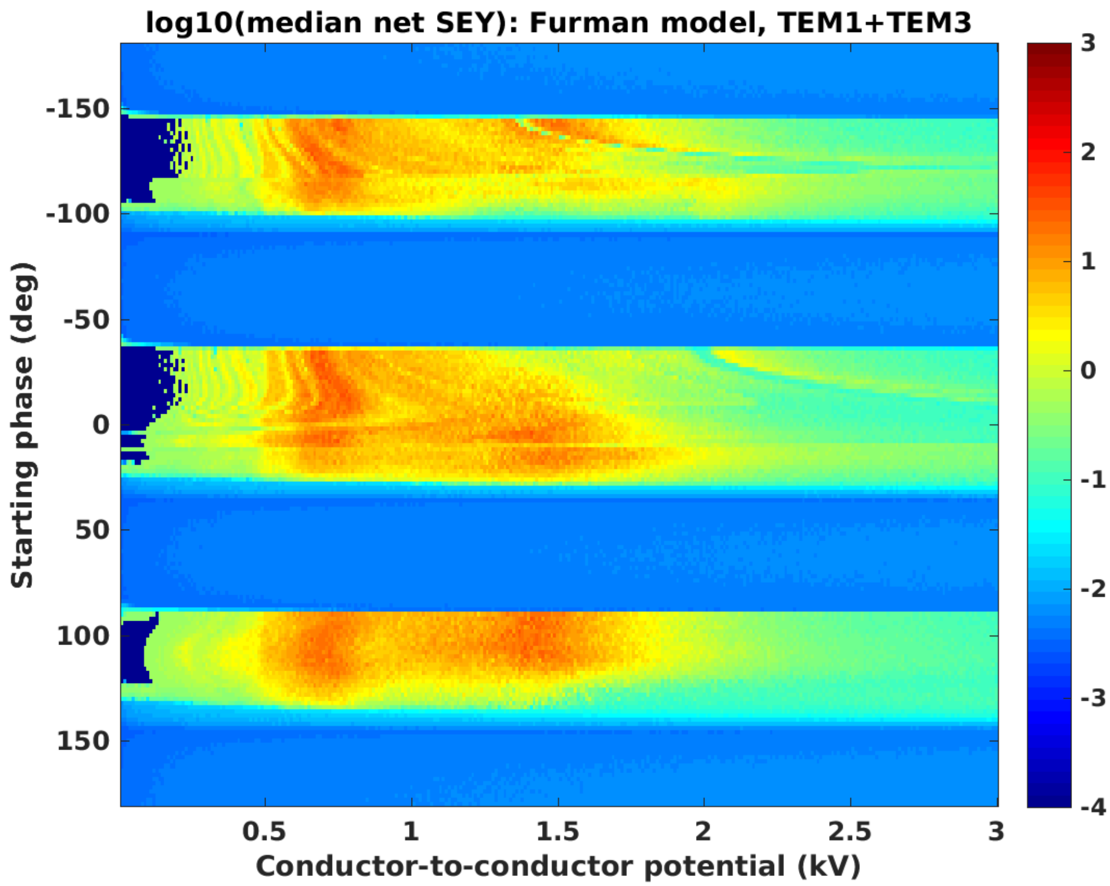

Figure 33: Median net SEY in coaxial geometry #1 using Furman's SEE model, with both the fundamental and 3rd harmonic TEM modes present. Conductor-to-conductor potential corresponds to field strength of the fundamental mode. The median is calculated over 100 Monte Carlo trials.

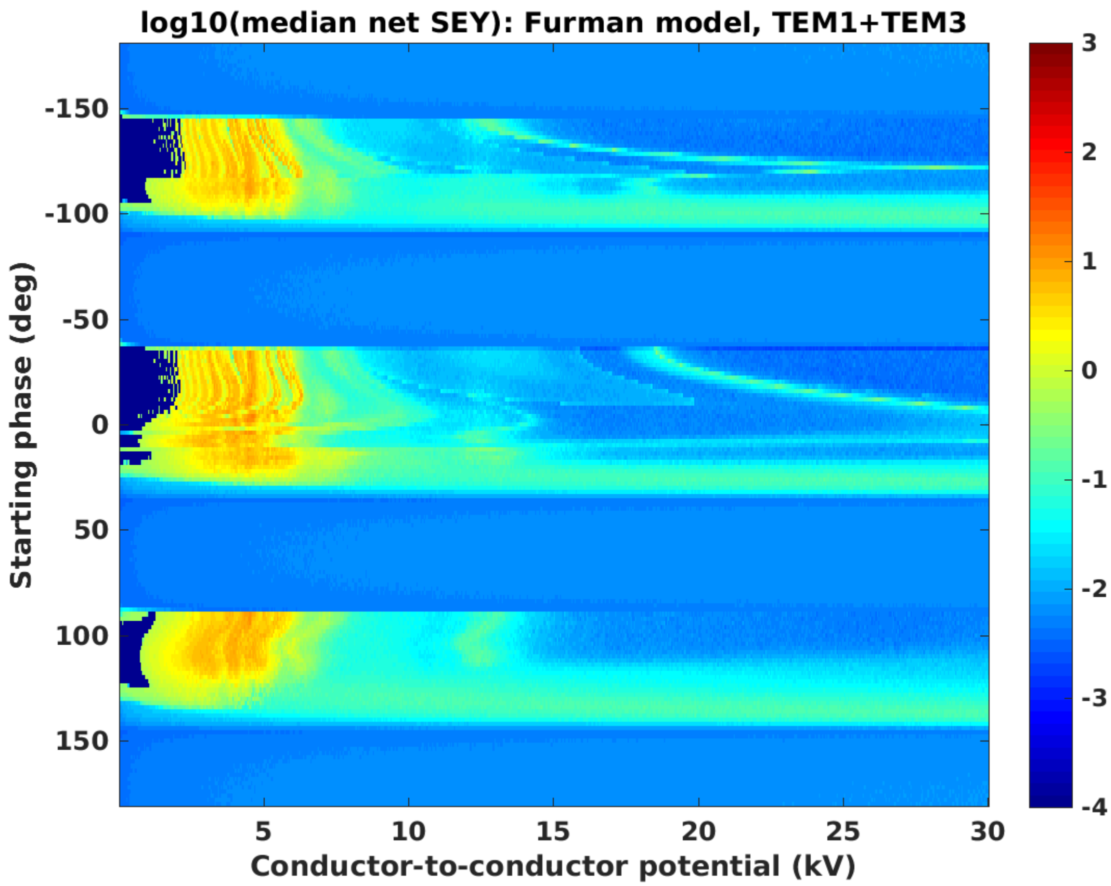

Figure 34: Median net SEY in coaxial geometry #2 using Furman's SEE model, with both the fundamental and 3rd harmonic TEM modes present. Conductor-to-conductor potential corresponds to field strength of the fundamental mode. The median is calculated over 100 Monte Carlo trials.

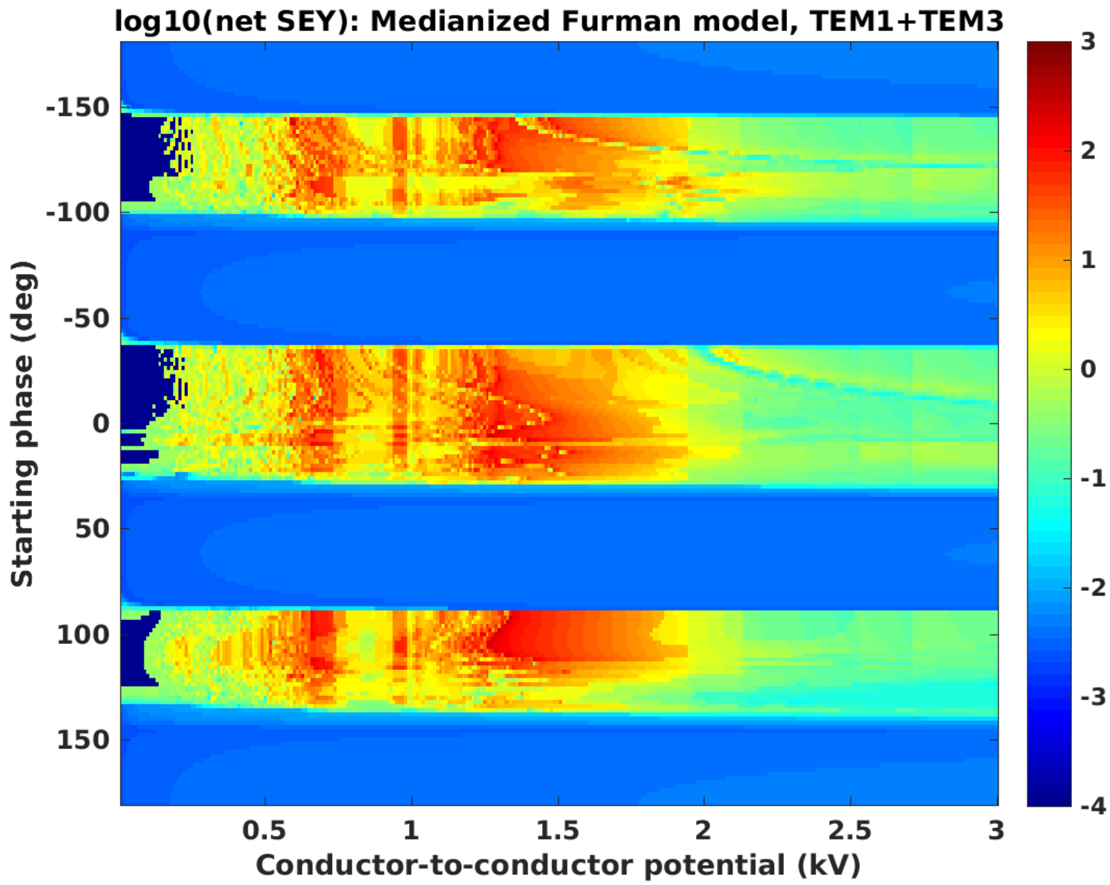

Figure 35: Net SEY in coaxial geometry #1 using the medianized Furman's SEE model, with both the fundamental and 3rd harmonic TEM modes present. Conductor-to-conductor potential corresponds to field strength of the fundamental mode.

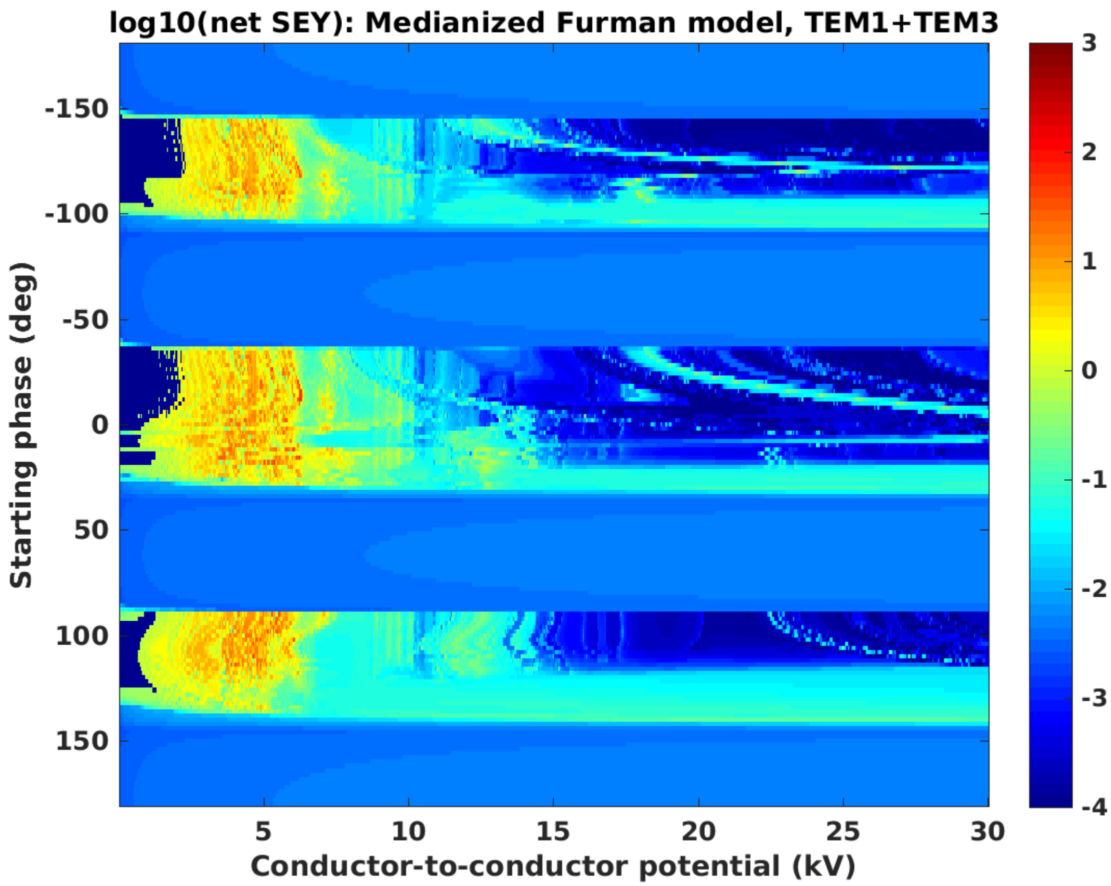

Figure 36: Net SEY in coaxial geometry #2 using the medianized Furman's SEE model, with both the fundamental and 3rd harmonic TEM modes present. Conductor-to-conductor potential corresponds to field strength of the fundamental mode.

As explained in Section 3.9, the net SEY can be related to the growth rates of multipactor current. Figures 37 and 38 show the median growth rates respectively for cavity #1 and #2 as computed using Furman's SEE model, where the median was calculated over 100 Monte Carlo trials at each (magnitude, phase) point. Figures 39 and 40 show the growth rates respectively for cavity #1 and cavity #2 as computed using the medianized Furman SEE model. Consistent with the previous net SEY and growth rate results, the medianized Furman model can yield a respectable estimate of the stochastic Furman model results. The computational costs is much less because Monte Carlo trials are avoided, at the cost of introducing some errors relative to the fully stochastic Furman SEE model.

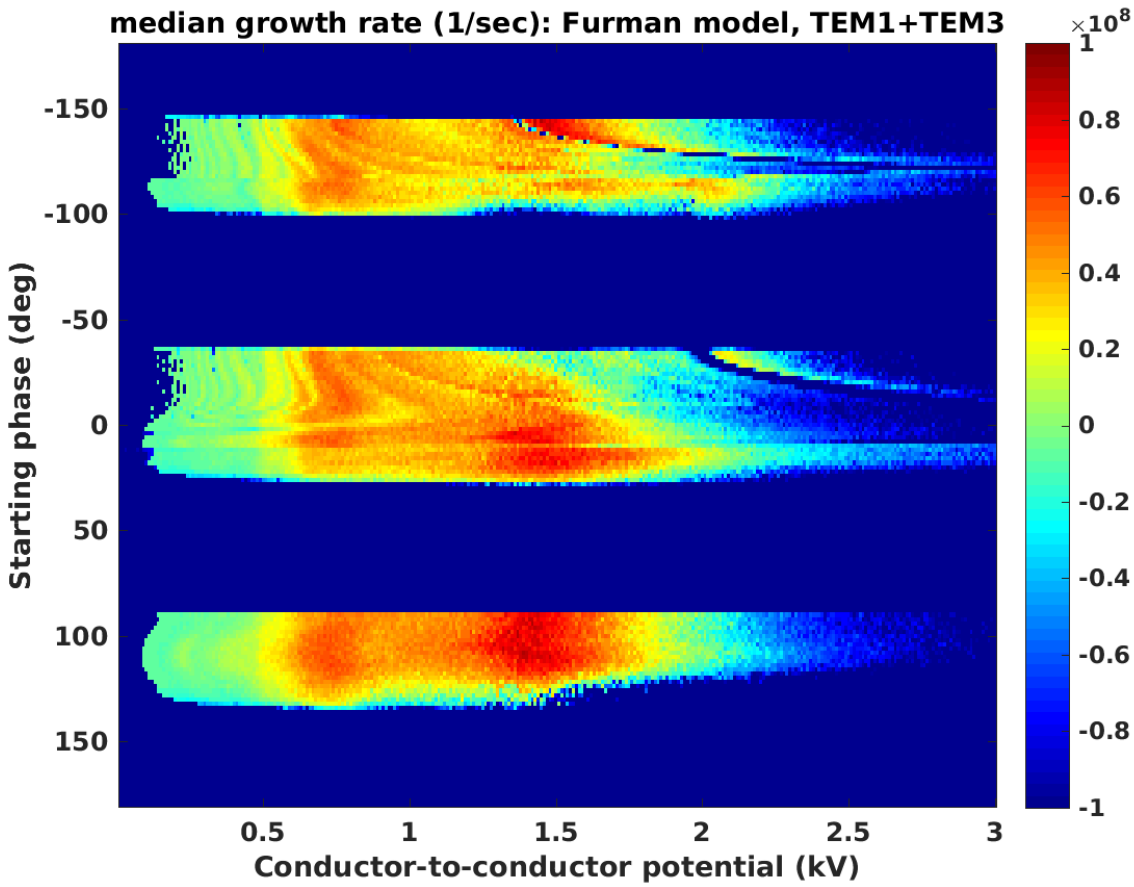

Figure 37: Median growth rate in coaxial geometry #1 using Furman's SEE model, with both the fundamental and 3rd harmonic TEM modes present. Conductor-to-conductor potential corresponds to field strength of the fundamental mode. The median is calculated over 100 Monte Carlo trials.

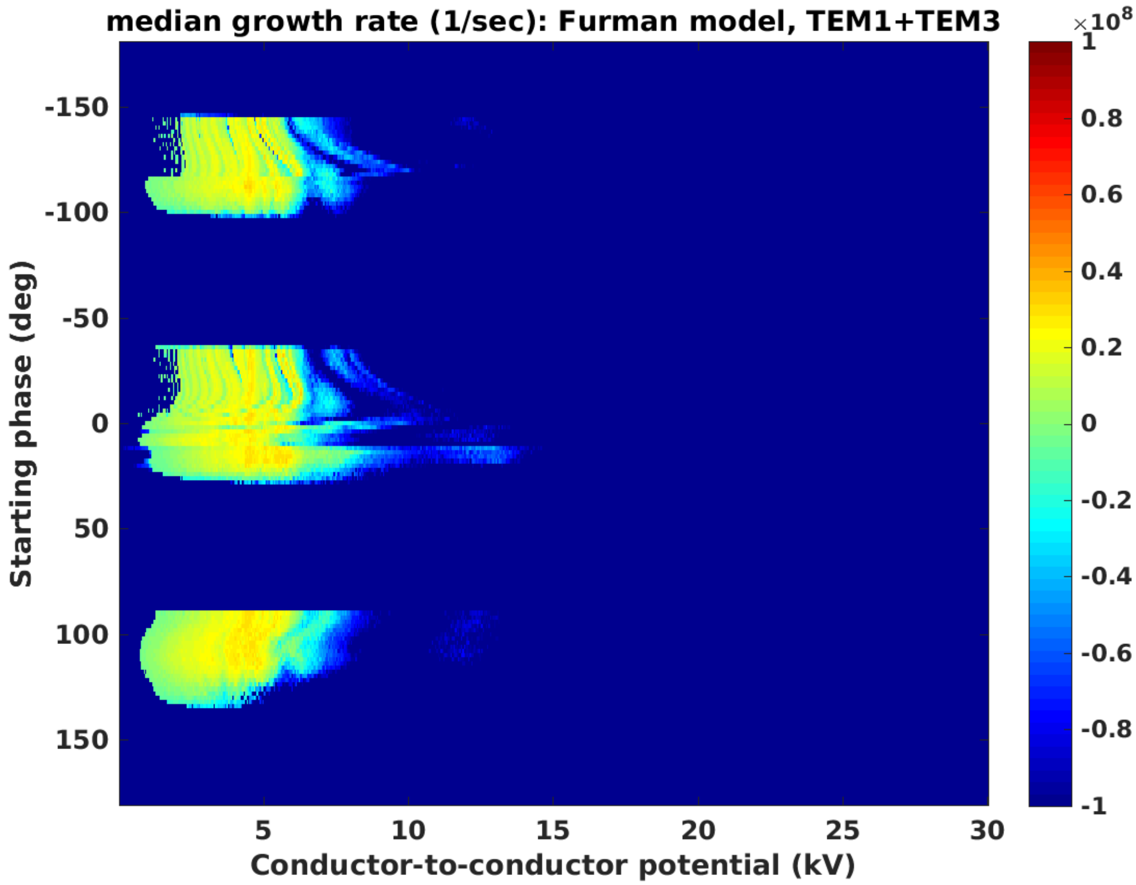

Figure 38: Median growth rate in coaxial geometry #2 using Furman's SEE model, with both the fundamental and 3rd harmonic TEM modes present. Conductor-to-conductor potential corresponds to field strength of the fundamental mode. The median is calculated over 100 Monte Carlo trials.

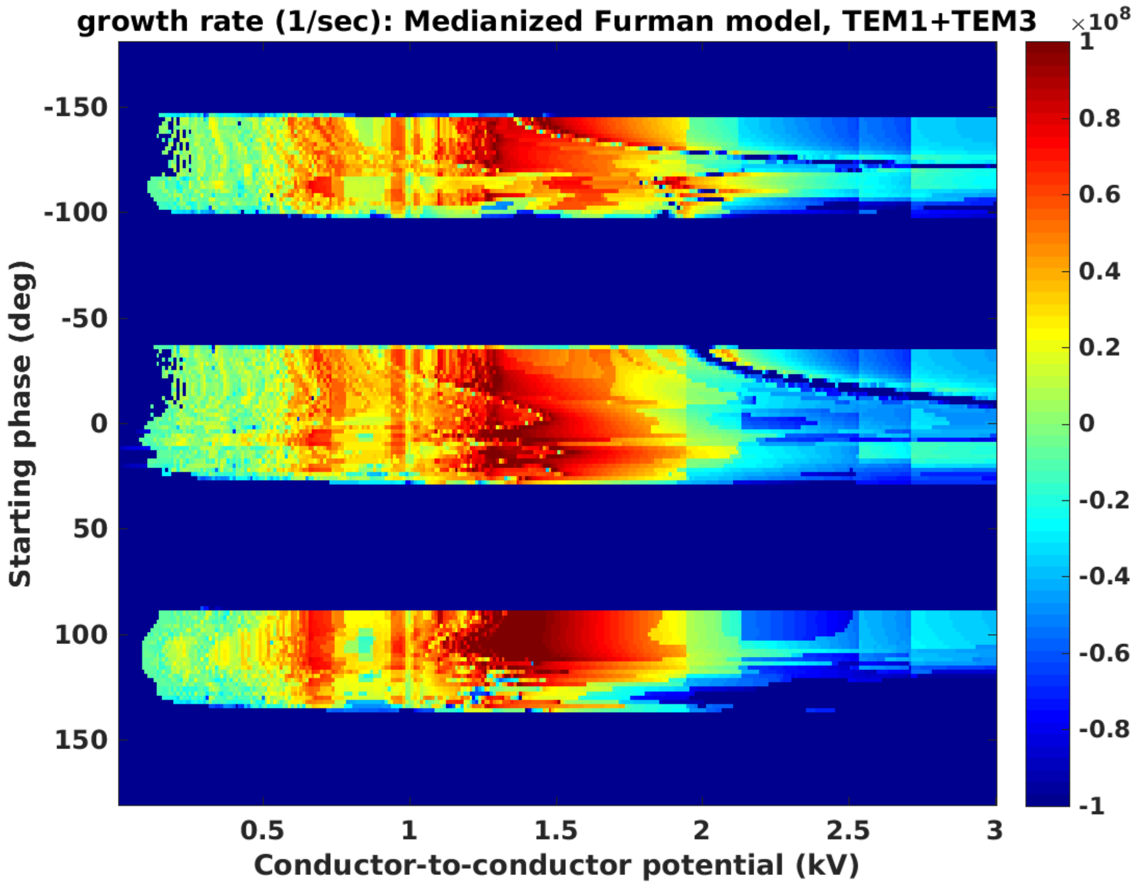

Figure 39: Growth rate in coaxial geometry #1 using the medianized Furman's SEE model, with both the fundamental and 3rd harmonic TEM modes present. Conductor-to-conductor potential corresponds to field strength of the fundamental mode.

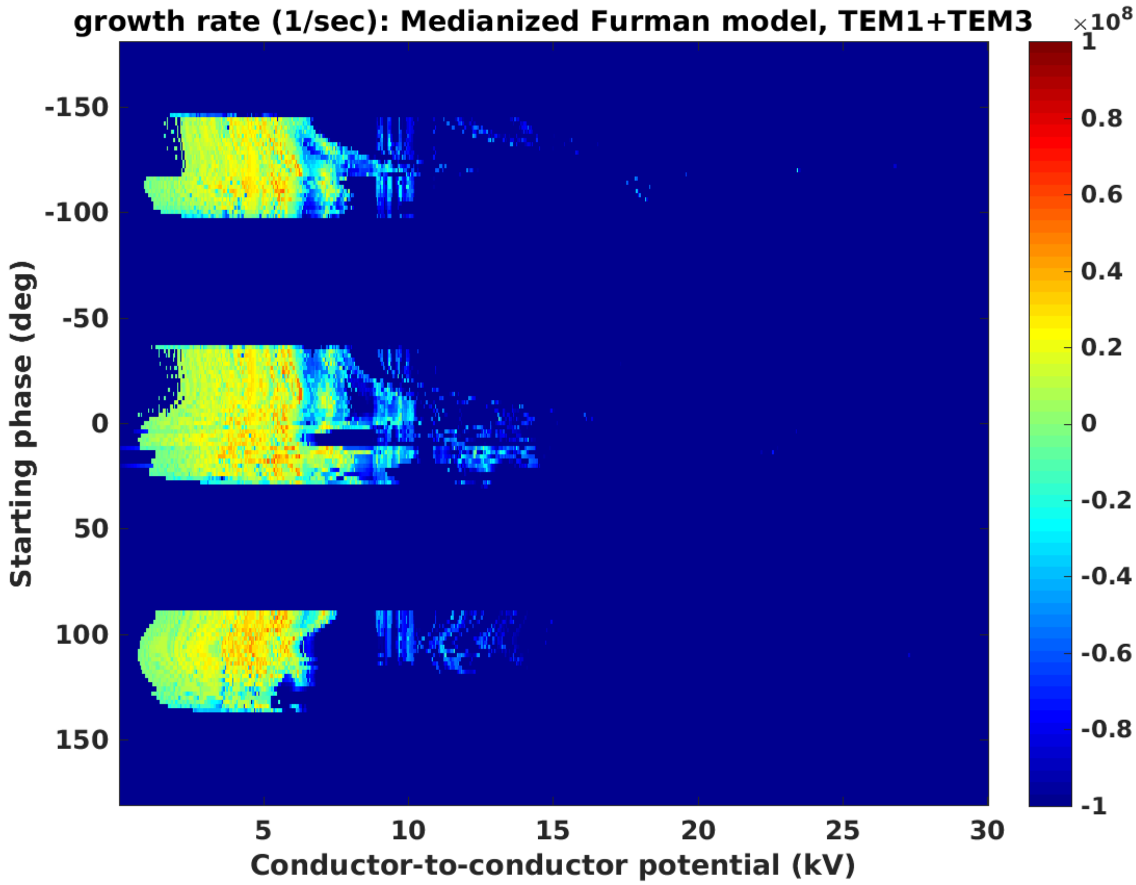

Figure 40: Median growth rate in coaxial geometry #2 using medianized Furman's SEE model, with both the fundamental and 3rd harmonic TEM modes present.

Conductor-to-conductor potential corresponds to field strength of the fundamental mode.

4.3 Total-cavity Multipactor Susceptibility with 2nd, 3rd, and 4th TEM Harmonics

This section closely follows the work presented by the author in [45].

In the previous section, we focused on the effects of a perturbative 3rd harmonic mode upon multipactor susceptibility. That analysis was limited in scope in that we only examined a single *z*-location midway through the cavity, ie. *z*=L/2 for a cavity to range from *z*=0 to *z*=L, and only one relative amplitude and one relative phase of the 3rd harmonic mode in reference to the fundamental mode. This limited scope was due to the requirement of new Monte Carlo trials needing to be run for the stochastic SEY models with every change in the system parameters. However, the medianized Furman model is reasonably accurate and completely deterministic, permitting us to avoid new Monte Carlo trials with each change in simulation parameters. In this section we use the medianized Furman model to expand our analysis to examine 2nd, 3rd, and 4th TEM harmonics of varying amplitudes and phases relative to the fundamental TEM mode, and to include other *z*-positions besides *z*=L/2. Because of the large parameter space to be examined, we restrict our analysis in this section to only coaxial geometry #1.

In the previous sections, our analysis of multipactor susceptibility consisted of generating susceptibility surfaces as functions of the fundamental mode field amplitude and the starting phase of the multipacting particles. This approach becomes impractical to analyze hundreds of combinations consisting not simply of the fundamental mode field amplitude and particle starting phase, but also the particle initial *z*-position, and the relative amplitude, phase, and harmonic order of a higher-order TEM mode. We seek to define metrics which quantify the multipactor susceptibility in some meaningful way.

With an arbitrary higher-order TEM mode present, the electric field $\boldsymbol{E}$(r,z,t) and magnetic field $\boldsymbol{B}$(r,z,t) field inside the cavity can be expressed as:

$$\boldsymbol{E}=\hat{r}\frac{V_0}{r\cdot\log(b/a)}\cdot\left(\cos(\omega t+\theta)\cdot\sin\left(\frac{\pi z}{L}\right)+\beta\cdot\cos(n\omega t+n\theta+\zeta)\cdot\sin\left(\frac{n\pi z}{L}\right)\right), \tag{4.3}$$

$$\boldsymbol{B}=-\hat{\phi}\frac{1}{c}\frac{V_0}{r\cdot\log(b/a)}\cdot\left(\sin(\omega t+\theta)\cdot\cos\left(\frac{\pi z}{L}\right)+\beta\cdot\sin(n\omega t+n\theta+\zeta)\cdot\cos\left(\frac{n\pi z}{L}\right)\right), \tag{4.4}$$

where β is the relative amplitude, ζ is the relative phase, n is the order of the perturbative higher-order TEM mode, and all the other parameters are as defined in equations 4.1 and 4.2.

Let us consider for a moment a single relative amplitude β and single relative phase ζ of a perturbative higher-order mode order n, and allow the fundamental mode field amplitude V_0, particle starting phase θ, and particle starting z-position to vary over given search ranges. If we define a metric for the resulting multipactor susceptibility over this 3-dimensional search space, we can then examine how this multipactor susceptibility metric changes as a function of the higher-order mode's parameters (β,ζ,n). We propose two possible metrics for this purpose: Metric #1 is termed the multipactor fraction, defined to be the fraction of the 3-dimensional (V_0, θ, starting z) search space in which the net SEY is greater than unity. Metric #2 is termed the exponential growth rate of multipactor current, defined as the maximum value within the 3-dimensional (V_0, θ, starting z) search space of log(net SEY)/(final recorded impact time), where log(.) denotes the natural logarithm. This is the same exponential growth rate as defined in Section 3.9.

We compute these metrics for (β,ζ,n) parameters sampled as follows: We allow the relative amplitude β to range from 0.5 to 5 in steps of 0.5, we allow the relative phase ζ to range from 0 to 2π in steps of $\pi/4$, and we examine harmonic orders $n = \{2, 3, 4\}$. For each combination of these perturbative mode parameters, we compute the metrics on a (V_0, θ, starting z) space discretized as follows: V_0 ranges from 30 V to 10 kV in 101 logarithmically-spaced points, θ spans the unit circle in 45 equally spaced samples starting from θ=0, and the starting z ranges from 0.1L to 0.5L in steps of 0.1L; note that the electric field is zero at z=0, and that due to symmetry the fields at locations of z>0.5L do not offer any different multipactor conditions than for z<0.5L, and thus we do not need to simulate these additional cases. As a point of reference, when the fundamental mode is present without any perturbative modes, metric #1 (multipactor fraction) yields 10.2%, and metric #2 (exponential growth rate) yields $10^{7.91}$ sec^{-1} when computed over the above-defined (V_0, θ, starting z) space.

Figures 41, 42, and 43 respectively show the multipactor severity metrics for harmonic orders 2, 3, and 4. The results show that lower-amplitude secondary modes either slightly mitigate or have no effect on the global metrics of multipactor severity. These results demonstrate that while relatively modest changes in multipactor susceptibility can be caused by the introduction of these selected TEM secondary modes, no major changes in multipactor susceptibility are noted: multipactor may be reduced in one location of (V_0, θ, starting z) space, but increased in another location. However, it is worth noting that the perturbative modes may still have some ability to increase or suppress multipactor at a particular location within a resonant structure, depending on what our goals may be, such as avoiding damage to a sensitive location, or intentionally attenuating field strength in a non-linear way.

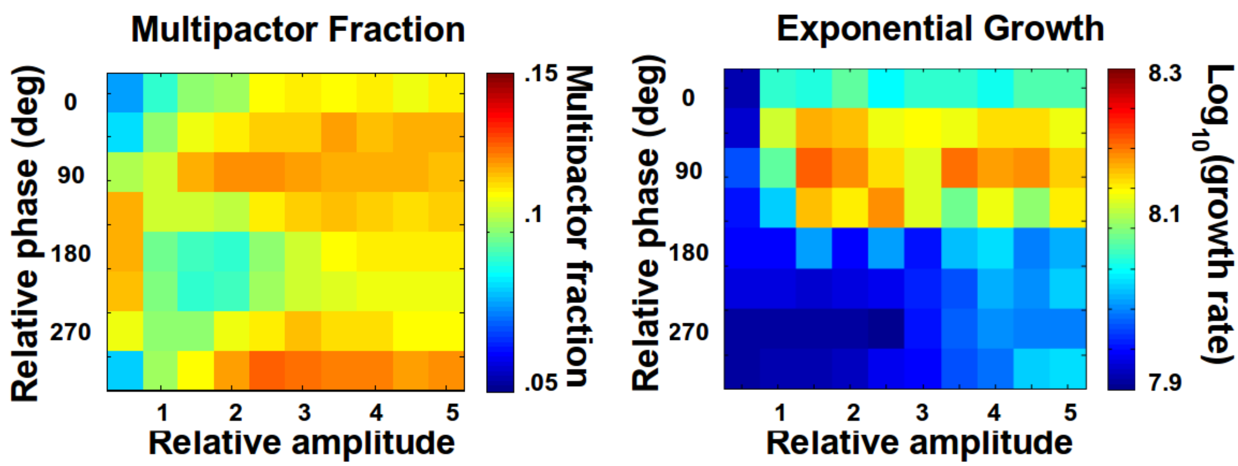

Figure 41: Multipactor susceptibility metrics for a 2^{nd} harmonic TEM mode in addition to the fundamental TEM mode.

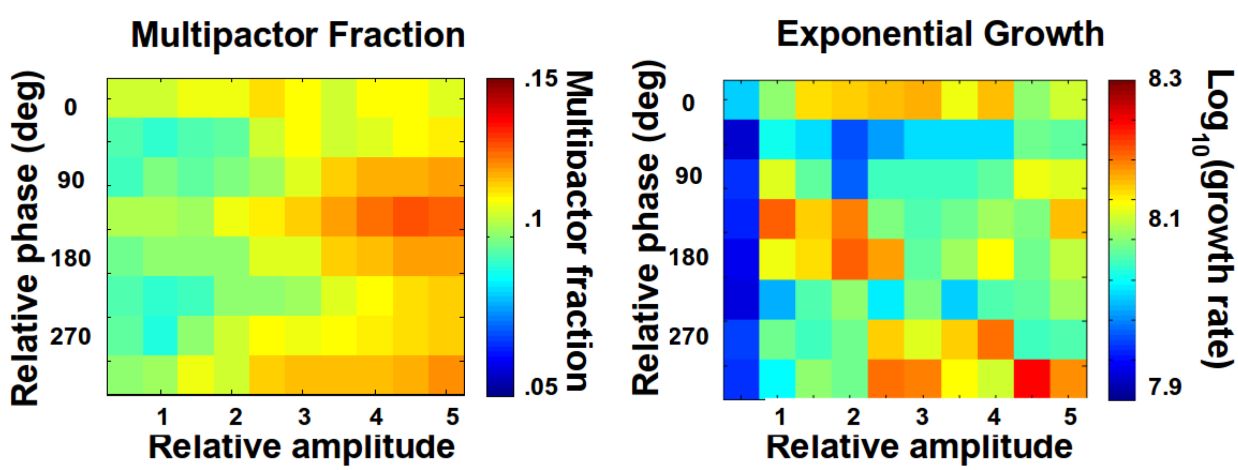

Figure 42: Multipactor susceptibility metrics for a 3^{rd} harmonic TEM mode in addition to the fundamental TEM mode.

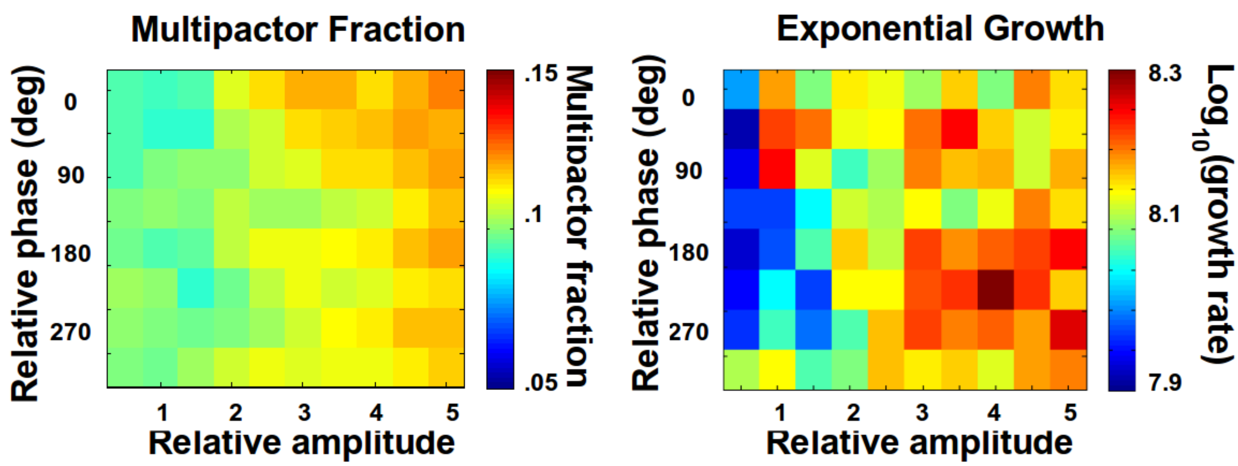

Figure 43: Multipactor susceptibility metrics for a 4th harmonic TEM mode in addition to the fundamental TEM mode.

4.4 Coaxial Waveguide Multipactor Susceptibility with Non-integer TEM Harmonics

In the previous section, we examined how multipactor susceptibility was affected within coaxial cavity geometry #1. Because we were examining a bounded cavity, we were restricted to standing wave harmonics that were integer multiples of the frequency of the fundamental mode. However, in unbounded structures such as a waveguide, a continuum of frequencies are possible. In this section, we examine multipactor susceptibility in the presence of traveling wave perturbations, which are both integer and non-integer multiples of the fundamental frequency. In order to maintain the analysis as consistent as possible to the bounded geometry case, we use the same coaxial inner and outer radii as was used for coaxial cavity geometry #1, but in this case have an unbounded *z*-dimension.

In order to keep this analysis computationally tractable, we only examine the case of the fundamental TEM mode and a single perturbative TEM mode at a different frequency, where both modes propagate in the negative *z*-direction. For this unbounded geometry with two TEM modes, the electric field ***E***(r,z,t) and magnetic field ***B***(r,z,t) inside the waveguide can be expressed as:

$$\boldsymbol{E}=\hat{r}\frac{V_0}{r\cdot\log(b/a)}\cdot\left(\cos\left(\omega\cdot(t+z/c)+\theta\right)+\beta\cdot\cos\left(n\omega\cdot(t+z/c)+n\theta+\zeta\right)\right), \tag{4.5}$$

$$\boldsymbol{B}=-\hat{\phi}\frac{1}{c}\frac{V_0}{r\cdot\log(b/a)}\cdot\left(\cos\left(\omega\cdot(t+z/c)+\theta\right)+\beta\cdot\cos\left(n\omega\cdot(t+z/c)+n\theta+\zeta\right)\right), \tag{4.6}$$

where n represents the frequency ratio of the perturbative mode to the fundamental mode (positive real number), c denotes the speed of light in vacuum, and all other parameters are as defined in equations (4.1) through (4.4).

We consider perturbative modes with frequency ratios n = {0.5, 0.75, 1.5, 2, 2.5, 3, 3.5, 4}. For each perturbative mode, we consider relative magnitude β ranging from 0 to 4 in 13 equally-spaced samples, and relative phase shift ζ sampled at 15 equally-spaced samples around the unit circle, starting at ζ=0. For each perturbative mode defined by given choice of (β,ζ,n), we compute a net SEY surface as V_0 ranges from 30 V to 10 kV over 41 logarithmically-spaced samples, and θ spans the unit circle in 30 equally-spaced samples around the unit circle, starting at θ=0. The starting z values range from 0 to λ/2 in steps of λ/10, where λ is the wavelength of the fundamental mode; note that this covers all possible multipactor scenarios, since multipactor simulations at other z values map to the range of 0 to λ/2 by an appropriate choice of field phases which are already being sampled.

For each sample point, we compute the net SEY as has been consistently done throughout this dissertation as described in Section 3.3: we simulate particle trajectories for 10 cycles, where a cycle is defined to be one period of the fundamental mode, or one boundary impact, whichever occurs first. The net SEY is defined as the product of each single-impact SEY, and is understood to be zero if at least two boundary impacts do not occur over the simulation period.

For each perturbative mode defined by given choice of (β,ζ,n), we assess the multipactor susceptibility using two metrics. The first metric is the multipactor fraction, which is defined to be the fraction of (V_0, θ, starting z) samples which have a net SEY greater than unity. The second metric is the maximum geometric average δ_{AVG} of the SEY within the (V_0, θ) search space, defined as $\delta_{AVG} = (\text{Net SEY})^{1/(\#\ \text{Impacts})}$; the geometric average gives a measure of how quickly the multipactor grows per unit impact. As a baseline for comparison, without a perturbative higher-order mode present, the multipactor fraction is approximately 10.7%, and the maximum per-impact delta is approximately 2.0.

The results of the two susceptibility metrics are shown in Figures 44 through 51 respectively for perturbative modes with frequency ratios n = {0.5, 0.75, 1.5, 2, 2.5, 3, 3.5, 4}. For most frequency ratios, the results for both metrics do not show a significant improvement; this means that if we reduce multipactor susceptibility in one location in the waveguide, then we are increasing the susceptibility in another location in the waveguide, either in terms of the total fraction of the search space capable of supporting multipactor, or by focusing multipactor resonances in such a way as to increase the per-impact delta and the corresponding multipactor growth rate within the search space.

However, the results in Figure 44 for the half-harmonic n=0.5 do show an interesting behavior: for a harmonic relative phase around ζ=270º and relative amplitudes β in the vicinity of 1 to 2.5, both the multipactor fraction and the max per-impact-delta are both reduced. The multipactor fraction reduces to approximately 1%, and the maximum per-impact delta reduces down to approximately 1.5. Note that there is nothing special about the half-harmonic n=0.5, other than that it happens to work well for this particular geometry and fundamental frequency. These results suggest that with at least some perturbing mode conditions in coaxial waveguide geometries, further examination is warranted for multipactor reduction at a target TEM mode by using a perturbing TEM mode.

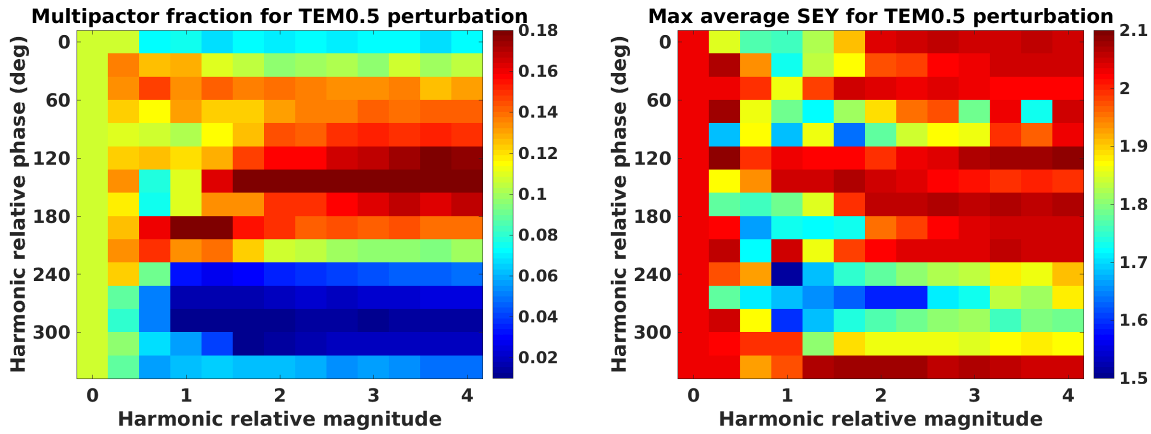

Figure 44: Coaxial waveguide multipactor susceptibility metrics with a TEM0.5 perturbation.

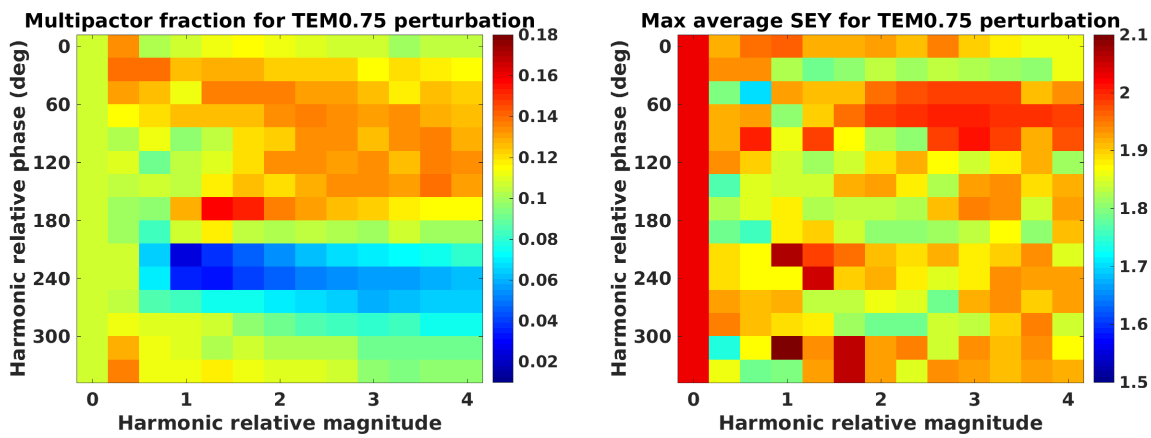

Figure 45: Coaxial waveguide multipactor susceptibility metrics with a TEM0.75 perturbation.

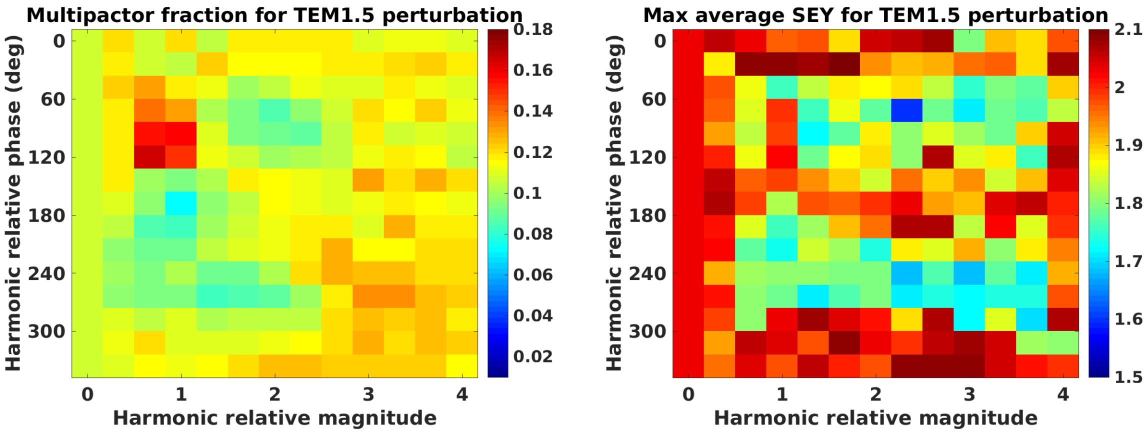

Figure 46: Coaxial waveguide multipactor susceptibility metrics with a TEM1.5 perturbation.

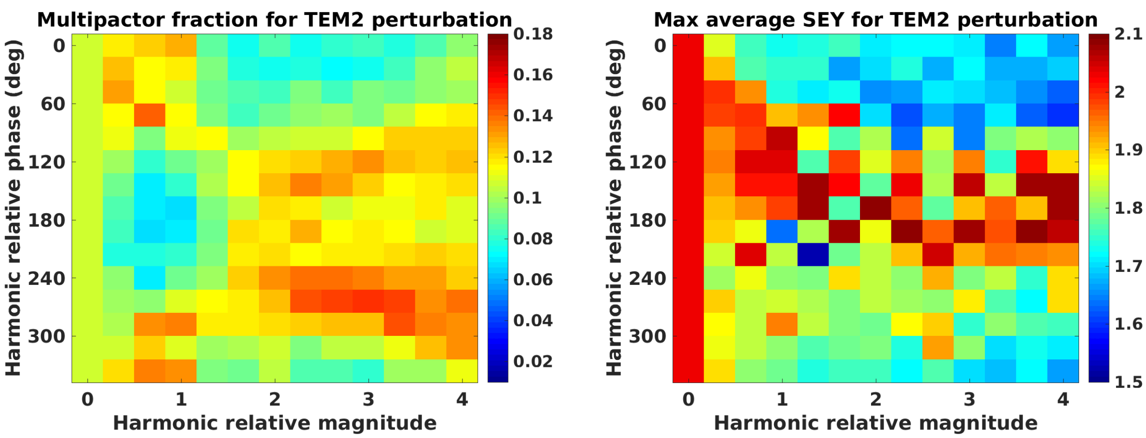

Figure 47: Coaxial waveguide multipactor susceptibility metrics with a TEM2 perturbation.

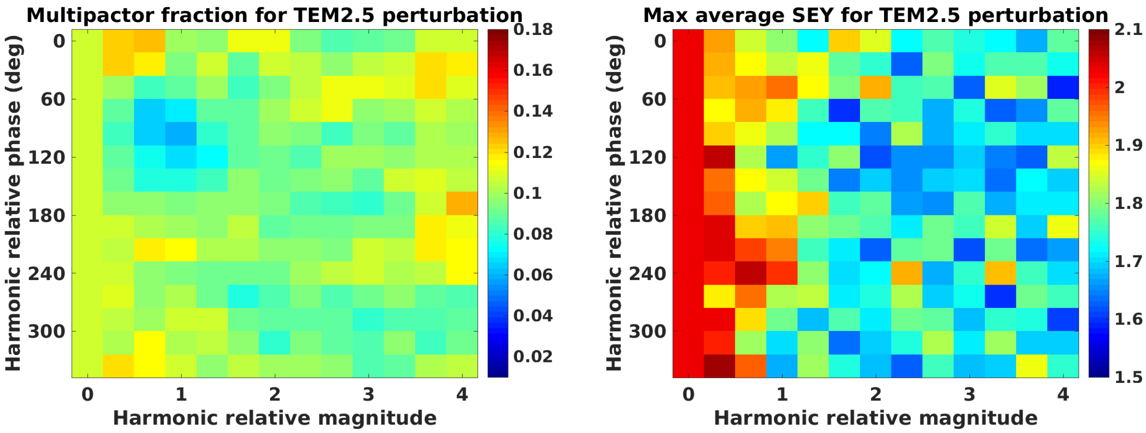

Figure 48: Coaxial waveguide multipactor susceptibility metrics with a TEM2.5 perturbation.

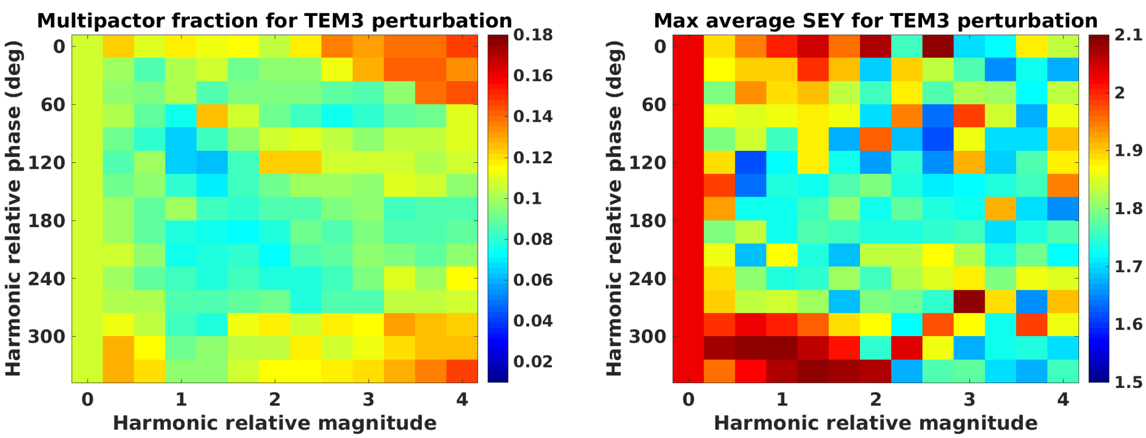

Figure 49: Coaxial waveguide multipactor susceptibility metrics with a TEM3 perturbation.

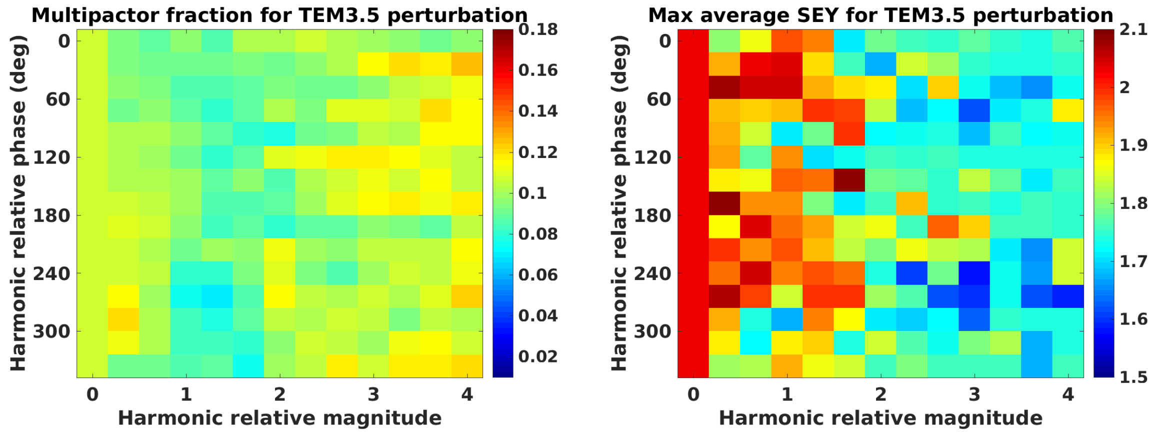

Figure 50: Coaxial waveguide multipactor susceptibility metrics with a TEM3.5 perturbation.

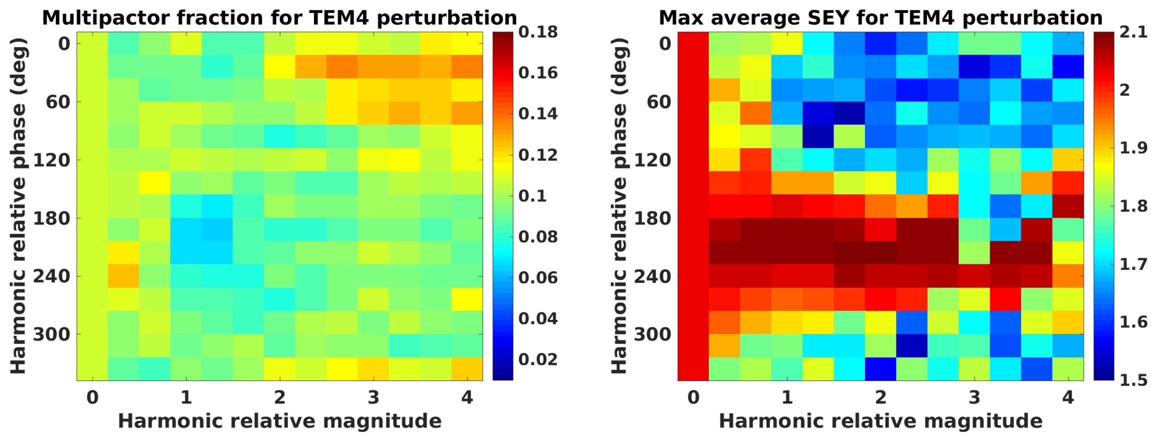

Figure 51: Coaxial waveguide multipactor susceptibility metrics with a TEM4 perturbation.

4.5 Conclusions

In this chapter we have examined the effect that perturbative modes can have upon multipactor which is primarily driven by a different mode. We first compared the predicted multipactor results using the same SEE models as were introduced in Chapter 3, with the specific test case of a particular TEM3 mode present in the cavity alongside the fundamental TEM1 mode. We then generalized this analysis by using the medianized Furman SEE model to look over a wide range of perturbing mode parameters in notional cavity #1, and a coaxial waveguide sharing the same inner and outer radii dimensions. In most cases, the total susceptibility to multipactor when considered over the entire volume was not observed to significantly change, but the perturbative modes may still have some ability to increase or suppress multipactor at a particular location within a resonant structure. We also noted that for the particular case of the coaxial waveguide being perturbed by a half-harmonic TEM mode, the multipactor susceptibility over the entire volume was non-trivially reduced, which suggests that with at least some perturbing mode conditions in coaxial waveguide geometries, further examination is warranted for multipactor reduction at a target TEM mode by using a perturbing TEM mode.

CHAPTER 5: Refinement of the medianized Furman SEE model

This chapter is an expansion of the early work presented by the author in [46] and [47].

5.1 Introduction

Furman's medianized SEY model is a reasonable approach to defining a deterministic SEY model which can provide reasonably accurate multipactor simulations without resorting to Monte Carlo trials. In defining that model, one of the unaddressed tradeoffs is whether or not the median is the best cumulative statistic to use when characterizing the emission energies of Furman's SEE model. We now turn our attention to examining the effects of using different cumulative statistics, which is a generalization of the medianized variant of Furman's SEE model. We refer to this collection of SEE models as reduced-order Furman SEE models.

This class of reduced-order Furman SEE models can be used to quickly perform multipactor simulations when simulation speed is more important than fully characterizing multipactor behavior, for example when carrying out swept-parameter simulations over a large space of possible designs for a given application. Once the design parameters are approximately determined, Furman's full model could be used to fine-tune and optimize the final design. In order to evaluate the performance of the reduced-order Furman SEE models, we consider three different error metrics, which may be more or less applicable depending on a given end-user design goal.

5.2 Error metrics

Let us begin by considering the cavity #1 geometry (defined in Section 3.1) which is excited solely by a TEM1 mode, as given by Equations (3.1) and (3.2) with n=1. We allow V_0 to vary from 10 V to 3000 V in steps of 10 V, and we allow θ to range from -π/2 to π/2 over 181 points. For each (voltage, starting phase) point in our simulation space, we run 100 Monte Carlo trials using Furman's SEE model for copper, and the net SEY for each Monte Carlo trial is calculated as has been consistently done throughout this dissertation: we simulate particle trajectories for 10 cycles, where a cycle is defined to be one period of the fundamental mode, or one boundary impact, whichever occurs first. The net SEY is defined as the product of each single-impact SEY, and is understood to be zero if at least two boundary impacts do not occur over the simulation period.

For each point in our simulation space, we calculate the mean and median of the net SEY of the Monte Carlo trials, which is plotted in Figure 52 below. We note that in many places the mean net SEY exceeds the median net SEY. This is due to a small number of trials in which the stochastic emission energies and directions happen to yield a very large net SEY, which affects the mean statistic but not the median statistic.

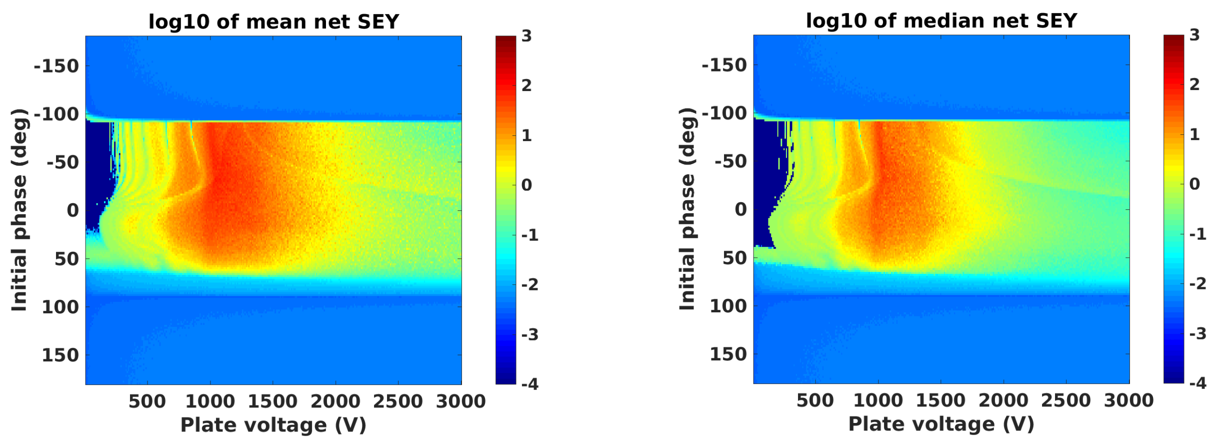

Figure 52: Mean (left) and median (right) results of the net SEY as computed from 100 Monte Carlo trials using Furman's SEE model on cavity #1 with only TEM1 excitation.

Furman's SEY model, while accurate, necessitates computationally costly Monte Carlo simulations to characterize multipactor susceptibility. In Section 3.8, in order to save computational cost, we proposed the use of the median values of the stochastic variables in Furman's model. This results in a deterministic (but still impact energy-dependent and angle-dependent) emission energy and emission angle. Such a deterministic SEE model will clearly not explore the entire phase space, but previous results suggest that it can do well in approximating the results of the full Furman model. As a generalization, consider using other percentiles instead of just the 50th percentile (median) values from the stochastic variable cumulative distributions. Figure 53 shows the resulting net SEY surfaces when we use the default median (50^{th} percentile) emission energy, as well as the 25^{th} and 75^{th} percentiles of the emission energies from Furman's stochastic model.

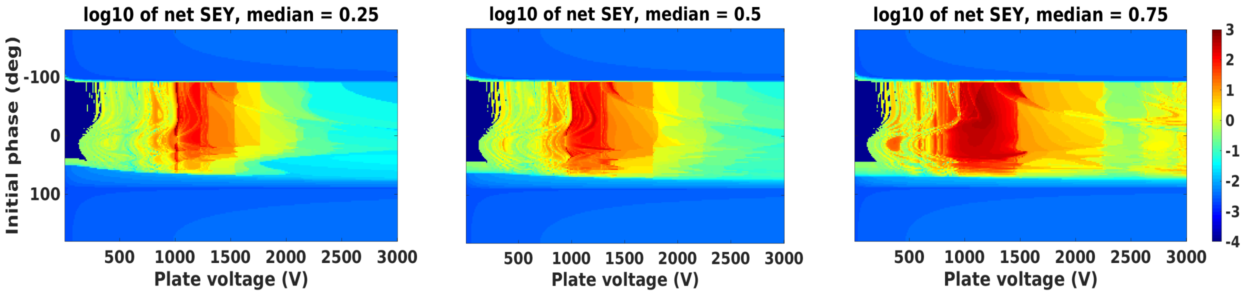

Figure 53: Net SEY using reduced-order Furman SEE model with 25th, 50th, and 75th percentile statistics, respectively shown from left to right, for cavity #1.

Let us now consider how we can quantify the error of the resulting net SEY surfaces when the cumulative statistic of Furman's stochastic variables is varied. One approach to quantify the level of agreement is by computing the root mean square error (RMSE) between the net SEY as computed via the full Furman model and the reduced-order Furman models. Figure 54 shows the RMS error between the reduced-order approximation and full Furman model as a function of the cumulative percentile statistic used. The RMSE varies between approximately 10 and 100 which correspond to values of 1 to 2 on the logarithmic plot scale, which may appear overwhelming, but it is important to note that slight changes in the SEY for each impact can yield significant changes to the net SEY after multiple bounces.

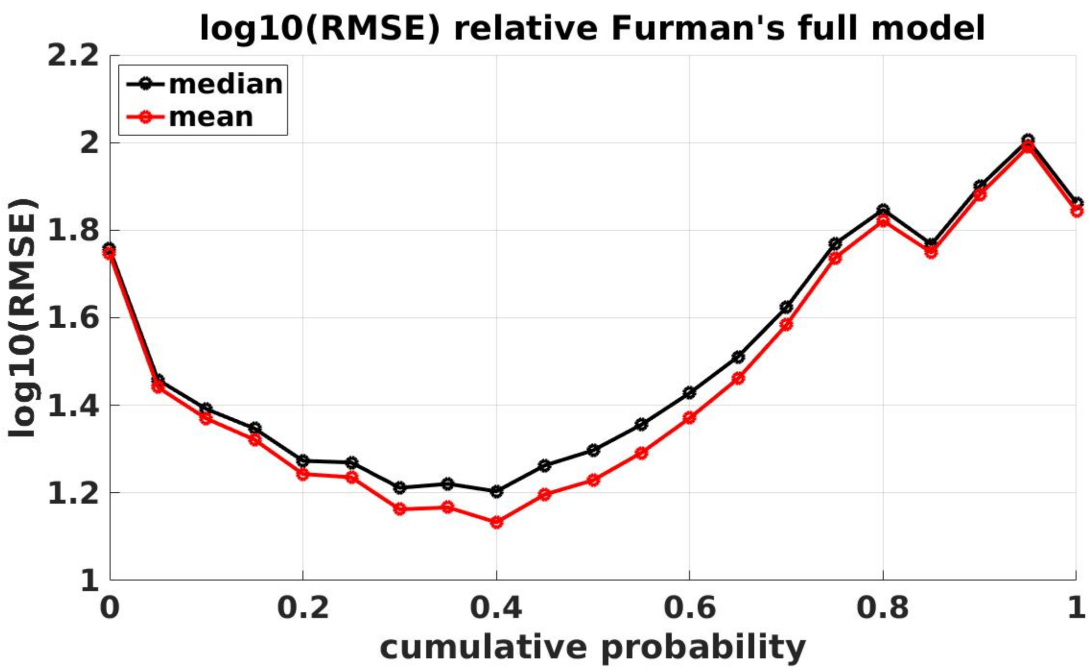

Figure 54: Root mean square error (RMSE) for the net SEY of the reduced-order Furman model, as a function of cumulative percentile used. The errors are shown for the reduced-order model as compared to both the median and mean results of 100 Monte Carlo trials using Furman's fully stochastic model within cavity #1.

A second approach to quantifying the error between the full Furman model and the reduced-order variants is to compute the geometric average δ_{AVG} of the net SEY over the individual surface impacts, where $\delta_{AVG} = (\text{Net SEY})^{1/(\#\ \text{Impacts})}$, with the understanding that if there are less than two impacts then we set the geometric average for that trial to zero, since the net SEY is zero as explained in Section 3.3. Figure 55 shows both the mean and the median of δ_{AVG} as generated from 100 Monte Carlo trials of Furman's model, and in Figure 56, we show the geometric average SEY as computed from a reduced-order model based upon the 25th, 50th, and 75th percentiles of the emission energies of Furman's stochastic model. Figure 57 shows the resulting RMSE of the geometric averaged reduced-order Furman results for cumulative probabilities ranging from 0 to 100th percentiles, as compared to both the mean and median of δ_{AVG} determined from 100 trials of the full Furman model.

Note that the RMSE for the geometric average SEY provides a better intuitive error metric for the similarity of the SEY predictions between the reduced-order Furman and full Furman SEE models. For example, with this metric, a value of 0.1 means that the error in secondary electron yield predictions between Furman's full model and the reduced-order models are on the order of 0.1, where for comparison the secondary electron yield of most metals typically ranges between 0 and approximately 2 depending upon impact energy and angle.

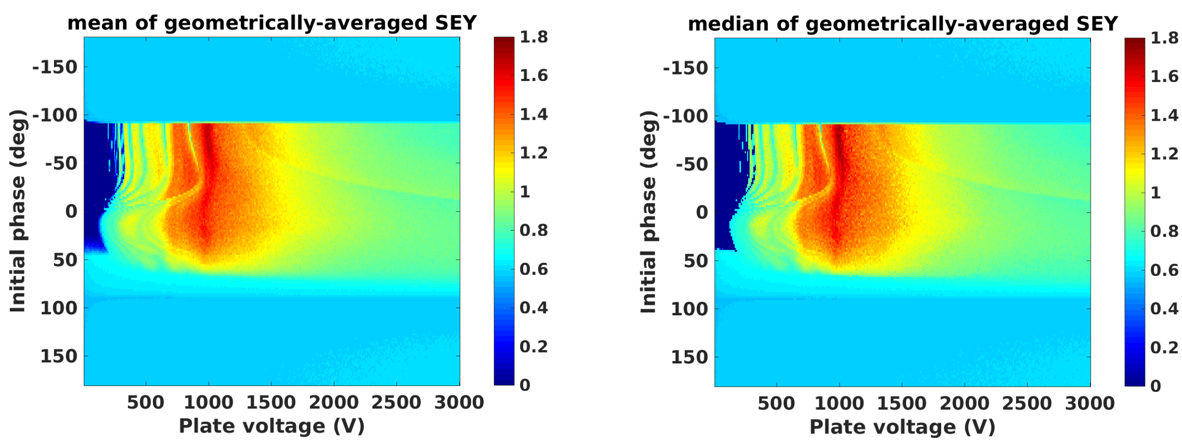

Figure 55: Results of the geometric averaged SEY for 100 Monte Carlo trials using Furman's SEE model on coaxial cavity #1 with only TEM1 excitation. Shown are mean (left) and median (right).

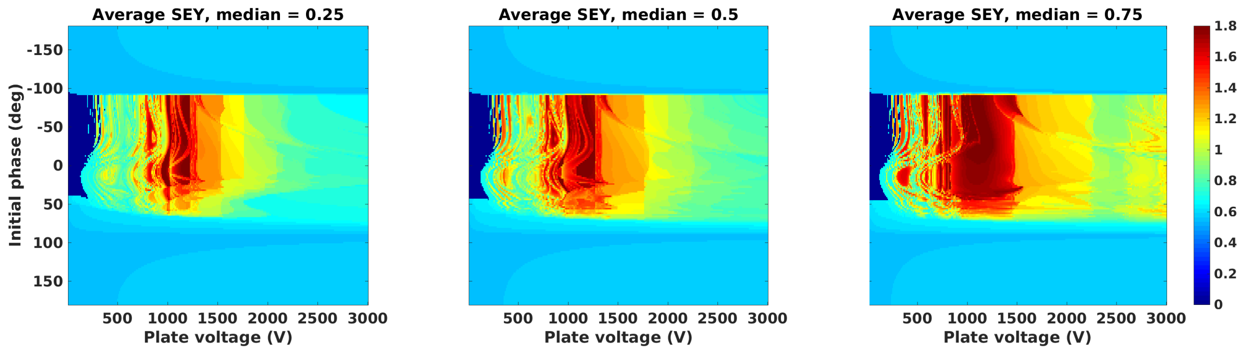

Figure 56: Geometric averaged SEY for reduced-order Furman models with 25th, 50th, and 75th percentile statistics, respectively shown from left to right, for coaxial cavity #1.

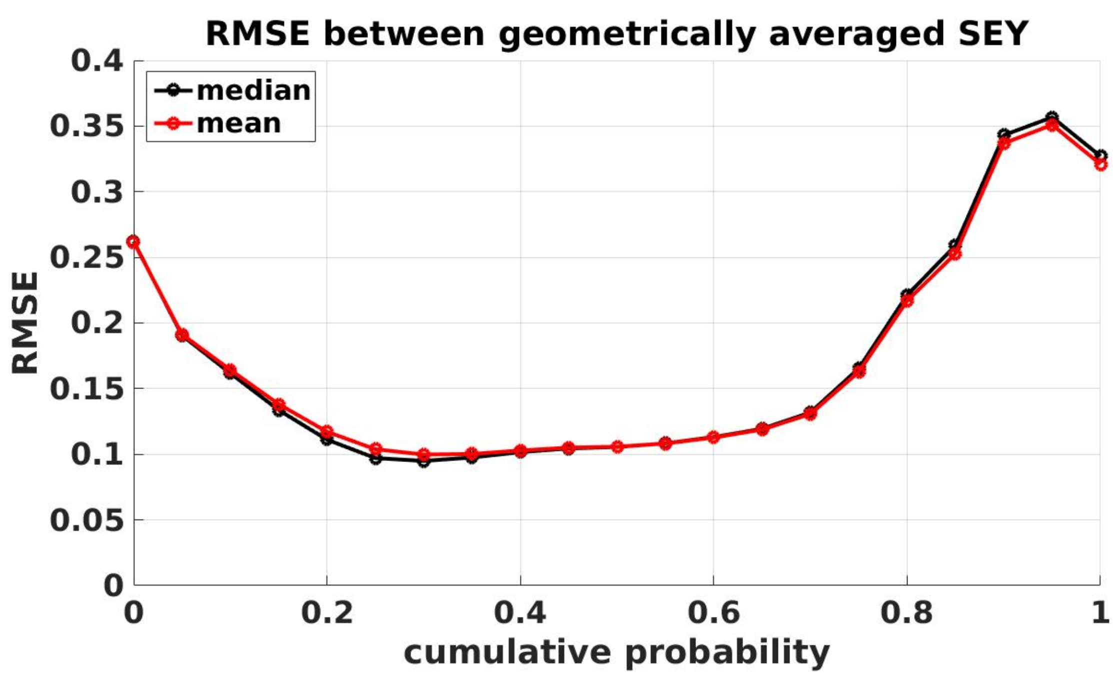

Figure 57: Root mean square error (RMSE) of the geometric averaged SEY for the reduced-order Furman model, as a function of cumulative percentile used. The errors are shown for the reduced-order model as compared to both the median and mean results of 100 Monte Carlo trials using Furman's fully stochastic model within coaxial cavity #1.

In addition to quantifying the error in net SEY prediction between a reduced-order Furman model and the fully-stochastic Furman model, in many situations we are primarily concerned with knowing whether or not multipactor can occur, without concern for accurately knowing the net SEY. In order to handle such a situation, we define the growth-decay error (GDE) as follows: For each (voltage, phase) point, if both the full Furman model and the reduced-order Furman model agree as to whether or not multipactor is possible, then assign a value of 0; if there is disagreement, then assign a value of 1. The GDE is then calculated to be the fraction of non-zero values over the entire search space. It can range from 0 (perfect agreement) to 1 (no agreement). This error gives a measure of how well the reduced-order Furman model predicts the presence or absence of multipactor, as compared to Furman's full model. The growth-decay error between the full Furman model and the reduced-order Furman model, as a function of cumulative percentile used, is shown in Figure 58.

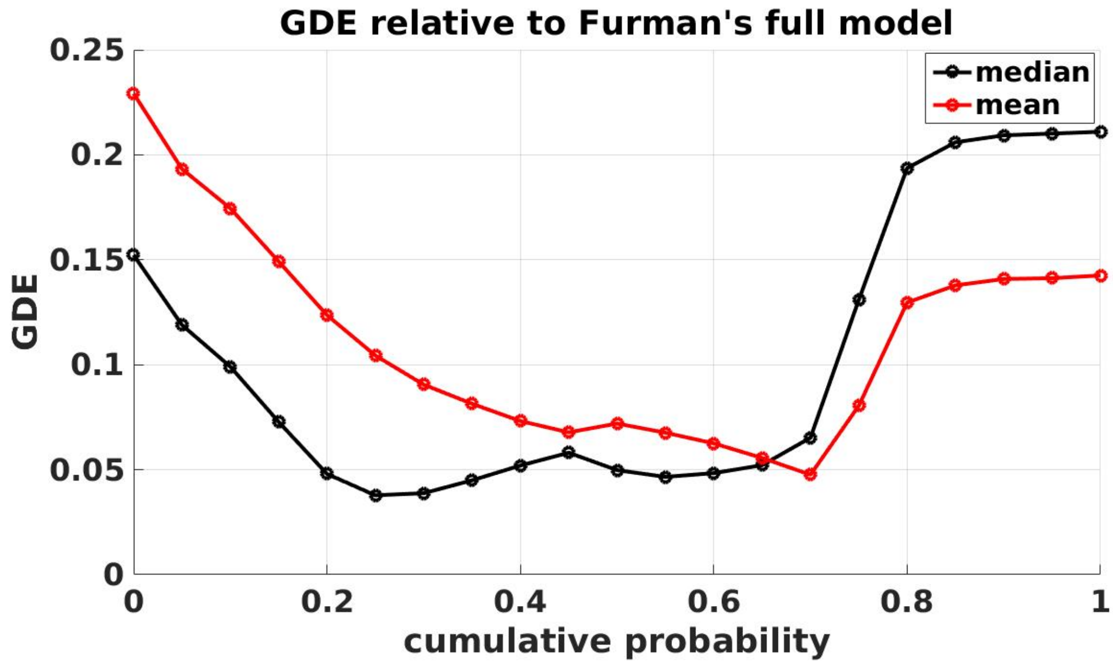

Figure 58: Growth-decay error (GDE) of the reduced-order Furman model, as a function of cumulative percentile used. The error is shown for the reduced-order model as compared to both the median and mean results of 100 Monte Carlo trials using Furman's fully stochastic model within coaxial cavity #1.

We have now defined three error metrics which we will use to examine how well the reduced-order Furman models agree with the fully stochastic Furman model. Before proceeding to do this in the next section, let us succinctly summarize what each metric tells us: The RMSE metric tells us how well the net SEY surfaces are in agreement after multiple surface impacts; the RMSE for geometrically-averaged SEY tells us how well the underlying SEY models are in agreement for a single surface impact; and the GDE tells us how well we can predict the presence or absence of multipactor.

5.3 Error performance for different geometries and excitations

With the three error metrics defined in the previous section, we now are in a position to examine how well the reduced-order Furman models can approximate the full Furman model in both coaxial cavities #1 and #2, and with just a TEM1 mode present as defined in equations (3.1) and (3.2), or with both TEM1 and TEM3 modes present as defined in equations (4.1) and (4.2). The net SEY surfaces for cavity #1 with TEM1 excitation were shown in figure 5.1 in the previous section. For completeness, we show the corresponding net SEY surfaces for cavity #1 with both the TEM1 and TEM3 mode present in Figure 59, for cavity #2 with a TEM1 mode present in Figure 60, and for cavity #2 with a TEM1 and TEM3 mode present in Figure 61. For all the results in this chapter, with cavity #1 we allow V_0 to vary from 10 V to 3000 V in steps of 10 V; with cavity #2 we allow V_0 to vary from 50 V to 30000 V in steps of 50 V. For both of the cavity results in this chapter, we allow θ to range from -π/2 to π/2 in 180 steps.

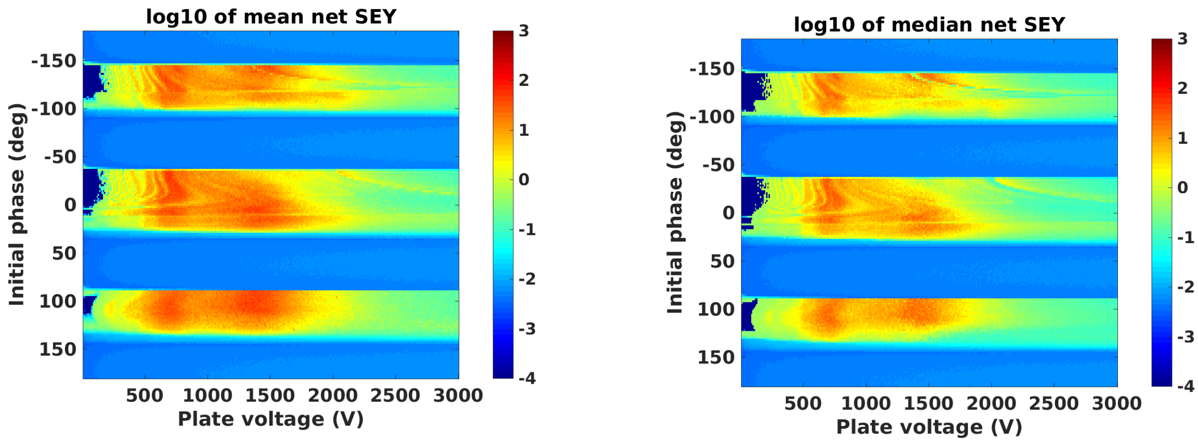

Figure 59: Results of the net SEY as computed from 100 Monte Carlo trials using Furman's SEE model on cavity #1 with both TEM1 and TEM3 modes present. Shown are mean (left) and median (right).

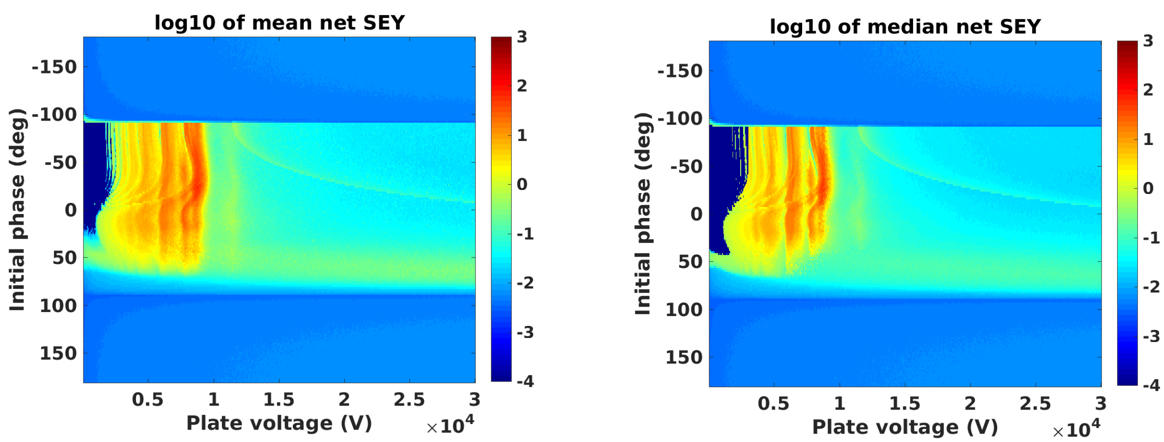

Figure 60: Results of the net SEY as computed from 100 Monte Carlo trials using Furman's SEE model on cavity #2 with only TEM1 excitation. Shown are mean (left) and median (right).

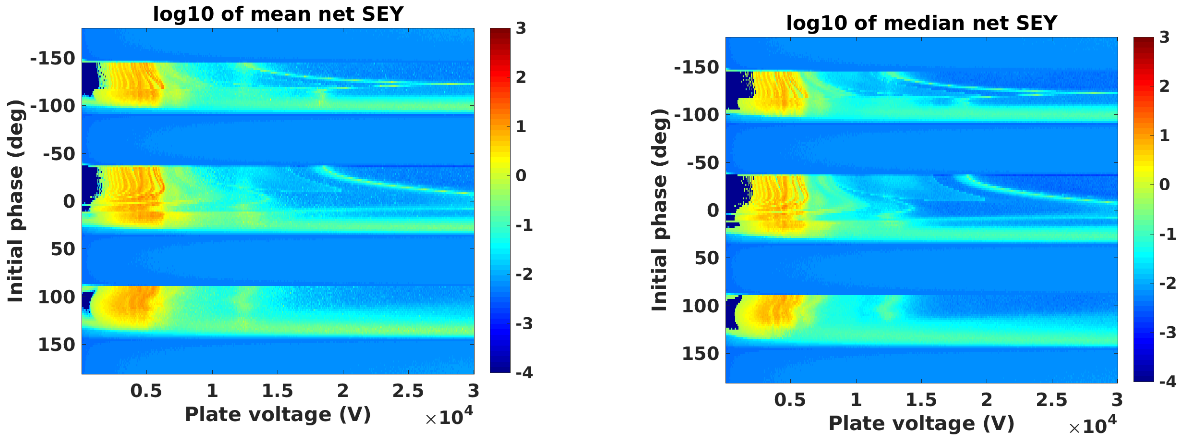

Figure 61: Net SEY as computed from 100 Monte Carlo trials using Furman's SEE model on cavity #2 with both TEM1 and TEM3 modes present. Shown are mean (left) and median (right).

The RMSE for the reduced-order Furman model net SEY is shown in Figure 62 for all four test cases. The error performance is not uniformly better or worse as the cumulative probability parameter of the reduced-order Furman model is changed, but it appears that choosing a cumulative probability in the range of approximately 0.2 to 0.4 will yield the best performance on average.

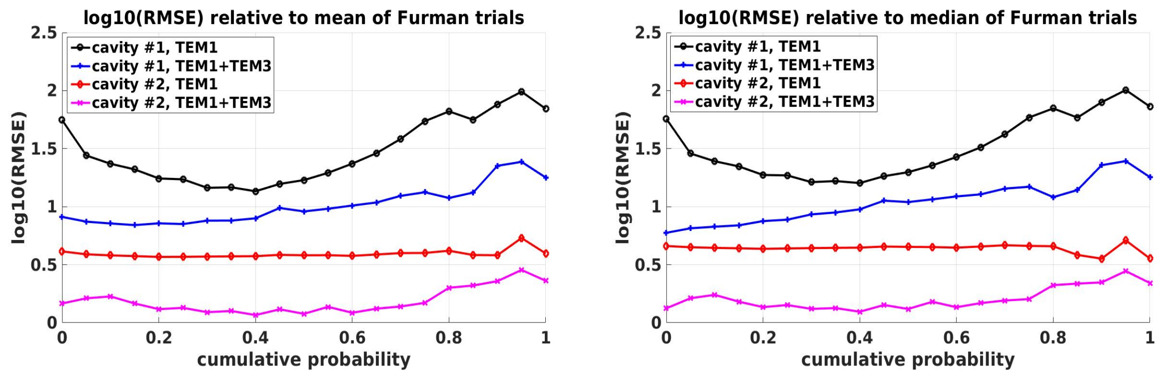

Figure 62: Net SEY RMSE for cavities #1 and #2, showing results with only a TEM1 mode present, and results with both a TEM1 and TEM3 mode present. RMSE is computed against the mean of 100 Furman trials on the left, and against the median of 100 Furman trials on the right.

The RMSE for the reduced-order Furman model geometric averaged SEY is shown in Figure 63 for all four test cases. The error performance for all cases shows nearly equal performance for a cumulative probability parameter of the reduced-order Furman model in the range of approximately 0.2 to 0.7, as compared to cumulative probabilities outside of this intermediate range. A shallow error minimum is observed in the vicinity of a cumulative probability of 0.3.

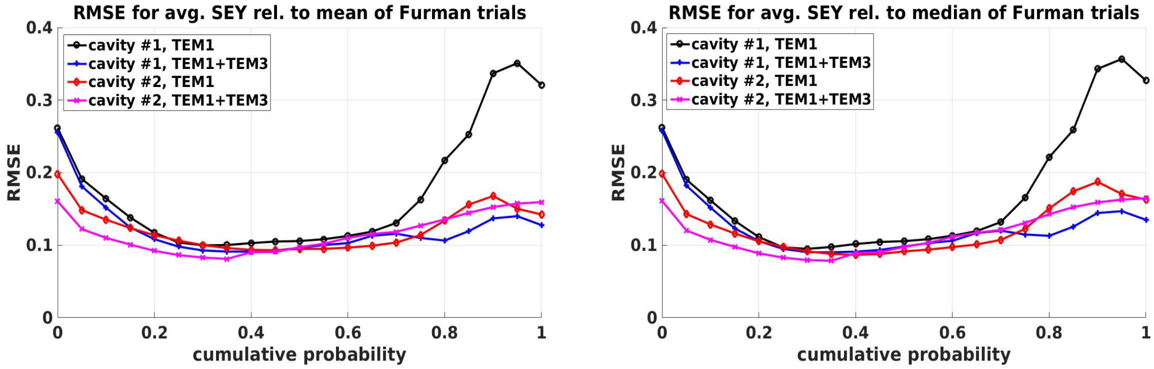

Figure 63: Geometric averaged SEY RMSE for cavities #1 and #2, showing results with only a TEM1 mode present, and results with both a TEM1 and TEM3 mode present. RMSE is computed against the mean of 100 Furman trials on the left, and against the median of 100 Furman trials on the right.

We next consider the GDE for the reduced-order Furman model, which is shown in Figure 64 for all four test cases. The error performance for each individual case shows a minimum at some place between 0.25 and 0.7, depending on the specific case considered and whether we are comparing the mean or median of the Monte Carlo results of the full Furman model. A cumulative probability parameter of the reduced-order Furman model in the range of approximately 0.4 to 0.6 is a good choice to achieve respectable results for all the cases, even though some specific cases may have a lower GDE at a different cumulative probability parameter.

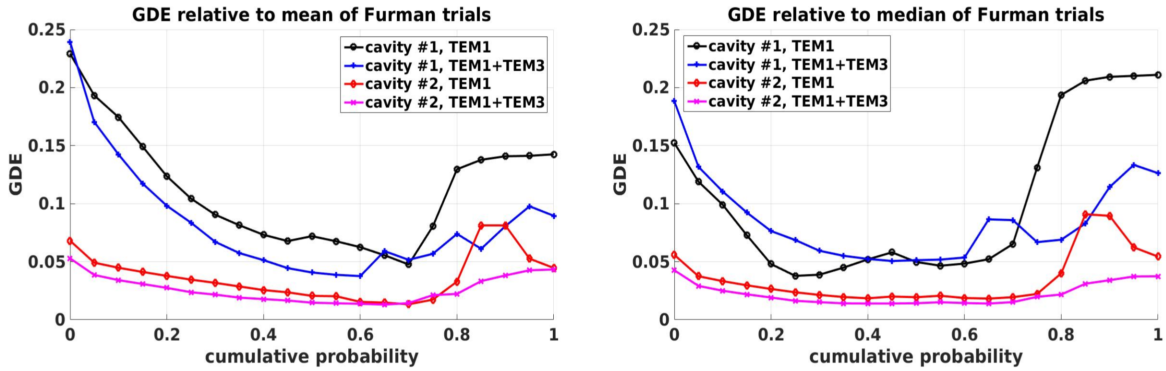

Figure 64: GDE for cavities #1 and #2, showing results with only a TEM1 mode present, and results with both a TEM1 and TEM3 mode present. GDE is computed against the mean of 100 Furman trials on the left, and against the median of 100 Furman trials on the right.

Based upon the error performance shown above, we can provide a few key guidelines for the use of reduced-order Furman models. For a general guideline, a suitable choice for the cumulative probability parameter of the reduced-order Furman model is 0.4. Different error minima may be achieved for specific cases, but a value of 0.4 does a good job of balancing all the errors across all of the test cases examined. If we are particularly interested in accurately characterizing the geometric averaged SEY for a system, then a cumulative probability parameters of 0.3 is probably more suitable, based upon the minimum error locations in Figure 63. Likewise, if we are particularly interested in simply knowing whether or not multipactor will occur as measured by the GDE, then a cumulative probability parameter of 0.6 is probably more suitable, based upon the minimum error locations in Figure 64.

5.4 Conclusions

In this chapter we generalized Furman's medianized SEE model to what we call Furman's reduced-order SEE model, in which the stochastic emission velocity is replaced by a cumulative statistic of the underlying distribution. The medianized Furman SEE model is a special case of this family of reduced-order models, with the cumulative probability chosen to be 0.5. In order to compare the reduced-order Furman SEE model performance against the fully stochastic Furman SEE model, three different error metrics were introduced, which may be of greater or lesser interest for a particular application. In the absence of any particular application dictating which error metric to minimize, a favorable choice for the cumulative probability parameter of the reduced-order Furman model was noted to be 0.4 in the geometries examined.

CHAPTER 6: Controlling multipactor impact points using a higher-order mode

This chapter builds upon the work presented by the author in [48].

6.1 Introduction

The ability to control the specific impact points of multipacting electrons within a structure may be of interest to RF system operators. This capability could be employed for such tasks as cleaning a given location in a structure to reduce further susceptibility to multipactor, or for directing multipacting electrons to a specific location in the geometry which is more or less susceptible to sustaining multipactor, depending on the desired objective.

This chapter examines how multipactor impact points change when a perturbative harmonic mode is added to the fundamental mode which is primarily driving the multipactor. for most of this chapter we depart from the coaxial geometry and use a parallel plate geometry for conceptual simplicity, but the results are expected to be generalizable to coaxial and more complicated geometries. Some comparisons between results for parallel plate and coaxial geometries are presented in Section 6.5.

6.2 Simulation scenario

Consider a parallel plate geometry as shown in Figure 65, which is bounded in the x-dimension and infinite in the *y*- and *z*-dimensions. Within this geometry, we apply time-harmonic fundamental and harmonic electric and magnetic fields as follows:

$$E_x = E_0 \cdot \cos(\omega t + \theta) + \beta \cdot E_0 \cdot \cos(n \cdot (\omega t + \theta) + \zeta) \tag{6.1}$$

$$B_y = (\alpha_1 \cdot E_0 / c) \cdot \sin(\omega t + \theta) + (\alpha_n \cdot \beta \cdot E_0 / c) \cdot \sin(n \cdot (\omega t + \theta) + \zeta) \tag{6.2}$$

(These field phases represent standing waves along the z-direction.)

where E_0 is the peak electric field strength (V/m), ω is the radian frequency (rad/s), t is the time (s), θ is the field starting phase (rad), β is the field strength of the harmonic mode relative to the fundamental mode (unitless), n is an integer greater than one which specifies the harmonic number, ζ is the relative phase of the harmonic mode (rad), α_1 and α_n are unitless scaling parameters which respectively scale the magnetic fields in the fundamental and n^{th} harmonic modes, and c is the speed of light in free space (m/s). The α_1 and α_n parameters allow us to examine what happens when the ratios of electric to magnetic field strengths change, as can occur if standing waves are present in geometries that are bounded in the z-direction in addition to the x-direction, as shown in Figure 66.

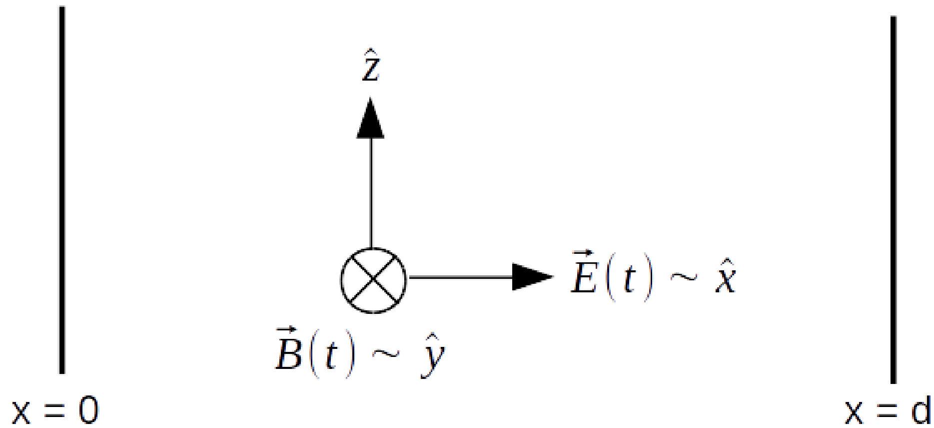

Figure 65: Parallel plate Geometry

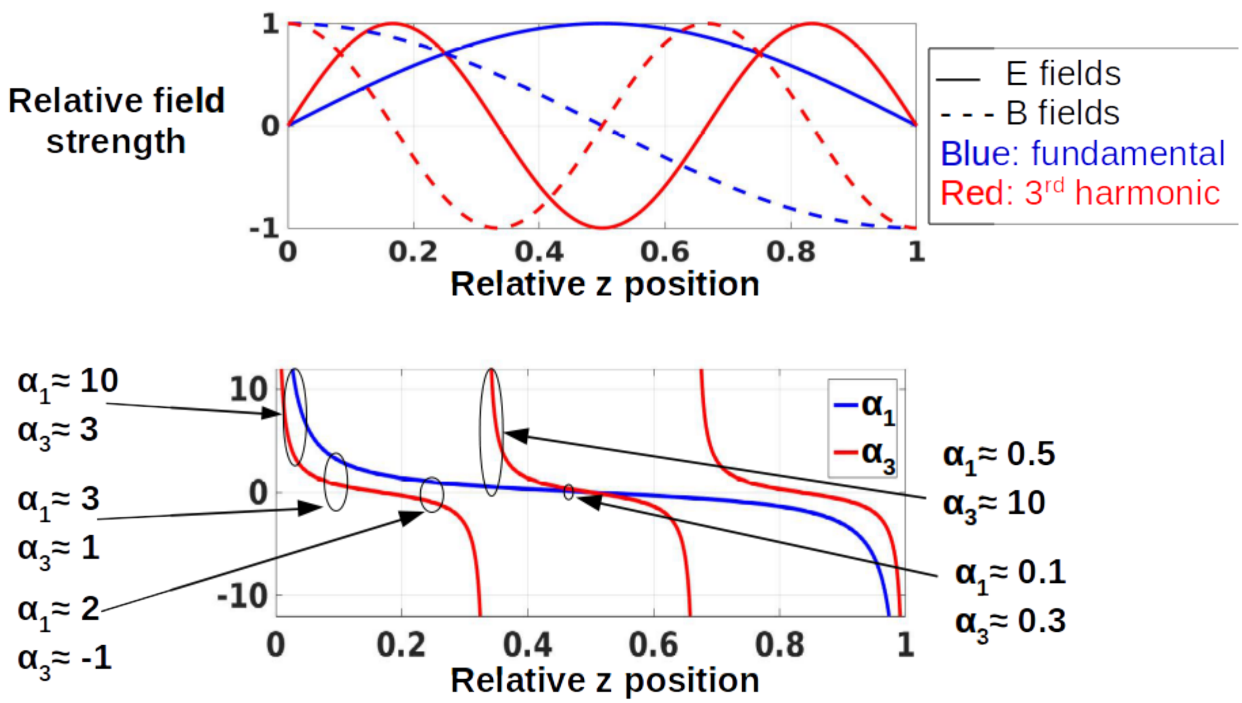

Figure 66: Field profiles for standing waves. Example field magnitudes (top) and field ratios (bottom) for standing waves within a geometry that is electrically shorted at both z boundaries.

In addition to standing waves inside a geometry bounded in z, we are also interested in examining the case of fields being represented by travelling waves in a geometry unbounded in z. For such a field structure, the time quadrature of the magnetic field matches that of the electric field:

$$E_x = E_0 \cdot \cos(\omega t + \theta) + \beta \cdot E_0 \cdot \cos(n \cdot (\omega t + \theta) + \zeta) \tag{6.3}$$

$$B_y = (\alpha_1 \cdot E_0 / c) \cdot \cos(\omega t + \theta) + (\alpha_n \cdot \beta \cdot E_0 / c) \cdot \cos(n \cdot (\omega t + \theta) + \zeta) \tag{6.4}$$

(These field phases represent travelling waves along the z-direction.)

Note that for travelling waves in vacuum, the characteristic impedance of free space would dictate the ratio of the electric to magnetic fields, and thus α_1 and α_n would both be unity. However, in the analysis that follows, we allow for non-unity α_1 and α_n to evaluate the sensitivity of solutions, and to provide some insight into potential results when the fields are a combination of both travelling and standing waves, such as could occur in a waveguide coupling energy into another device, in which some energy is transmitted and some is reflected.

For all the results in this chapter, we used a gap distance of d=4.6472 cm, and a fundamental mode frequency of ω=2π(80.5 MHz). These specific numerical values are somewhat arbitrary; the frequency was chosen to match the quarter-wave resonant cavities being designed for the Facility for Rare Isotope Beams particle accelerator facility [42], and the choice of gap distance was chosen to yield a strong multipactor response for a peak plate-to-plate potential around $E_0 \cdot d \approx$1000V. The qualitative results are expected to generalize to other multipacting systems.

By assuming that we are in the early-time of multipactor before space charge is significant, the multipactor is simulated by starting a particle with zero velocity from $(x,y,z) = (0,0,0)$, and tracking the single particle's trajectory for a default time of 30 periods of the fundamental mode using the numerical differential equation solver as described in Section 2.3. If during this simulation period a boundary strike occurs at $x=0$ or $x=d$, then the (incident energy- and angle-dependent) secondary electron yield (SEY) is computed using Furman's medianized SEE model introduced in Chapter 3. This deterministic secondary electron yield model was chosen in order to keep this investigation computationally feasible.

For every computed trajectory, the net SEY is computed as the product of all the SEY values of the individual impacts. A somewhat arbitrary threshold of 0.001 was defined such that if the net SEY is below this threshold, then the trajectory is discarded, and the corresponding parameters are considered to not support multipactor. Otherwise the trajectory is retained as a possible trajectory of particles supporting multipactor. In testing to evaluate the sensitivity of the later results to the net SEY threshold, thresholds of 0.01 and 0.0001 were also examined for two test cases, and no significant changes in the results were noted; the results of this test with different thresholds are provided in the Appendix of this dissertation.

6.3 Control of *z*-drift

The multipacting particles are subject to two forces: electric forces which accelerate the particles along the electric fields, and magnetic forces which accelerate the particles transverse to the magnetic fields. In the parallel plate geometry under consideration, this transverse drift would manifest as a deflection in the positive or negative z-direction. Since particle trajectories can drift, an interesting question is whether we can control this drift through an appropriate choice of the magnitude and phase of the two modes present. We are particularly interested in controlling multipactor *z*-drift via the higher-order mode when given the field parameters of the fundamental mode, because in many practical situations the fundamental mode conditions are pre-defined design or operational conditions in a system.

We begin to answer the above question by noting that for a given fundamental mode specified by (ω, E_0, θ, α_1), if we introduce a higher-order mode specified by parameters (n, β, ζ, α_n), then we can change the resulting particle trajectory migrations along z: we can increase the migration rate, decrease the migration rate, and in some circumstances even change the direction of migration.

We can demonstrate this change in *z*-migration through a representative example: Using the default frequency ω and gap distance d given in Section 6.2, and for the travelling wave field configuration as defined in equations (6.3) and (6.4), let us specify a fundamental mode field configuration by setting $E_0 \cdot d$=1000V (or equivalently, E_0=21.52 kV/m), α_1=1, and three different cases for the field phases θ={0, -π/9, π/9}. For an example additive harmonic mode excitation, we set n=3, β=0.8, α_3=-10, and allow ζ to range around the unit circle in 30 equally spaced samples starting at ζ=0; ζ is allowed to independently change for each field phase φ examined. For all of these cases we then calculate the *z* drifts vs. time over 30 periods of the fundamental mode, and we record the maximum and minimum possible *z* drifts obtained as we varied ζ. The results are shown in Figure 67 below.

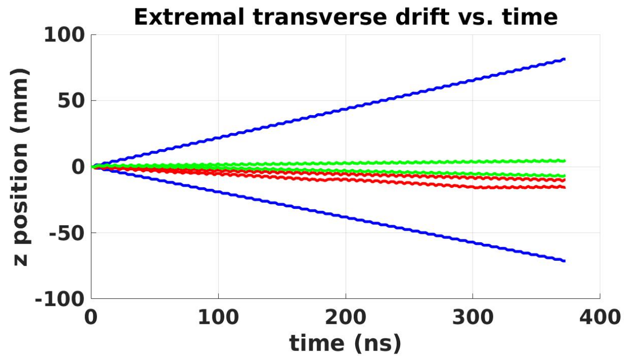

Figure 67: Extremal transverse (z) drift trajectories vs. time. Plots are shown for $\theta = 0$ (blue), $\theta = -\pi/9$ (red), and $\theta = \pi/9$ (green). Field parameters are defined in the preceding text. Two trajectories are shown for each phase: the minimum and maximum achieved transverse drift as ζ is allowed to independently vary for each phase φ, as explained in text.

We note that in Figure 67, for the cases of the fundamental mode phase θ being 0 or $\pi/9$, we are able to cause the z drift to be either positive or negative by an appropriate choice of ζ. When this is possible, we refer to a given multipactor condition as being steerable-to-zero. In general, this is not always possible, and we are interested in understanding when it is possible.

In order to determine which multipacting field configurations allow for steerability-to-zero along the transverse drift direction, we must first specify the field parameters ($\omega, E_0, \theta, \alpha_1, n, \alpha_n$). Note that in most multipacting circumstances, we are significantly limited in our ability to change these parameters: ω and E_0 are operating constraints for a given system, θ is the field phase when a random multipacting trajectory is initiated, and the magnetic-to-electric field scaling factors α_1 and α_n are dependent upon the specific mode and system geometry. If we wish to control the z-migration, we thus in practice would have control only over the higher order mode number n, relative strength β, and relative phase ζ.

For the default ω and gap distance d given in Section 6.2, we search over the following ranges of parameters: $E_0 \cdot d$={700, 800, 900, 1000, 1100, 1200, 1300, 1400} V, φ={-π to π radians in 60 equally-spaced samples}, α_1={.1, .316, 1, 3.16, 10}, n={2,3,4}, α_n=±{.1, .316, 1, 3.16, 10}, ζ={0 to 2π in 30 equally-spaced samples}, and β={0.01 to 2 in 41 logarithmically-spaced samples}. Note that even though we need both positive and negative values for α_n, we only need to include positive α_1 values because a steerable-to-zero condition for a negative α_1 value would also yield a steerable-to-zero condition if we make the following parameter changes: $\alpha_1 \rightarrow -\alpha_1$, $\alpha_n \rightarrow -\alpha_n$. Thus, without loss of generality we can reduce our search space by considering only positive α_1 values.

For each ($\omega, E_0, \theta, \alpha_1, n, \alpha_n$) parameter value permutation, we step through β in order of increasing value, simulate multipactor trajectories for each possible ζ value, and search for two conditions: (i) Does at least one of the ζ samples yield a positive z-deflection at the end of the simulation interval? (ii) Does at least one of the ζ samples yield a negative z-deflection at the end of the simulation interval? Once both of these conditions have been satisfied for a value of β equal to or less than the present selected β, we declare that the multipactor z-deflection is steerable-to-zero for the given ($\omega, E_0, \theta, \alpha_1, n, \alpha_n$) parameter value permutation. Note that the above conditions (i) and (ii) need not be satisfied by the same value of β; for example a value of $\beta^{(+)}$ may be needed to effect a positive z-deflection, and a value of $\beta^{(-)}$ may be needed to effect a negative z-deflection. In such a case, we record β to be the larger of $\beta^{(+)}$ and $\beta^{(-)}$, such that positive and negative z-deflection can be achieved at or below the reported β value. This definition of steerability-to-zero would translate into a laboratory RF source in which we could independently control the magnitude and phase of the higher-order mode.

For each (α_1, α_n) combination, we tabulate the minimum β needed that can allow for a steerable-to-zero condition, as a function of plate peak voltage ($E_0 \cdot d$) and field starting phase φ. Figure 68 shows such a surface for the parameter choices α_1 = 0.1 and α_3 = 10, and for the travelling wave field configuration as defined in equations (6.3) and (6.4).

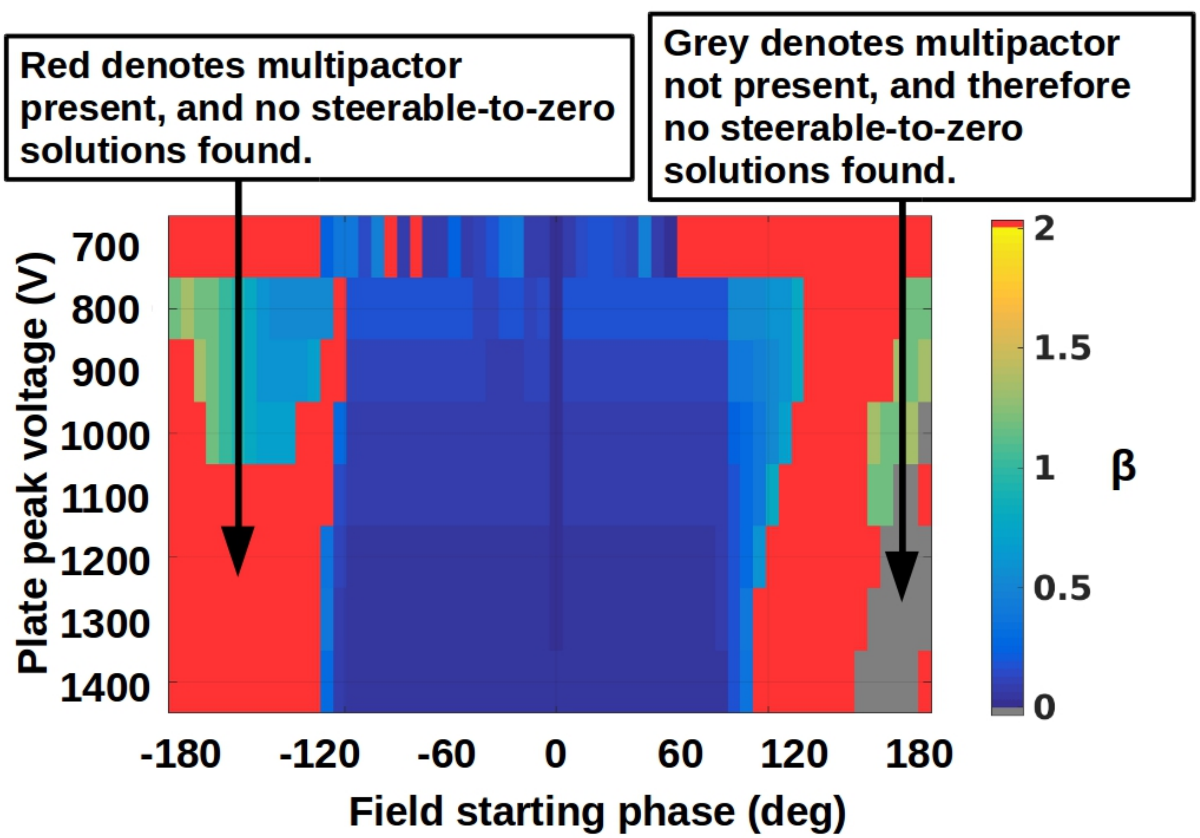

Figure 68: Surface plot showing regions of multipactor steerability-to-zero for travelling waves with α_1 = 0.1 and α_3 = 10. The same axes and colormap ranges are used for all surface plots.

6.4 Controllability results

Figures 69, 70, and 71 respectively show for standing waves the minimum-β surfaces for multipactor steerability-to-zero via the presence of a 2nd, 3rd, or 4th harmonic mode, in addition to the fundamental mode; Figures 72, 73, and 74 respectively show the same cases for travelling waves. Some general conclusions can be drawn from an examination of these results.

The first general conclusion that we notice is that to a good approximation it is only the ratio of magnetic field strengths α_n/α_1 which determines the steerability-to-zero surfaces. This is evident when steerability-to-zero surfaces are compared along diagonals from the upper-left to the lower-right in Figures 69 through 74, and show remarkable similarity with diagonally-adjacent results. This is explained by noting that the z-deflection due to a given mode is proportional to magnetic field strength of that mode, and thus if two opposing magnetic fields are present and are both scaled by the same factor, then the net deflection direction experienced by a particle will be the same.

The second general trend that we notice is that steerability-to-zero is more common with the standing wave modes than with the travelling wave modes. This is due to the relative phase (sine vs. cosine) of the magnetic fields for the same electric fields, as noticed by examining equations (6.1) through (6.4). If we consider the electric field as primarily driving the multipactor along the $\pm x$-direction in Figure 6.1, and the magnetic fields as primarily steering the multipactor along the $\pm z$-direction in Figure 6.1, then we notice that with standing waves, the magnetic field direction changes sign halfway through the time that the electric field is accelerating a particle in a single direction. We also recall that due to phase-locking for multipactor resonance to occur, the electric field tends to change direction near the time that particles impact the far boundary. Thus, if we consider a particle travelling from one boundary to the other in one-half period of the driving frequency (ie. N=1 in equation (3.1)), then the magnetic field introduces less deflection if it changes direction approximately halfway through the transit (the standing wave case), than it does if it points in the same direction over most of the transit (the travelling wave case). Thus, if the fundamental mode is a travelling wave, then the field is already deflecting the particles more significantly than if the fundamental mode is a standing wave. This is the baseline condition for the trajectories before introducing perturbing modes, and thus it is intrinsically harder to control the z-drift in the travelling mode case, in which the particles already have a more significant z-drift.

We observe that for both standing wave and travelling wave results, the 4th harmonic perturbation tends to do worse than the 2nd or 3rd harmonic perturbation. We also note that for standing waves, the 3rd harmonic perturbation results in the greatest steerable-to-zero areas in the parameter spaces examined; for travelling waves, the 2nd harmonic perturbation results in the greatest steerable-to-zero areas in the parameter spaces examined.

In the travelling wave case, for all of the harmonics examined, with a few exceptions to be discussed momentarily, steerability-to-zero is most achievable in regions with a relatively weak fundamental mode B-field (small α_1) and a relatively strong harmonic mode B-field (large $|\alpha_2|$, $|\alpha_3|$, and $|\alpha_4|$). This is understandable by considering two opposing factors. The first factor is that the fundamental mode B-field tends to result in the particles migrating in the z-direction, transverse to both the x-velocity and the B-field. The x-velocity and the B-field tend to change signs at approximately the same time due to period-locking of the multipactor to the driving fields; this results in a net deflection along the same direction during each half of the multipactor period. The second factor is that the stronger the harmonic mode, the more this mode's B-field is able to affect the particle's z-deflection, and thus counteract the intrinsic deflection due to the presence of the fundamental mode. The combination of these two opposing factors results in a weak fundamental mode B-field and a strong harmonic mode B-field being conducive to steering the z-deflection.

The possible exception in the travelling wave case to this general trend of steerability-to-zero being linked with strong harmonic fields is observed for the case of the 2nd harmonic and $\alpha_2 < 0$, in which the largest regions of steerability are observed when the magnetic fields of the fundamental and harmonic mode are approximately equal, which corresponds to the surface plots along the main diagonal in the bottom pane of Figure 72. However, these increased regions of steerability are achieved at a tradeoff, in that they require a stronger harmonic mode field strength (higher β value) as compared to the steerable-to-zero conditions involving a small α_1 and large $|\alpha_2|$ in Figure 72.

For the standing wave case, for the 2nd and 3rd harmonic cases, the steerability-to-zero tends to be more possible in regions with a relatively strong fundamental mode B-field (large α_1) and a relatively weak harmonic mode B-field (small $|\alpha_2|$ and $|\alpha_3|$). This weak magnetic field condition for the perturbing mode, opposite to the behavior observed for the travelling wave case, is not yet well-understood and deserves future study beyond the scope of this dissertation, especially in regard to what is the optimal ratio of fundamental-to-harmonic magnetic fields for optimum controllability.

We also observe in the travelling wave case that steerability-to-zero is most achievable for α_n being the opposite sign of α_1. This condition represents a situation in which the harmonic mode's magnetic-to-electric field orientation ($+y$ vs. $-y$ for the B-field when E-field is directed along $+x$) has the opposite parity as the fundamental mode, as can be seen from an examination of Equations (6.3) and (6.4). This effect is not observed in the standing wave case, as expected, because the magnetic-to-electric field orientations change at different times than do the electric fields.

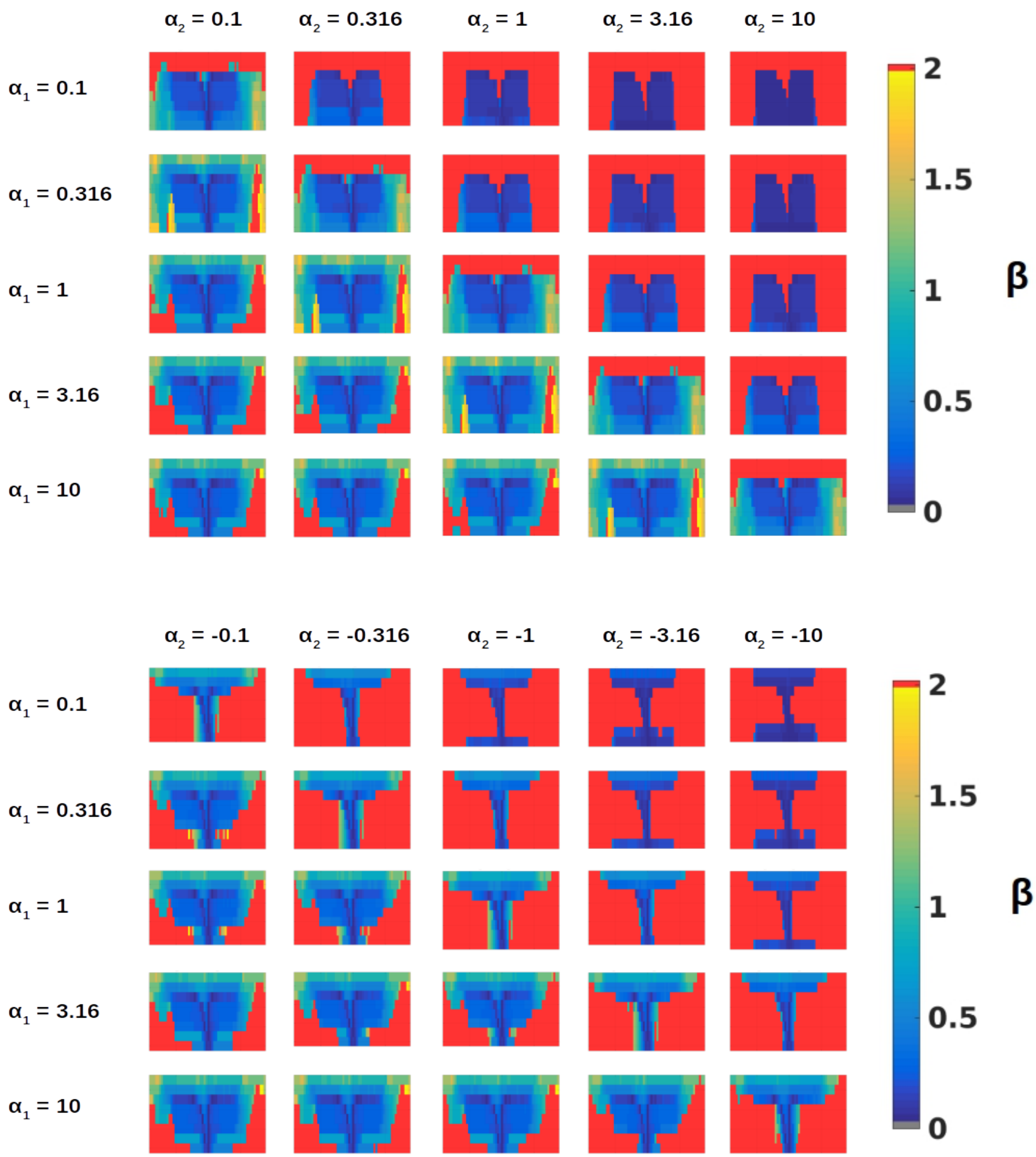

Figure 69: Standing wave steerable-to-zero conditions for 2nd harmonic perturbative mode, for various values of α_1 and α_2. Unlabelled axes are shown as in Figure 68. (top) Results for $\alpha_2 > 0$. (bottom) Results for $\alpha_2 < 0$.

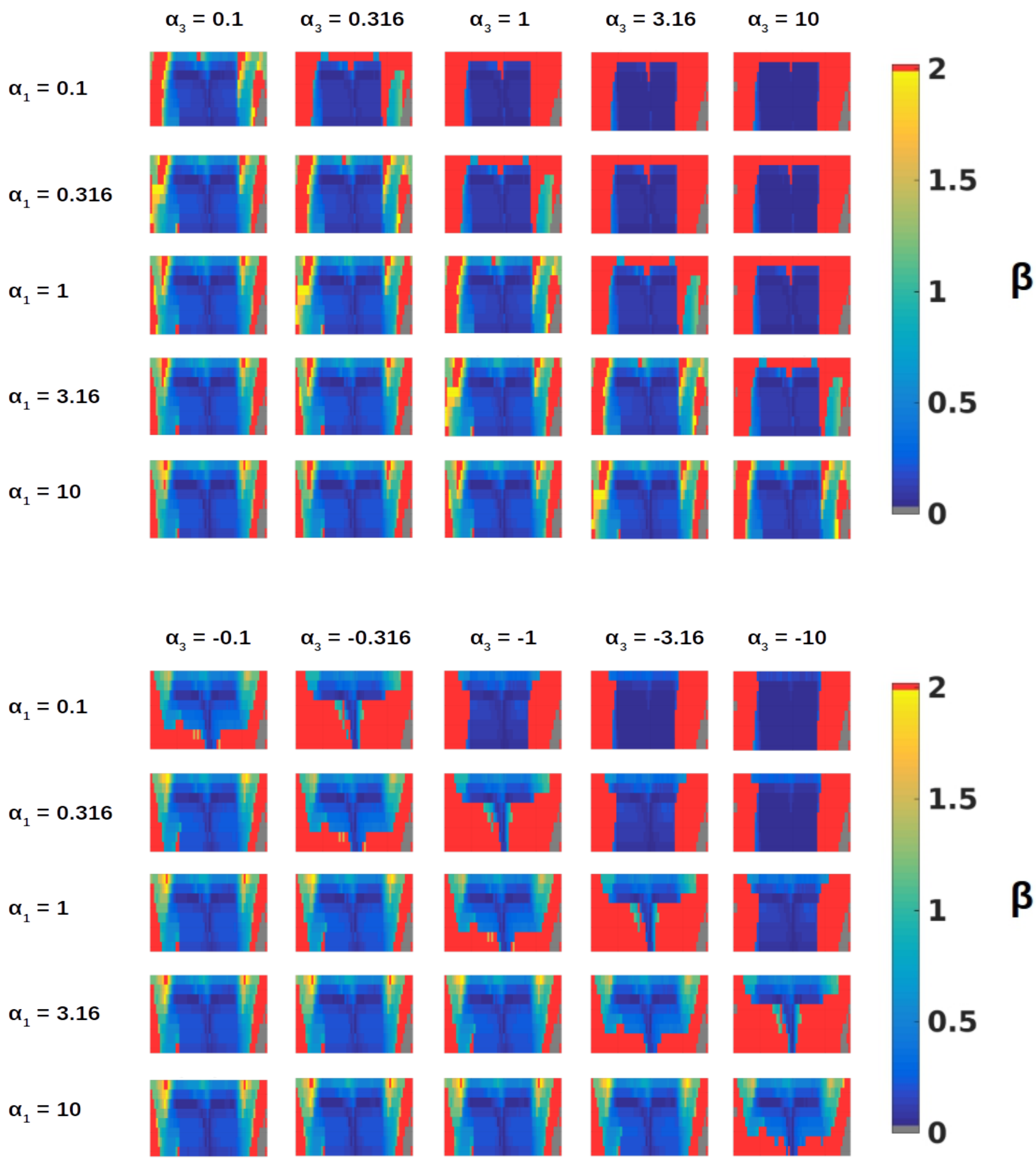

Figure 70: Standing wave steerable-to-zero conditions for 3rd harmonic perturbative mode, for various values of α_1 and α_3. Unlabelled axes are shown as in Figure 68. (top) Results for $\alpha_3 > 0$. (bottom) Results for $\alpha_3 < 0$.

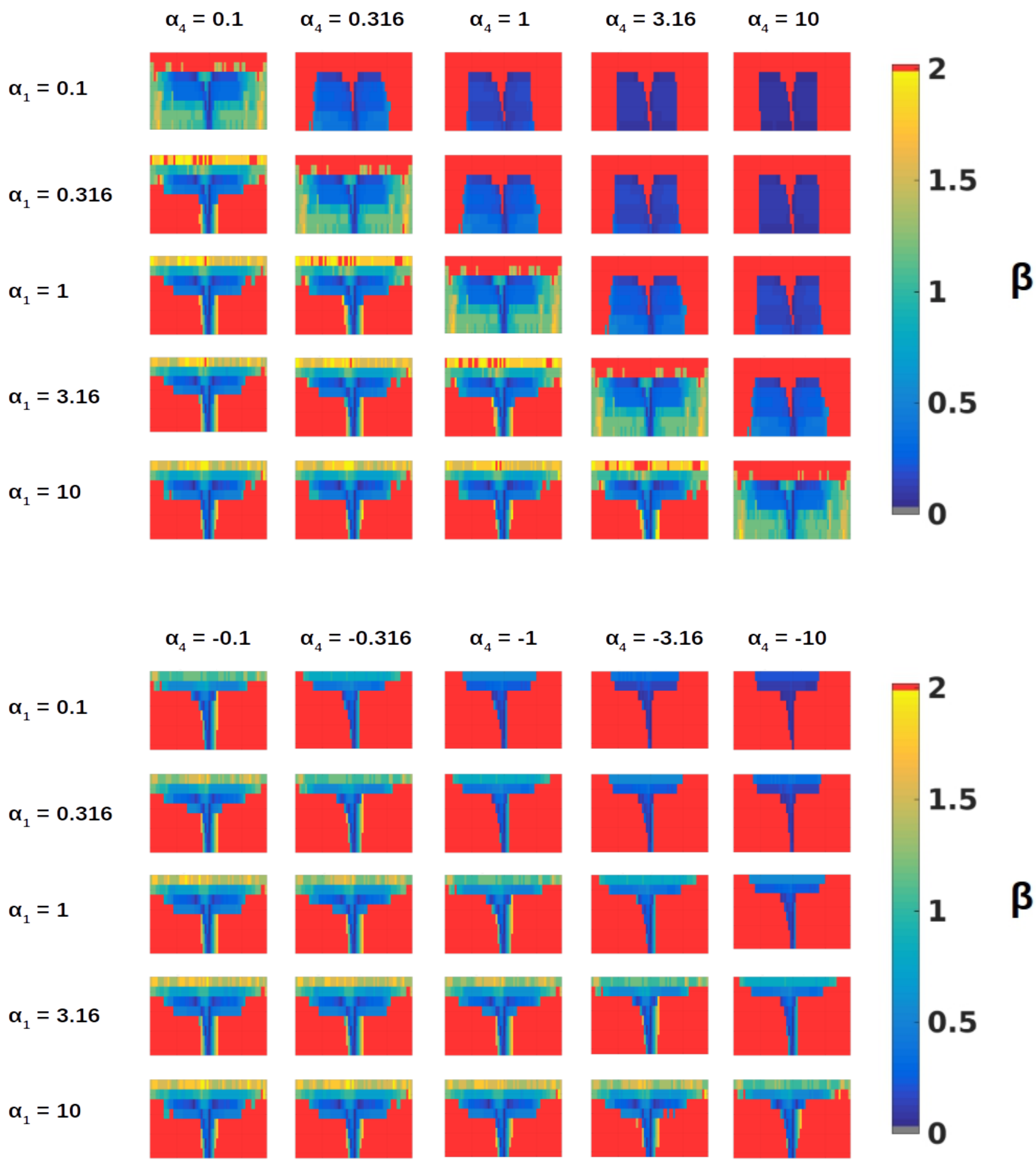

Figure 71: Standing wave steerable-to-zero conditions for 4th harmonic perturbative mode, for various values of α_1 and α_4. Unlabelled axes are shown as in Figure 68. (top) Results for $\alpha_4 > 0$. (bottom) Results for $\alpha_4 < 0$.

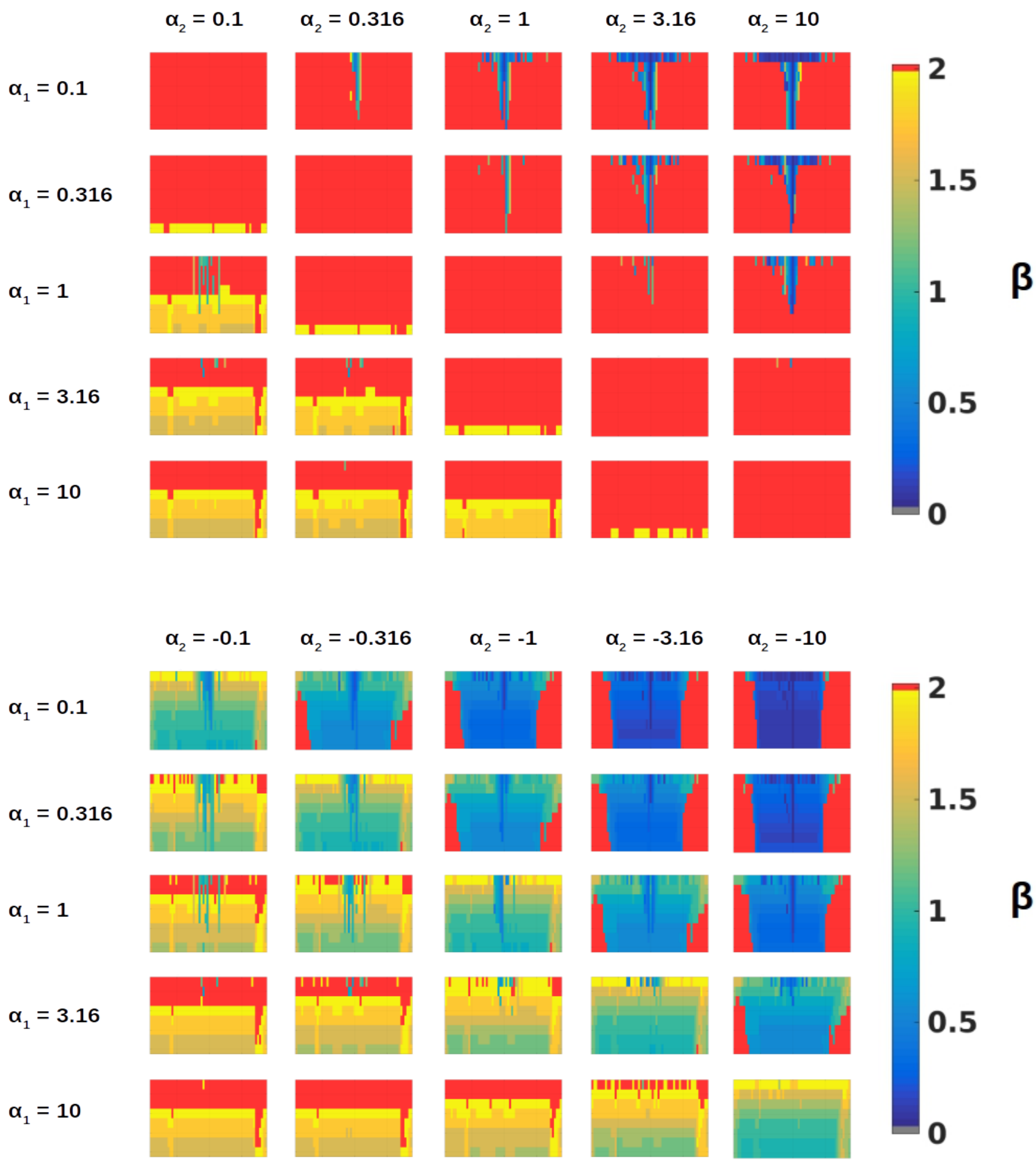

Figure 72: Travelling wave steerable-to-zero conditions for 2nd harmonic perturbative mode, for various values of α_1 and α_2. Unlabelled axes are shown as in Figure 68. (top) Results for $\alpha_2 > 0$. (bottom) Results for $\alpha_2 < 0$.

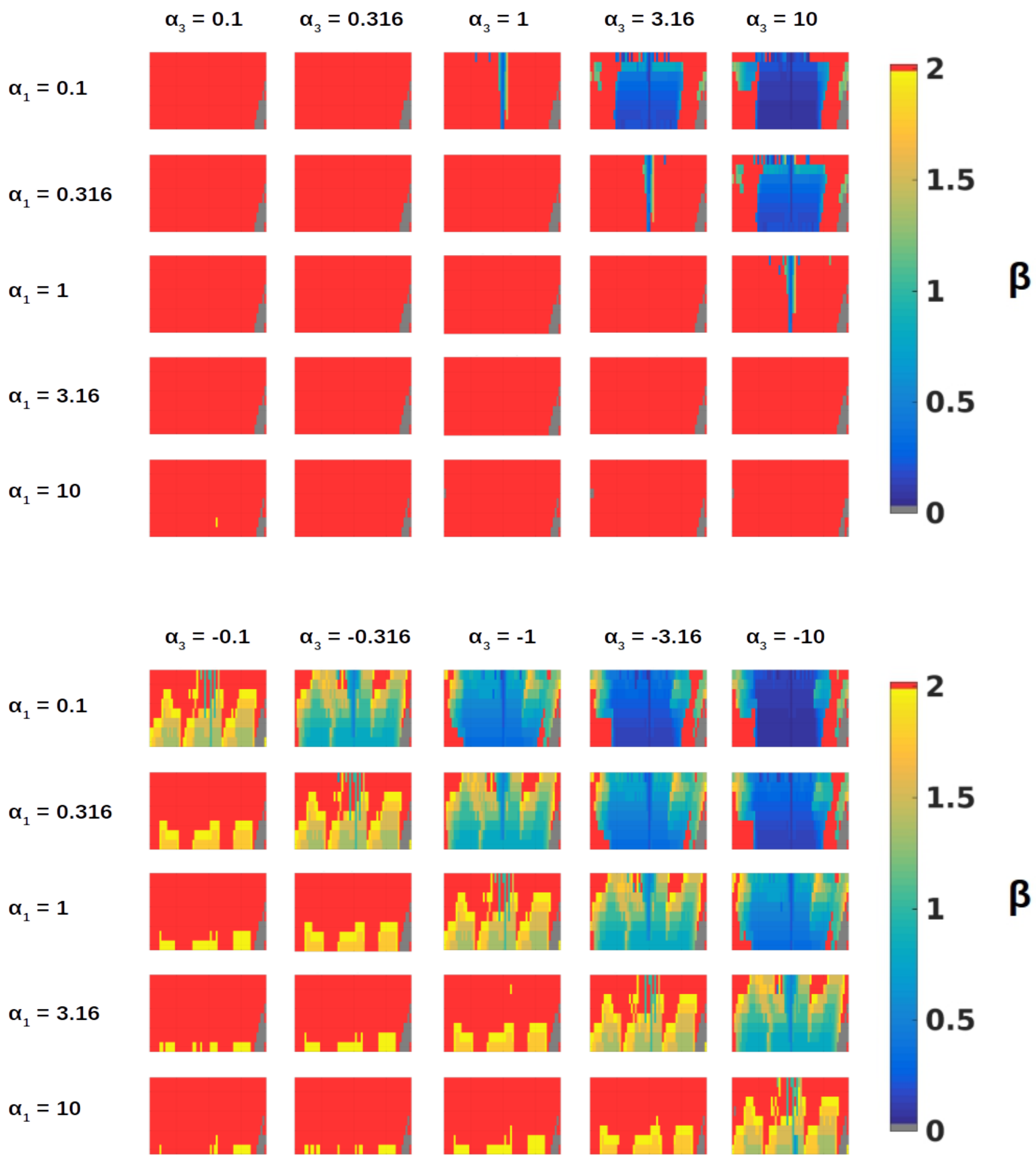

Figure 73: Travelling wave steerable-to-zero conditions for 3rd harmonic perturbative mode, for various values of α_1 and α_3. Unlabelled axes are shown as in Figure 68. (top) Results for $\alpha_3 > 0$. (bottom) Results for $\alpha_3 < 0$.

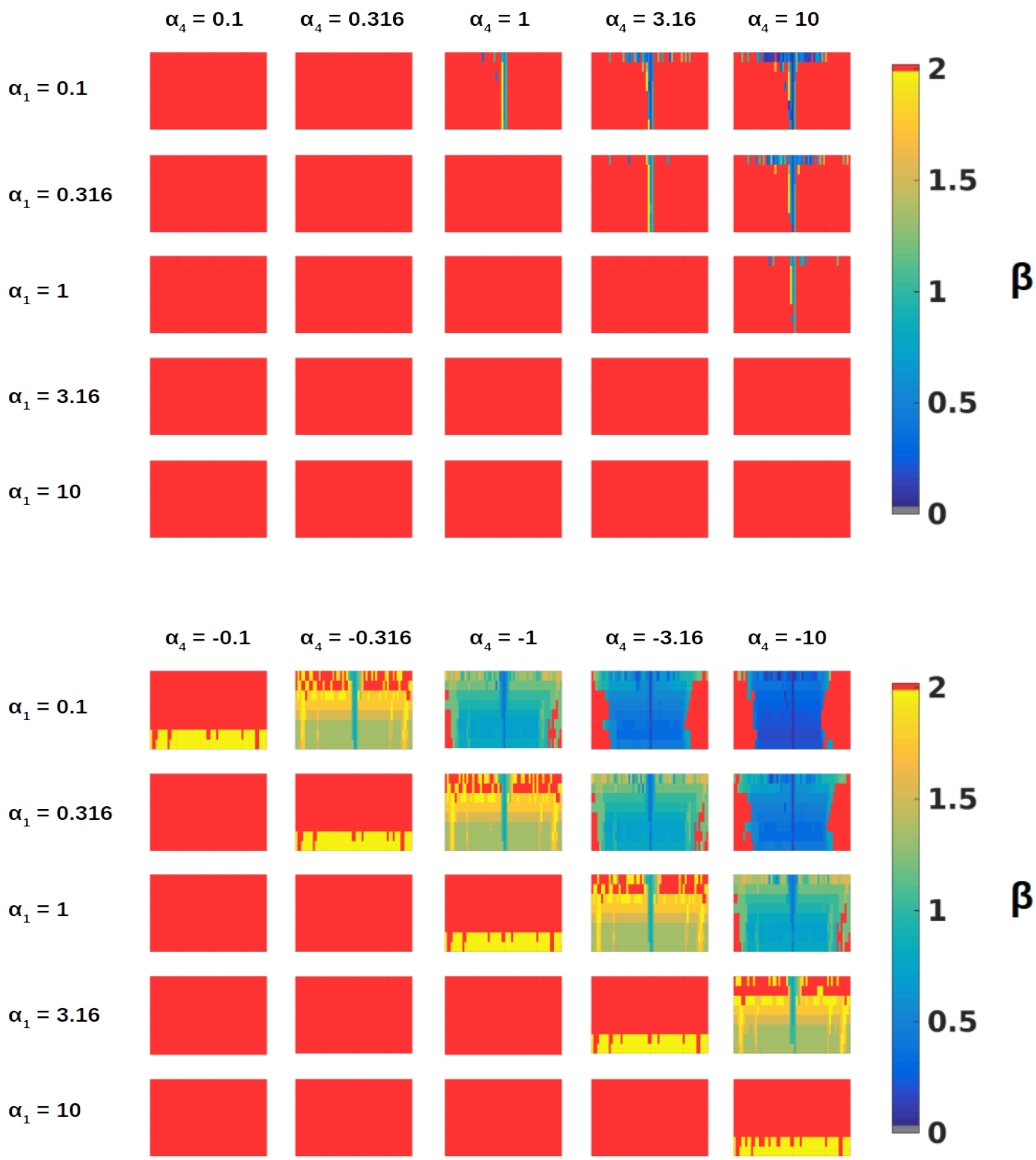

Figure 74: Travelling wave steerable-to-zero conditions for 4th harmonic perturbative mode, for various values of α_1 and α_4. Unlabelled axes are shown as in Figure 68. (top) Results for $\alpha_4 > 0$. (bottom) Results for $\alpha_4 < 0$.

6.5 Comparison to selected coaxial geometries

In this section we examine the present approach to controlling z-drift within coaxial cavities, which have field profiles which vary along the z-direction. We focus our attention on the case of a 3rd harmonic perturbative mode. For ease of reference, we pictorially represent the coaxial cavity (described in Chapter 3) in Figure 75 below, in which the inner and outer conductors are shorted at both ends.

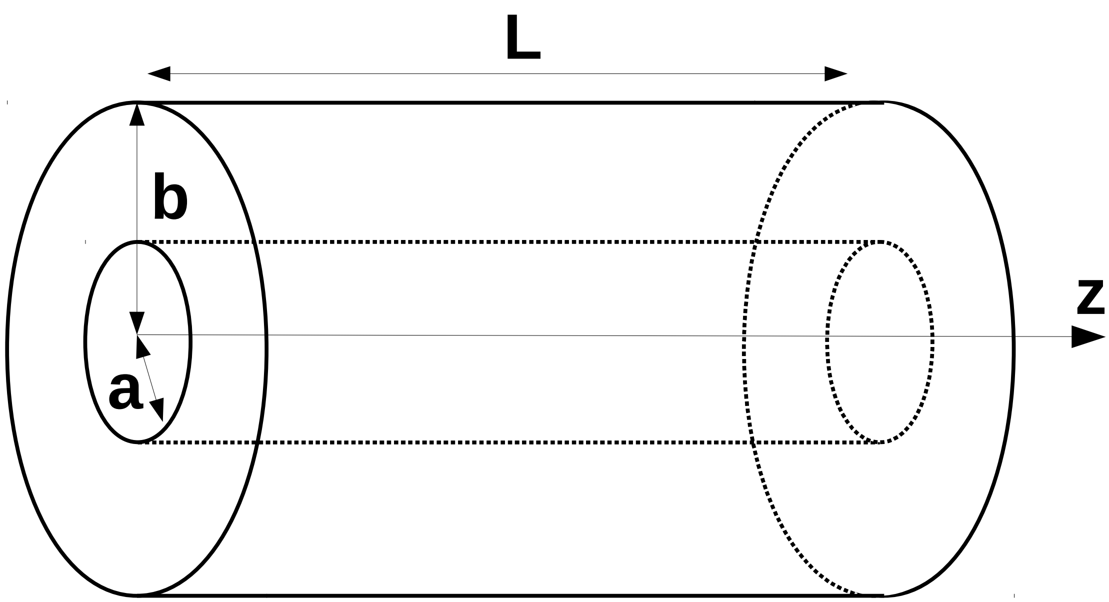

Figure 75: Coaxial cavity geometry. Dimensions are length L, inner radius a, and outer radius b.

As described in Chapter 3, we use a length L=1.86 meters, which corresponds to a fundamental (n=1) TEM mode resonance at 80.5 MHz. We consider three different inner radii: a = {0.01, 0.1, 1} meters. The gap distance b-a = 0.046472 meters for all cases, in order to be consistent with the parallel plate analysis in the previous section.

With perturbing 3rd harmonic TEM mode present, the electric field $\boldsymbol{E}(r,z,t)$ and magnetic field $\boldsymbol{B}(r,z,t)$ field inside the cavity can be expressed as:

$$\boldsymbol{E}=-\hat{r}\frac{V_0}{r\cdot\log(b/a)}\cdot\left(\cos(\omega t+\theta)\cdot\sin\left(\frac{\pi z}{L}\right)+\beta\cdot\cos(3\omega t+3\theta+\xi)\cdot\sin\left(\frac{3\pi z}{L}\right)\right), \tag{6.5}$$

$$\boldsymbol{B}=\hat{\phi}\frac{1}{c}\frac{V_0}{r\cdot\log(b/a)}\cdot\left(\sin(\omega t+\theta)\cdot\cos\left(\frac{\pi z}{L}\right)+\beta\cdot\sin(3\omega t+3\theta+\xi)\cdot\cos\left(\frac{3\pi z}{L}\right)\right), \tag{6.6}$$

where V_0 is the peak conductor-to-conductor voltage, r is the radial location, and all other parameters are as defined in equations 6.1 and 6.2. Note that the fields given by equations (6.5) and (6.6) have a negative sign, as compared to the coaxial fields defined in previous chapters. This was done so that the field phase θ would have the same meaning as for the parallel plate case, to allow for easier comparison to the parallel-plate results.

Since the field profiles change as a function of z-position as previously shown in Figure 66, we choose six starting locations along z as shown in Table 2; recall that z=0 and z=L bound the cavity. Figures 76 through 81 respectively show the results for starting z-positions corresponding to ratios of α_3/α_1 = {1/10, -1/10, -1/3, -3, -10, 10}, for the cavities with the three different inner radii a, as well as the closest parallel plate result for each case. The plot axes in these figures correspond to the same scales as shown in Figure 68. Specifically, the plot x-axes correspond to the electric field starting phase, the plot y-axes correspond to the fundamental mode's peak voltage between the outer and inner conductor at the particle starting z-position (note that the field strengths will be different at other z-positions within the cavity), and the colormap denotes the same scale as in the previous results.

z	α_1	α_3	α_3/α_1
0.14536 L	2.0354	0.2036	1/10
0.18292 L	1.1544	-0.1544	-1/10
0.20978 L	1.2910	-0.4303	-1/3
0.29021 L	0.7746	-2.2325	-3
0.31707 L	0.6476	-2.2325	-10
0.35465 L	0.4913	4.9103	10

Table 2: z-locations within a coaxial cavity to yield desired α_3/α_1 ratios.

The results demonstrate that steerable-to-zero conditions are achievable in this coaxial cavity, in which the fields are changing with z-position. As expected, we also notice that the coaxial results tend towards the parallel plate results as the gap distance becomes small relative to the conductor radii.

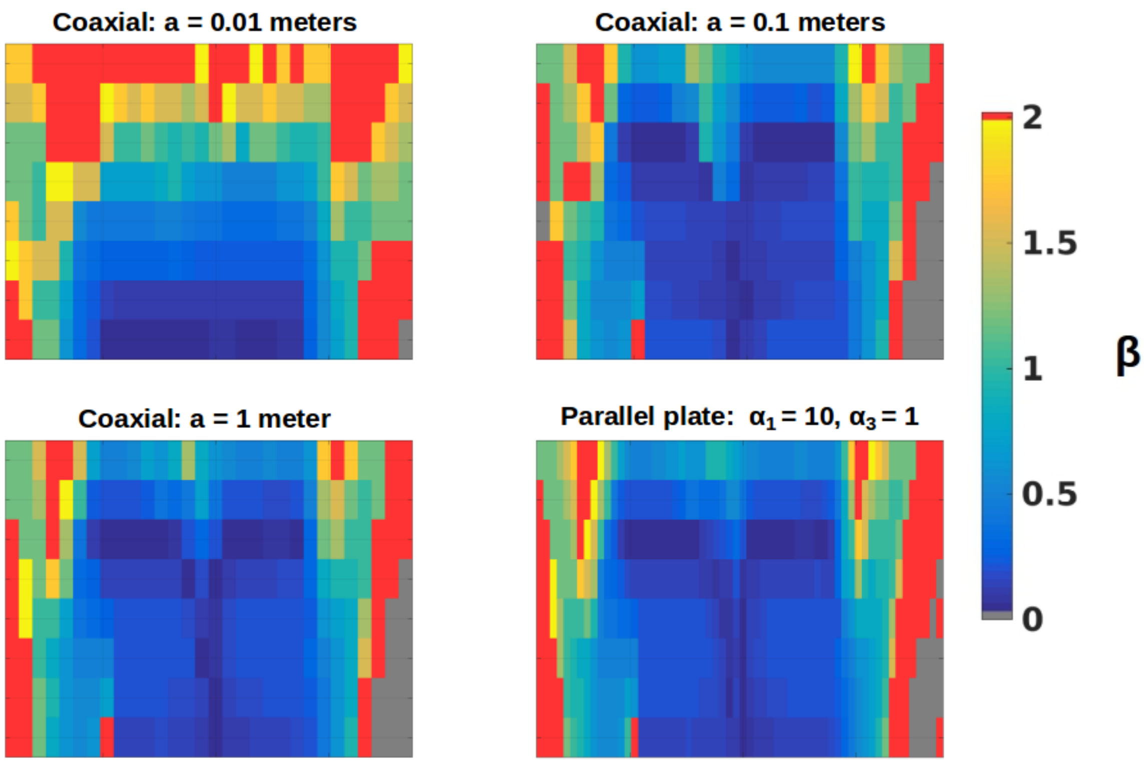

Figure 76: Coaxial cavity steerable-to-zero conditions for a 3rd harmonic perturbative mode, and α_3 / α_1 = 1/10. This corresponds to a starting *z* position of *z*=0.14536L. As the inner radius *a* increases while gap distance remains the same, the results approach the parallel plate standing wave results shown in the lower right pane. Unlabelled axes are as shown in Figure 68.

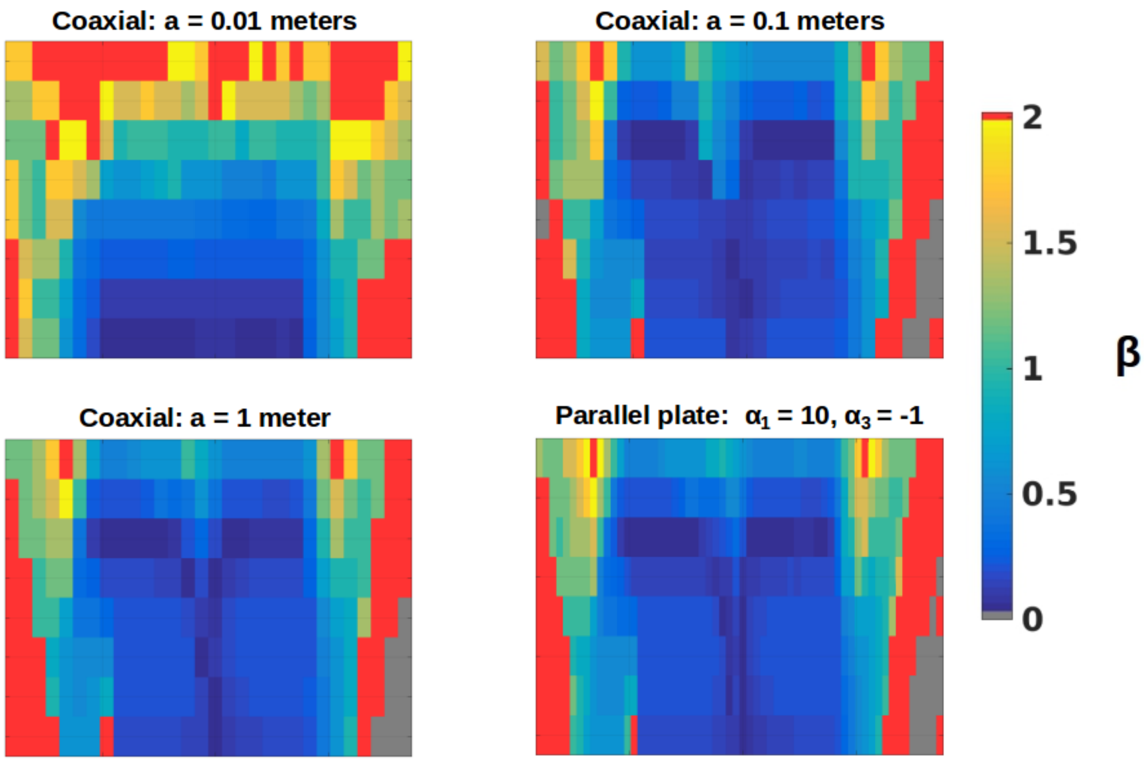

Figure 77: Coaxial cavity steerable-to-zero conditions for a 3rd harmonic perturbative mode, and α_3 / α_1 = -1/10. This corresponds to a starting *z* position of *z*=0.18292L. As the inner radius *a* increases while gap distance remains the same, the results approach the parallel plate standing wave results shown in the lower right pane. Unlabelled axes are as shown in Figure 68.

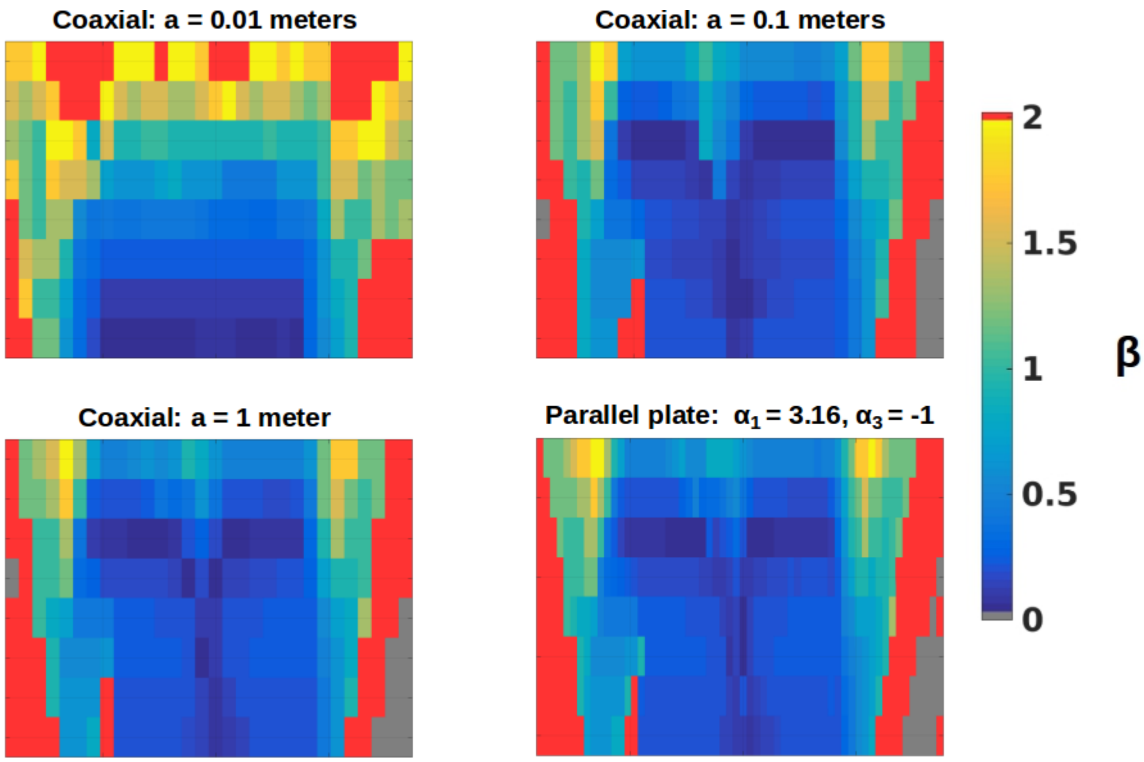

Figure 78: Coaxial cavity steerable-to-zero conditions for a 3rd harmonic perturbative mode, and $\alpha_3/\alpha_1 = -1/3$. This corresponds to a starting z position of z=0.20978L. As the inner radius a increases while gap distance remains the same, the results approximately approach the parallel plate standing wave results shown in the lower right pane, which was generated using a comparable α_3/α_1 ratio of -1/3.16. Unlabelled axes are as shown in Figure 68.

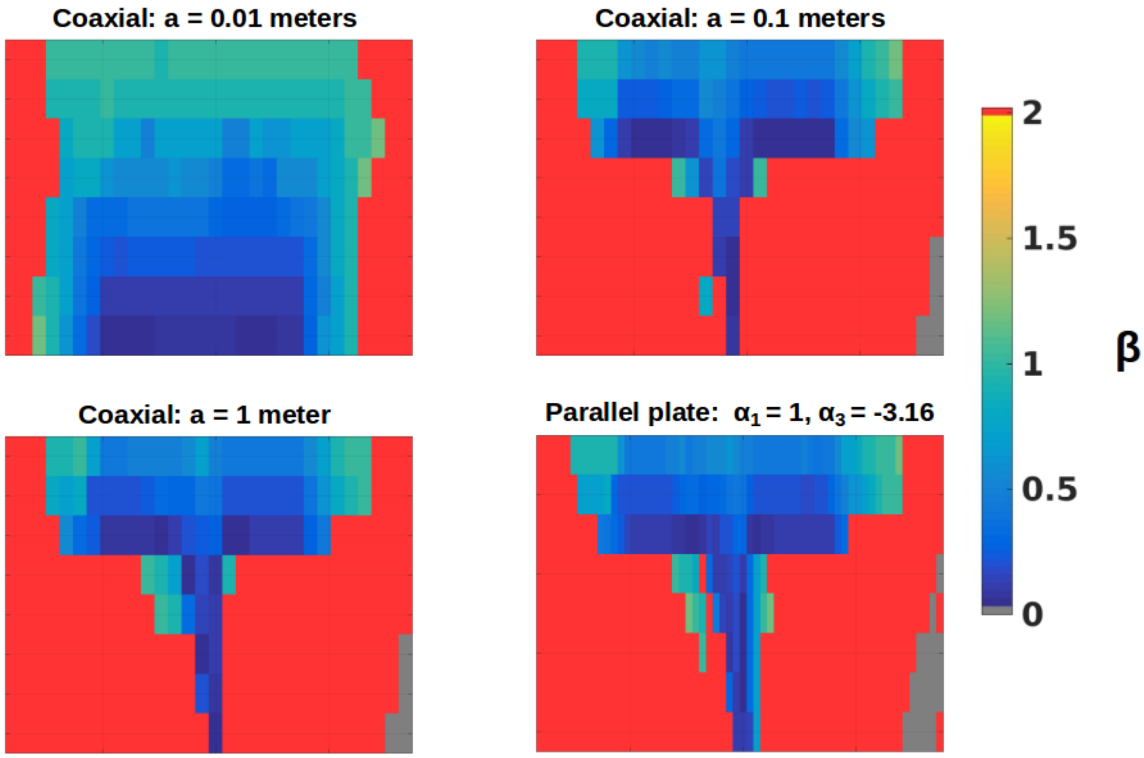

Figure 79: Coaxial cavity steerable-to-zero conditions for a 3rd harmonic perturbative mode, and α_3/α_1 = -3. This corresponds to a starting *z* position of *z*=0.29021L. As the inner radius *a* increases while gap distance remains the same, the results approximately approach the parallel plate standing wave results shown in the lower right pane, which was generated using a comparable α_3/α_1 ratio of -3.16. Unlabelled axes are as shown in Figure 68.

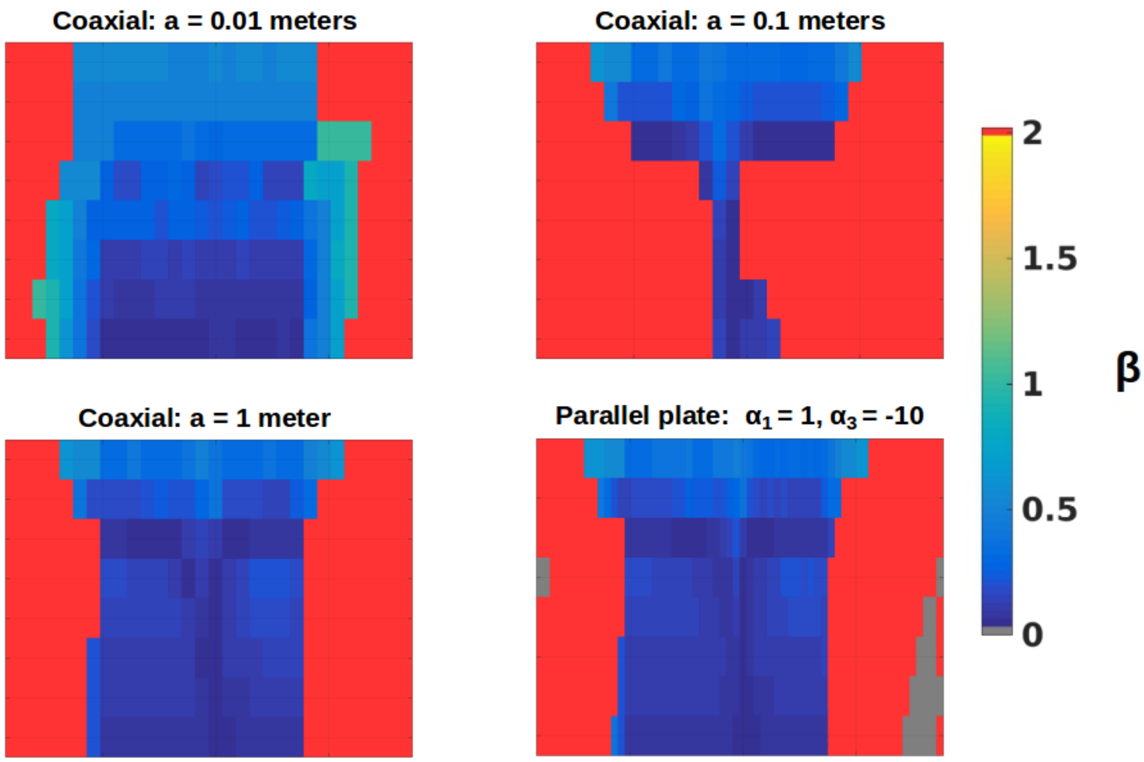

Figure 80: Coaxial cavity steerable-to-zero conditions for a 3rd harmonic perturbative mode, and $\alpha_3 / \alpha_1 = -10$. This corresponds to a starting z position of z=0.31707L. As the inner radius a increases while gap distance remains the same, the results approach the parallel plate standing wave results shown in the lower right pane. Unlabelled axes are as shown in Figure 68.

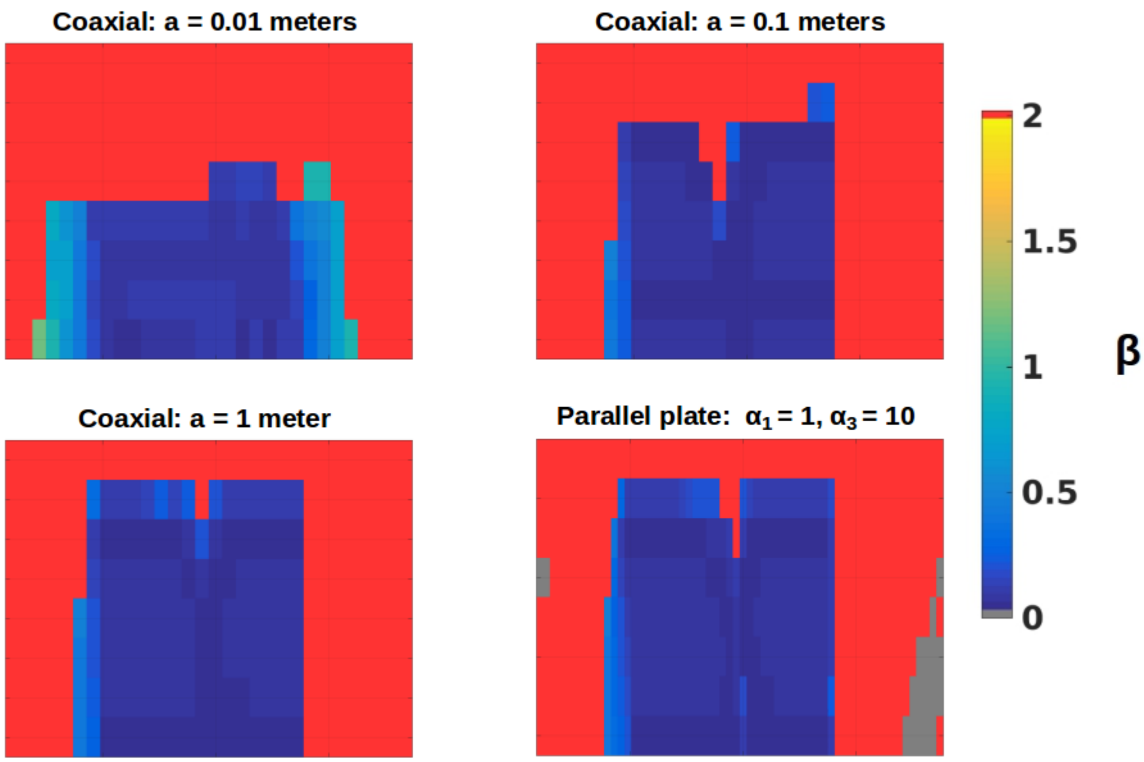

Figure 81: Coaxial cavity steerable-to-zero conditions for a 3rd harmonic perturbative mode, and $\alpha_3 / \alpha_1 = 10$. This corresponds to a starting *z* position of *z*=0.35465L. As the inner radius *a* increases while gap distance remains the same, the results approach the parallel plate standing wave results shown in the lower right pane. Unlabelled axes are as shown in Figure 68.

6.6 Conclusions

We have examined the feasibility of employing a harmonic mode to control the transverse deflection present in a multipactor current, within the context of a parallel plate geometry and with the assumption that space charge effects are negligible. For the parallel plate geometry, we have allowed for generalized ratios of electric to magnetic fields, where arbitrary ratios can occur within a cavity containing standing waves; the limiting assumption to this approach is that multipactor trajectories do not deflect sufficiently far in the transverse direction that the electric and magnetic field ratios change. In addition to just considering standing waves inside a cavity, we also investigated the results with relative phases of the electric and magnetic fields corresponding to travelling waves, as would occur in an infinitely-long waveguide. The controllability results showed significantly different behavior between the two cases. We also examined a few cases involving standing waves within a coaxial geometry, with results that were in general agreement with the parallel plate results as the gap distance became small relative to the coaxial conductor radii.

For standing waves, the results show that for the 2nd, 3rd, and 4th harmonics examined, steerability-to-zero is possible under many circumstances for the 2nd and 3rd harmonic cases, and not very often for the 4th harmonic case. For travelling waves, the results show that for the 2nd, 3rd, and 4th harmonic cases, steerability-to-zero is possible under some circumstances, typically when the harmonic mode magnetic field is much stronger than the fundamental mode magnetic field. However, steerability-to-zero is a harder problem with travelling waves than it is for standing waves.

Future work can examine the steerability-to-zero results when multiple harmonics are present at the same time in the geometry, as well as the possibility of more complicated waveforms such as square wave, triangle, and sawtooth waveforms in addition to the fundamental sinusoidal waveform. Determination of the optimum ratios of fundamental-to-harmonic magnetic fields for the standing wave case would also be useful, since for the 2nd and 3rd harmonic cases, it appears that the optimum ratio does not lie within the range of parameters examined, with improved controllability results observed as the perturbing magnetic field becomes weaker and the fundamental magnetic mode becomes stronger. An examination of other scales of gap distances and excitation frequencies would also be useful to evaluate this technique for higher orders of multipactor with multipacting periods lasting more than one field period. A study involving random secondary emission velocities would also be important to fully characterize the steerability-to-zero conditions, since it is possible that additional randomness in the particle trajectories could increase or decrease the steerability-to-zero in an average sense for given field conditions.

CHAPTER 7: Conclusions

In this dissertation, we have used computational methods to examine multipactor during the early-time of multipactor evolution when space charge effects are negligible. We have mainly focused on two broad areas in particular: the relative accuracy of different secondary electron emission (SEE) models when simulating multipactor, and the effects that perturbing modes can have upon multipactor being primarily driven by a different mode.

The results of chapters 3 and 5 showed the importance of wisely choosing an appropriate SEE model when simulating multipactor. The first key finding of these chapters was that SEE models which have zero secondary electron yield (SEY) below a given impact energy threshold are insufficient to accurately simulate multipactor, due to the fact that some electrons which can result in multipactor will strike a boundary at low impact energies. The SEY of this single impact may be rather small, but we cannot discard it because if the net SEY after multiple impacts is greater than unity, then multipactor can still be sustained.

The second key finding of chapters 3 and 5 is that despite multipactor being a stochastic process due to the underlying stochastic (quantum mechanical) secondary electron emission mechanisms, deterministic models based upon Furman's stochastic SEE model can yield simulation results that agree reasonably well with the average results from Monte Carlo trials using Furman's model. Such a multipactor simulation approach would allow for rapid multipactor simulation over a wide parameter search space, for example to identify possible solutions for a given design goal. Once solutions are found with the approximated non-stochastic model, Monte Carlo simulations using a high-fidelity stochastic model such as Furman's SEE model could be used to optimize the final design.

Chapter 4 examined the effect that perturbing modes can have upon multipactor which is primarily being driven by a different mode. The main takeaway is that even if multipactor is able to be suppressed or enhanced in one location within a cavity or waveguide, the perturbing modes will tend to have the opposite effect for other locations within the geometry. Thus, for the purposes of multipactor suppression, in most cases we likely would not be able to rely solely on a perturbing mode to achieve the results that we want. However, perturbing modes in conjunction with other engineering modifications, such as surface treatments or geometrical adjustments, could be considered as a part of an overall multipactor suppression strategy. One exception to perturbing modes not uniformly changing multipactor susceptibility was observed for the case of a coaxial waveguide, in which a TEM perturbing mode was introduced at half of the TEM primary mode's frequency; future investigation into multipactor suppression via lower-frequency modes is warranted.

In addition to the effects of perturbative modes upon multipactor susceptibility, in chapter 6 we examined how perturbative modes may change the impact points of multipacting electrons. We catalogued the conditions under which selected harmonic modes could be used to actively control the migration direction of multipacting electrons. Future work could investigate the use of such higher-order modes to steer and contain multipacting electrons to desired points within a resonant structure. Such points may be engineered to tolerate, suppress, or even intentionally sustain multipactor. For the case of multipactor suppression, such an approach would allow engineers to focus on reducing multipactor in isolated locations where the perturbing modes direct the multipactor, which would likely be less expensive than attempting to reduce multipactor susceptibility over an entire cavity.

In addition to the future possible research directions noted above, work could also be done to improve simulation capabilities by including space charge effects, which would allow more of the multipactor evolution to be studied beyond the early-time when space charge is negligible. Including space charge effects could be done in two different manners: The first approach would be to incorporate a self-consistent electromagnetics solver which dynamically solves for the fields within the resonant structure as the multipactor current grows and eventually reaches saturation. Such an approach would be rigorous but would need to track numerous particles at once, and potentially be computationally costly, especially for Monte Carlo simulations. A second approach would be to incorporate an approximate space charge effect by assuming a sheet or slab of multipacting electrons, as was done by Vaughan [1], Riyopolous [6], and Kishek [10], among others. This second approach would lack the rigor and fidelity of a self-consistent field model, but could be done at much less computational cost. Such an approach would likely not accurately capture multipactor behavior at full saturation when a multitude of independent particles are present, but would likely extend the applicability of the single particle approach used in this dissertation.

APPENDIX

Choice of Net SEY Threshold for Drift Controllability Study

In Section 6.2 it was noted that a somewhat arbitrary threshold of 0.001 was used for the net SEY in order to decide if a multipactor trajectory was present or not, and this threshold was used for all of the later simulations used to generate the results in Sections 6.4 and 6.5 which showed under which conditions multipactor impact points can be controlled. In order to assess the sensitivity of the controllability results to this net SEY threshold, two controllability cases were examined with thresholds of 0.01 and 0.0001 in addition to the default 0.001. The case of a travelling wave steerable-to-zero conditions for a 3th harmonic perturbative mode, with α_1 = 0.1 and α_3 = -10, is shown in Figure 82 below; the case of a travelling wave steerable-to-zero conditions for a 3th harmonic perturbative mode, with α_1 = 0.316 and α_3 = -3.16, is shown in Figure 83 below. In both cases, the steerability-to-zero results look identical as the threshold was varied, thus suggesting an insensitivity to whatever reasonably-chosen threshold value is used.

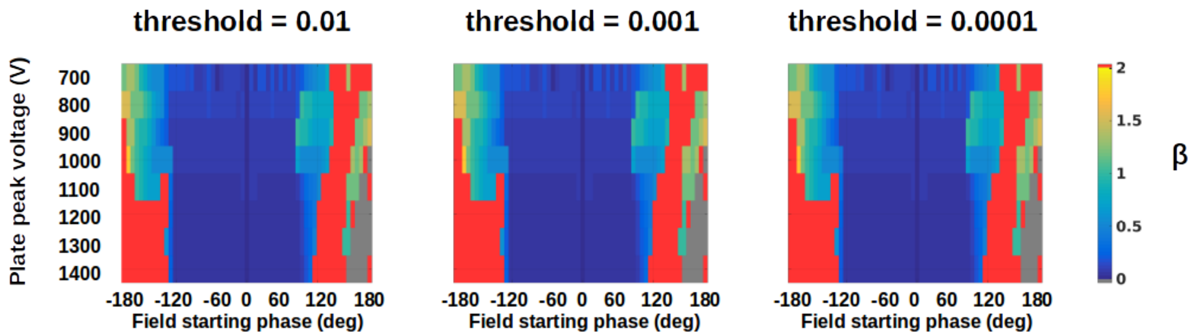

Figure 82: Varying threshold test #1. Travelling wave steerable-to-zero conditions for 3rd harmonic perturbative mode, for $\alpha_1 = 0.1$ and $\alpha_3 = -10$, for three different Net SEY thresholds to use when deciding if multipactor is present.

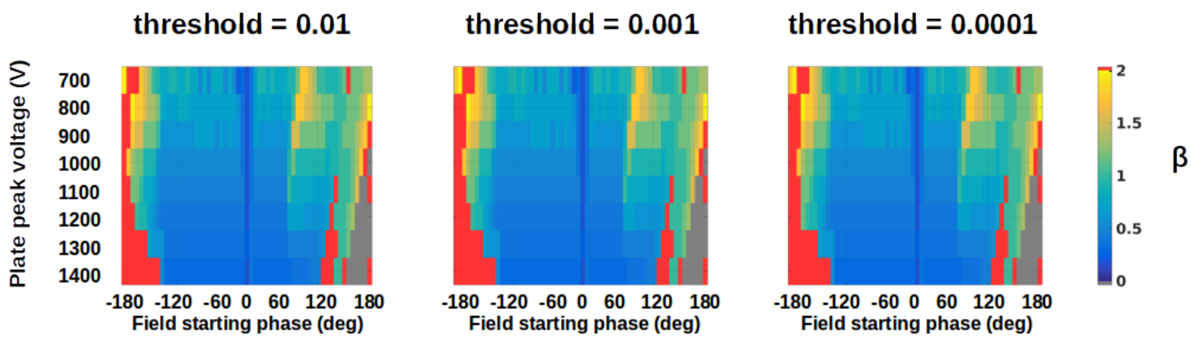

Figure 83: Varying threshold test #2. Travelling wave steerable-to-zero conditions for 3rd harmonic perturbative mode, for $\alpha_1 = 0.316$ and $\alpha_3 = -3.16$, for three different Net SEY thresholds to use when deciding if multipactor is present.

BIBLIOGRAPHY

BIBLIOGRAPHY

[1] J. Rodney M. Vaughan, “Multipactor”, *IEEE Transactions on Electron Devices*, Vol. 35, (no. 7), pp. 1172-1180, July 1988

[2] R.A. Kishek *et al.*, “Multipactor discharge on metals and dielectrics: Historical review and recent theories”, *Physics of Plasmas*, Vol. 5, (no. 5), pp. 2120-2126, 1998

[3] Albert J. Hatch and H. Bartel Williams, “The Secondary Electron Resonance Mechanism of Low-Pressure High-Frequency Gas Breakdown”, *Journal of Applied Physics*, Vol. 25, (no. 4), pp. 417-423, April 1954

[4] Philo Taylor Farnsworth, “Television by electron image scanning”, *Journal of the Franklin Institute*, Volume 218, (no. 4), Pages 411-444, 1934

[5] E. W. B. Gill, A. von Engel, “Starting Potentials of High-Frequency Gas Discharges at Low Pressure”, *Proceedings of the Royal Society A*, Vol. 192, pp. 446-463, 1948

[6] Spilios Riyopoulos *et al.*, “Theory of electron multipactor in crossed fields”, *Physics of Plasmas,* Vol. 2, (no. 8) , pp. 3194-3213, August 1997

[7] Spilios Riyopoulos *et al.*, “Effect of random secondary delay times and emission velocities in electron multipactors”, *IEEE Transactions on Electron Devices*, Vol. 34, (no. 3), pp. 489-497, March 1997

[8] R.A. Kishek and Y.Y. Lau, “Interaction of Multipactor Discharge and rf Circuit”, *Physical Review Letters*, Vol. 75, (no. 6), pp. 1218-1221, August 1995

[9] Agust Valfells *et al.*, “Frequency response of multipactor discharge”, *Physics of Plasmas*, Vol. 5, (no. 1), pp. 300-304, January 1998

[10] R.A. Kishek and Y.Y. Lau, “A novel phase focusing mechanism in multipactor discharge”, *Physics of Plasmas*, Vol. 4, (no. 5), pp. 1481-1483, May 1996

[11] Spilos Riyopoulos, “Multipactor saturation due to space charge-induced debunching”, *Physics of Plasmas*, Vol. 4 (no. 5), pp. 1448-1462, May 1997

[12] V. P. Gopinath *et al.*, “Multpactor electron discharge physics using an improved secondary emission model”, *Physics of Plasmas*, Vol. 5, (no. 5), pp. 1535-1540, May 1998

[13] R. Udiljak *et al.*, “Multipactor in a coaxial transmission line. I. Analytical study”, *Physics of Plasmas*, Vol. 14, pp. 033508-1 through 033508-11, March 2007

[14] V. E. Semenov *et al.*, “Multipactor in a coaxial transmission line. II. Particle-in-cell simulations”, *Physics of Plasmas*, Vol. 14, pp. 033509-1 through 033509-7, March 2007

[15] Antonio M. Pérez *et al.*, “Prediction of Multipactor Breakdown THresholds in Coaxial Transmission Lines for Traveling, Standing, and Mixed Waves”, *IEEE Transactions on Plasma Science*, Vol. 37, (no. 10), pp. 2031-2040, October 2009

[16] Edén Sorolla *et al.*, “An Analytical Modedl to Evaluate the Radiated Power Spectrum of a Multipactor Discharge in a parallel plate Region”, *IEEE Transactions on Electron Devices*, Vol. 55, (no. 8), pp. 2252-2258, August 2008

[17] Vladimir E. Semenov *et al.*, “Simple model of the rf noise generated by multipacting electrons”, *Journal of Phyiscs D: Applied Physics*, Volume 47, pp. 055206-1 through 055206-9, January 2014

[18] Vladimir Semenov *et al.*, “Multipactor suppression in amplitude modulated radio frequency fields”, *Physics of Plasmas*, Vol. 8 (no. 11), pp. 5034-5039, November 2001

[19] V. Semenov *et al.*, “Multipactor in Microwave Transmission Systems Using Quadrature Phase-Shift Keying”, *IEEE Transactions on Plasma Science*, Vol. 38, (no. 4), pp. 915-922, April 2010

[20] Daniel Gonzáles-Iglesias *et al.*, “Analysis of Multipactor Effect Using a Phase-Shift Keying Single-Carrier Digital Modulated Signal”, *IEEE Transactions on Electron Devices*, Vol. 60, (no. 8), pp. 2664-2670, August 2013

[21] N. K. Vdovicheva *et al.*, “Statistical Theory of Two-Sided Multipactor”, *Radiophysics and Quantum Electronics*, Vol. 47, (no. 8), pp. 580-596, August 2004

[22] S. Anza *et al.*, “Nonstationary statistical theory for multipactor”, *Physics of Plasmas*, Vol. 17, pp. 062110-1 through 062110-11, June 2010

[23] S. Anza *et al.*, “Multipactor theory for multicarrier signals”, *Physics of Plasmas*, Vol. 18, pp. 032105-1 through 032105-12, March 2011

[24] Sergio Anza *et al.*, “Prediction of Multipactor Breakdown for Multicarrier Applications: The Quasi-Stationary Method”, *IEEE Transactions on Microwave Theory and Techniques*, Vol. 60, (no. 7), pp. 2093-2105, July 2012

[25] A. Kryazhev *et al.*, “Hybrid resonant modes of two-sided multipactor and transition to the polyphase regime”, *Physics of Plasmas*, Vol. 9 (no. 11), pp. 4736-4743, November 2002

[26] Spilios Riyopoulos, “Higher-order, asymmetric orbit multipactors”, *Physics of Plasmas*, Volume 14, (no. 11), pp. 112101-1 through 112101-11, November 2007

[27] Valery Shemelin, “Generalized phase stability in multipacting”, *Physical Review Special Topics – Accelerators and Beams*, Vol. 14, (no. 9), pp. 092002-1 through 092002-6, September 2011

[28] R. A. Kishek, “Ping-Pong Modes: A New Form of Multipactor”, *Physical Review Letters*, Vol. 108, (no. 3), pp. 035003-1 through 035003-5, January 2012

[29] V. E. Semenov *et al.*, “Multipactor in rectangular waveguides”, *Physics of Plasmas*, Vol. 14, pp. 033501-1 through 033501-8, March 2007

[30] J. Rasch *et al.*, “Microwave Multipactor Breakdown Between Two Cylinders”, *IEEE Transactions on Plasma Science*, Vol. 38, (no. 8), pp. 1997-2005, August 2010

[31] J. Rasch *et al.*, “Simulations of Multipactor Breakdown Between Two Cylinders”, *IEEE Transactions on Plasma Science*, Vol. 30, (no. 9), pp. 1786-1794, September 2011

[32] Vladimir E. Semenov *et al.*, “General Study of Multipactor Between Curved Metal Surfaces”, *IEEE Transactions on Plasma Science*, Vol. 42, (no. 3), pp. 721-728, March 2014

[33] *CRC Handbook of Chemistry and Physics*, 65th Edition. Boca Raton, FL: CRC Press, 1994, Section 12, p. 115

[34] J. Rodney M. Vaughan, “A New Formula for Secondary Emission Yield”, *IEEE Transactions on Electron Devices*, Vol. 36, (no. 9), pp. 1963-1967, (September 1989). See also the article revision by the same author published as “Secondary Emission Formulas”, *IEEE Transactions on Electron Devices*, Vol. 40, (no. 4), p. 830, April 1993

[35] M.A. Furman and M.T.F. Pivi, “Probabilistic model for the simulation of secondary electron emission”, *Physical Review Special Topics – Accelerators and Beams*, Vol. 5, (no. 124404), pp. 124404-1 through 124404-18, 2002

[36] Hasan Padamsee *et al.*, Chapter 10 in *RF Superconductivity for Accelerators*, Weinheim, Germany: WILEY-VCH, 2008

[37] Scott Rice and John Verboncoeur, "Quasi-Analytical Derivation of parallel plate Multipactor Trajectories in the Presence of Higher-Order Mode Perturbations", *2016 IEEE International Power Modulator and High Voltage Conference (2016 IPMHVC)*, San Francisco, CA, July 5-9, 2016

[38] Michael Baake and Ulrike-Schlägel, “The Peano-Baker Series”, arXiv:1011.1775v2 [math.CA], January 6, 2012, available online at http://arxiv.org/abs/1011.1775v2

[39] Panos J. Antsaklis and Anthony N. Michel, Chapters 1 and 3 in *A Linear Systems Primer*, Boston, Massachusetts: Birkhauser, 2007

[40] "ode45", *MATLAB Documentation*, The MathWorks®, retrieved July 15, 2017 from https://www.mathworks.com/help/matlab/ref/ode45.html

[41] Lawrence F. Shampine and Mark W. Reichelt, "The MATLAB ODE Suite," *SIAM Journal on Scientific Computing*, Vol. 18, 1997, pp. 1–22. Also available on the Mathworks website at https://www.mathworks.com/help/pdf_doc/otherdocs/ode_suite.pdf

[42] J. Wei *et al.,* "The frib project–accelerator challenges and progress." *Heavy Ion Accelerator Technology Conference 2012 (HIAT2012)*, Chicago, IL, June 18-21, 2012.

[43] Scott Rice and John Verboncoeur, "Multipactor Suppression in Resonant Cavities via Higher Order Modes", *IEEE Conference on Pulsed Power & Plasma Science (PPPS 2013)*, San Francisco, CA., June 16-21, 2013.

[44] R. Cimino et. al., "Can Low-Energy Electrons Affect High-Energy Physics Accelerators?", *Phys. Rev. Letters*, Vol. 93, (no. 1), pp. 014801-1 through 014801-4, 2004.

[45] Scott Rice and John Verboncoeur, "Multipactor Current Modelling Using an Averaged Version of Furman's SEY Model", *41st IEEE International Conference on Plasma Science (ICOPS 2014)*, Washington, DC, May 25-29, 2014

[46] Scott Rice and John Verboncoeur, "Multipactor Current Growth Modelling Using an Averaged Version of Furman's SEY Model", *International Particle Accelerator Conference (IPAC'15)*, Richmond, VA, May 3-8, 2015

[47] Scott Rice and John Verboncoeur, "Multipactor Breakdown Modelling Using an Averaged Version of Furman's SEY Model", *42nd IEEE International Conference on Plasma Science (ICOPS 2015)*, Belek, Analya, Turkey, May 24-28, 2015

[48] Scott Rice and John Verboncoeur, "Migration of Multipactor Trajectories Via Higher-Order Mode Perturbation." accepted for publication in an upcoming issue of *IEEE Transactions on Plasma Science*, 2017

[49] E.J. Sternglass, "Theory of Secondary Electron Emission by High-Speed Ions", *The Phyical Review*, Vol. 108, (no. 1), pp. 1-12, October 1957.